UNIVERSITY OF CALIFORNIA,
IRVINE

Spin Polarized Fuel and Artificial Intelligence in Fusion Energy at DIII-D

DISSERTATION

submitted in partial satisfaction of the requirements
for the degree of

DOCTOR OF PHILOSOPHY

in Physics

by

Alvin V. Garcia

Dissertation Committee:
Professor William W. Heidbrink, Chair
Professor Zhihong Lin
Professor David Kirkby

2023

DEDICATION

To my family.

TABLE OF CONTENTS

LIST OF FIGURES

LIST OF TABLES

ACKNOWLEDGMENTS

Several people made significant contributions to my thesis and education. I would like to express my deepest gratitude to Professor Bill Heidbrink for acceptance into his group, guidance on my projects, and support throughout my graduate education. Early in my PhD, the experience in the National Science Foundation funded Machine Learning and Physics Sciences (MAPS) fellowship program led by Padhraic Smyth, Pierre Baldi, Maritza Salazar Campo and the rest of the Principal Investigators had a great impact on the trajectory of my studies and I'm grateful to have participated in this group. Later in my PhD, Egemen Kolemen encouraged me to join and visit his Plasma Control Group at Princeton University as a funded fellow, and I'm immensely thankful for his encouragement since this was a stimulating experience for me. Also, I would like to thank Zhihong Lin and David Kirkby for serving on my thesis committee. Last but not least, I would like to thank my classmates and friends Cody Combs, Wenhao Wang, Ernesto Barraza-Valdez, Daniel Lin, Eric Nelson, Michael Seggebruch, Kenneth Gage, Genevieve DeGrandchamp, Garrett Prechel and Wataru Hayashi for working on coursework or attending conferences with me. As a final note, I'd like to thank Bill and David for playing pick-up soccer with me.

Chapters 2, 3 and 4 of this dissertation are reprints of the material as it appears in [1], [2], and [3, 4], respectively. The co-authors listed in these publications are the following: chapter 2) W.W. Heidbrink, **A.V. Garcia**, W. Boeglin, M. Salewski, chapter 3) **A.V. Garcia**, W.W. Heidbrink, A.M. Sandorfi, chapter 4) **A.V. Garcia**, A. Jalalvand, P. Steiner, A. Rothstein, M. Van Zeeland, W.W. Heidbrink, E. Kolemen. Chapters 2–4 are used with permission from IOP Publishing. Chapter 4 is also used with permission from IEEE.

Additionally, I would like to thank the following list of people for their contributions to:

- Chapter 2: A. Netepenko for providing data for this study and L. Stagner for helpful suggestions.
- Chapter 3: Larry Baylor, Keith Burrell, Xiaodi Du, Brian Grierson, Eric Hollmann, Val Izzo, Vasili Kiptily, David Pace, Sterling Smith, Luke Stagner and Mike Van Zeeland for helpful comments.
- Chapter 4: Azarakhsh Jalalvand for mentoring me and Michele Guindani for providing helpful tips.

This material is based upon work supported by the U.S. Department of Energy, Office of Science, Office of Fusion Energy Sciences, Office of Workforce Development for Teachers and Scientists, Office of Science Graduate Student Research (SCGSR) program, using the DIII-D National Fusion Facility, a DOE Office of Science user facility, under Award(s) DE-SC0014664, DE-SC0021624, DE-SC0001157, DE-SC0019253, DE-SC0020337, DE-FC02-04ER54698, DE-SC0021275, and in part by the United States Department of Energy, Office of Nuclear Physics Division, under contract DE-AC05-06OR23177 under which Jefferson

Science Associates operates Jefferson Laboratory. The SCGSR program is administered by the Oak Ridge Institute for Science and Education (ORISE) and managed by ORAU for the DOE. Also supported by the Army Research Office (ARO W 911NF-19-1-0045), National Science Foundation under 1633631, Ghent University Special Research Award No. BOF19/PDO/134.

This dissertation contains excerpts from prior publications as follows:

- Chapter 2: W.W. Heidbrink, **A.V. Garcia**, et al. "Phase-space sensitivity (weight functions) of 3 MeV proton diagnostics." *Plasma Physics and Controlled Fusion* 63.5 (2021): 055008.
- Chapter 3: **A.V. Garcia**, W.W. Heidbrink, et al. "Conceptual design of DIII-D experiments to diagnose the lifetime of spin polarized fuel." *Nuclear Fusion* 63 (2022): 026030.
- Chapter 4:
  - **A.V. Garcia**, A. Jalalvand, et al. "Alfvén eigenmode detection using long-short term memory networks and CO_2 interferometer data on the DIII-D National Fusion Facility," *in 2023 International Joint Conference on Neural Networks (IJCNN) (IEEE)* (2023): pp. 1–8.
  - **A.V. Garcia**, A. Jalalvand, et al. "Comparison of machine learning systems trained to detect Alfvén eigenmodes using the CO_2 interferometer on DIII-D." *Nuclear Fusion* (submitted 2023).

VITA

Alvin V. Garcia

EDUCATION

Doctor of Philosophy in Physics **2023**
University of California, Irvine *Irvine, California*

Bachelor of Science in Physics **2016**
University of California, Los Angeles *Los Angeles, California*

RESEARCH EXPERIENCE

Graduate Student Researcher **2018–2023**
University of California, Irvine *Irvine, California*
- DOE SCGSR Fellowship 2021–2022 (@ Princeton University, PPPL)
- NSF Research Trainee Fellowship 2019–2021

Development Engineering Intern **2017**
RadiaBeam Technologies *Santa Monica, California*

Undergraduate Student Researcher **2015–2016**
University of California, Los Angeles *Los Angeles, California*
- Regents Scholarship 2014–2016

TEACHING EXPERIENCE

Graduate Teaching Assistant **2017**
University of California, Irvine *Irvine, California*

AWARDS

Van Zeeland Prize for the Most Exciting Idea of the Year at DIII-D **2022**
Conceptual design of DIII-D experiments to diagnose the lifetime of spin polarized nuclei (Talk)

Exceptional Poster Award at ITER International School **2022**
Conceptual design of DIII-D experiments to diagnose the lifetime of spin polarized nuclei (Poster)

REFEREED JOURNAL PUBLICATIONS

Comparison of machine learning systems trained to detect Alfvén eigenmodes using the CO_2 interferometer on DIII-D — **submitted 2023**
A.V. Garcia, A. Jalalvand, P. Steiner, et al.

Nuclear Fusion

Conceptual design of DIII-D experiments to diagnose the lifetime of spin polarized fuel — **2023**
A.V. Garcia, W.W. Heidbrink, A.M.J. Sandorfi

*Nuclear Fusion **63** 026030*

Exploring data-driven models for spatiotemporally local classification of Alfvén eigenmodes — **2022**
A. Kaptanoglu, A. Jalalvand, **A.V. Garcia**, et al.

*Nuclear Fusion **62** 106014*

Alfvén eigenmode classification based on ECE diagnostics at DIII-D using deep recurrent neural networks — **2021**
A. Jalalvand, A. Kaptanoglu, **A.V. Garcia**, et al.

*Nuclear Fusion **62** 026007*

Phase-space sensitivity (weight functions) of 3 MeV proton diagnostics — **2021**
W.W. Heidbrink, **A.V. Garcia**, et al.

*Plasma Physics and Controlled Fusion **63** 055008*

Fast-ion D alpha diagnostic with 3D-supporting FIDASIM in the Large Helical Device — **2020**
Y. Fujiwara, S. Kamio, H. Yamaguchi, **A.V. Garcia**, et al.

*Nuclear Fusion **60** 112014*

Progress in modelling fast-ion D-alpha spectra and neutral particle analyzer fluxes using FIDASIM — **2020**
B. Geiger, L. Stagner, W.W. Heidbrink, R. Dux, Y. Fujiwara, **A.V. Garcia**, et al.

*Plasma Physics and Controlled Fusion **62** 105008*

Tomography of the positive-pitch fast-ion velocity distribution in DIII-D plasmas with Alfvén eigenmodes and neoclassical tearing modes — **2020**
B Madsen, M Salewski, W.W. Heidbrink, L Stagner, M Podestà, D Lin, **A.V. Garcia**, et al.

*Nuclear Fusion **60** 066024*

Evaluation of an energetic particle profile using a tangential-fida diagnostic in the large helical device **2019**
Y. Fujiwara, S. Kamio, H. Yamaguchi, **A.V. Garcia**, et al.

*Plasma and Fusion Research **14** 3402129*

Isotropic rotation in amphidynamic crystals of stacked carbazole-based rotors featuring halogen-bonded stators **2016**
A.C. Molina, S.P. Estrada, A.E. Roa, **A.V. Garcia**, et al.

*Chemical Communications **52** 12833*

REFEREED CONFERENCE PUBLICATIONS

Alfvén Eigenmode Detection using Long-short Term Memory Networks and CO_2 Interferometer Data on the DIII-D National Fusion Facility **2023**
A.V. Garcia, A. Jalalvand, P. Steiner, et al.

2023 International Joint Conference on Neural Networks (IJCNN) (IEEE): pp. 1–8

TALKS

Machine Learning-based Classification of Alfvén Eigenmodes Using CO2 Interferometer Data on the DIII-D National Fusion Facility **2023**
29th ACM SIGKDD Conference on Knowledge, Discovery and Data Mining

Alfvén eigenmode detection using long-short term memory networks and CO_2 interferometer data on the DIII-D National Fusion Facility **2023**
2023 International Joint Conference on Neural Networks (IJCNN)

Development and comparison of Machine Learning systems trained to automatically classify Alfvén eigenmodes on DIII-D **2022**
28th Meeting of ITPA Topical Group on Energetic Particle Physics

Conceptual design of DIII-D experiments to diagnose the lifetime of spin polarized fuel **2021**
17th Technical Meeting on Energetic Particles and Theory of Plasma Instabilities in Magnetic Confinement Fusion

POSTERS

Conceptual design of DIII-D experiments to diagnose the lifetime of spin polarized fuel **2022**
64th Annual Meeting of the APS Division of Plasma Physics (Spokane, Washington)

Deep learning-based classification of Alfvén eigenmodes using CO_2 interferometer data on the DIII-D tokamak **2022**
Annual Meeting of ANS Technology of Fusion Energy (Anaheim, California)

Classifying Alfvén eigenmodes using deep learning and CO_2 interferometer data at DIII-D **2021**
63rd Annual Meeting of the APS Division of Plasma Physics (Pittsburgh, Pennsylvania)

Enhanced version of FIDASIM simulates passive signals, accepts 3D geometry and is reunified with European code **2020**
23rd Topical Conference on High Temperature Plasma Diagnostics (Virtual)

Development of weight functions for 3 MeV proton diagnostics in FIDASIM **2020**
62nd Annual Meeting of the APS Division of Plasma Physics (Virtual)

Extensions of FIDASIM capabilities: Passive signals, 3D geometry and neutron collimator signals **2019**
16th Technical Meeting on Energetic Particles and Theory of Plasma Instabilities in Magnetic Confinement Fusion (Shizuoka, Japan)

Introduction of passive signals and 3D geometry to FIDASIM **2018**
60th Annual Meeting of the APS Division of Plasma Physics (Portland, Oregon)

SOFTWARE

FIDASIM `www.github.com/D3DEnergetic/FIDASIM`
A Neutral Beam and Fast-ion Diagnostic Modeling Suite.

ABSTRACT OF THE DISSERTATION

Spin Polarized Fuel and Artificial Intelligence in Fusion Energy at DIII-D

By

Alvin V. Garcia

Doctor of Philosophy in Physics

University of California, Irvine, 2023

Professor William W. Heidbrink, Chair

This thesis presents advances in computational modelling, analysis and techniques that can be used to study mission critical topics in fusion. Energetic particles is an important field of research since information about the plasma state can be encoded in the fast-ion distribution function. Energetic ions can resonate with plasma waves in a fusion device, degrade plasma performance or confinement, and damage the inner walls of the vessel. There is a need in the community to better understand the fast-ion distribution function, improve plasma performance, and mitigate unwanted impacts from wave-particle interactions.

In chapter 2, the weight function for 3-MeV protons produced in d(d,p)t fusion reactions between a fast ion and a thermal deuteron is developed. The weight function $W(X)$ is a diagnostic sensitivity to phase-space variables X that relates the measured signal C to the distribution function $F(X)$ through the equation $C = \int W(X)F(X)\,dX$. The algorithm developed here accounts for the complications associated with the curved "sightline" trajectories of the escaping protons. Time-reversed orbits are initially calculated to get the effective solid angles and sightlines for the range of incident proton velocity vectors. Synthetic diagnostic code FIDASIM [Plasma Phys. Cont. Fusion **62** (2020) 105008] is upgraded to accept these inputs, then calculate the reactivity averaged over the thermal distribution of the "target" deuterons and the probability that a fast ion of specified energy and pitch has

a gyroangle that is consistent with the kinematic equations along each of the sightlines. The outputs of this upgraded version of FIDADSIM are verified using independent calculations on the Mega Amp Spherical Tokamak.

In chapter 3, a conceptual design to diagnose the lifetime of spin polarized fusion experiments using existing port geometries is developed at DIII-D. The cross sections for the D-T and D-^{3}He fusion reactions are increased by as much as 50% if the fuel remains spin polarized parallel to the magnetic field in magnetically confined fusion experiments. The goal in this chapter is to assess the feasibility of lifetime measurements of spin polarization, in magnetic fusion relevant conditions, on the DIII-D tokamak using relative changes in charged fusion product (CFP) loss measurements that depend upon the differential fusion cross section $\mathrm{d}\sigma/\mathrm{d}\Omega$. Relative measurements that capture changes in the escaping CFP pitch, poloidal, and energy distributions are studied in two realistic TRANSP calculated plasma scenarios (high T_i and beam-plasma). Ideal CFP detection, a realistic assessment of CFP signals and reduced chi-squared χ_r^2 calculations show polarization lifetime measurements are feasible for the thermonuclear (high T_i) scenario.

In chapter 4, Machine Learning (ML) models are developed to automatically detect Alfvén eigenmodes (AE) and these models achieve high performance (True Positive Rate = 90% and False Positive Rate = 14%). ML-based models can be useful for real-time detection and control of AEs in steady-state plasma scenarios. These ML systems can be implemented into control algorithms that drive actuators for mitigation of unwanted AE impacts. Using labels created from a curated database [Heidbrink, et al., Nucl. Fusion '20], Machine Learning-based systems are trained using single chord and crosspower spectrograms to predict the presence of 5 AEs (EAE, TAE, RSAE, BAE and LFM). The advantages of using the CO_2 interferometer to detect AEs, and the results from a comparison between inputs (single chord and crosspower spectrograms) and another comparison between two different ML models (Reservoir Computing Network and Long Short-Term Memory Network) are covered here.

Chapter 1

Introduction

Energy is important to the livelihood of developed and developing nations. Basic needs such as warm food, clean water and safe shelter all require energy. In the case of an emergency, a charged mobile phone or medical device can save one's life. Generally speaking, the quality of life substantially improves with more energy worldwide, see Panel (a) of Figure 1.1. However, energy produced by burning oil, coal, and gas directly exacerbates extreme climate change since large quantities of emitted carbon dioxide (CO_2) get trapped in our atmosphere. Global warming, ice melt and rising sea levels are hindering the natural development of our ecosystems. Panel (b) of Figure 1.1 shows that the Human Development Index increases at the cost of more pollution to the earth's atmosphere. Alternative energy sources like solar, wind or hydroelectric are better, but these all depend upon environmental stimulus and intermittent weather conditions. There is a need for a fundamentally new source of energy that is clean, abundant and sustainable.

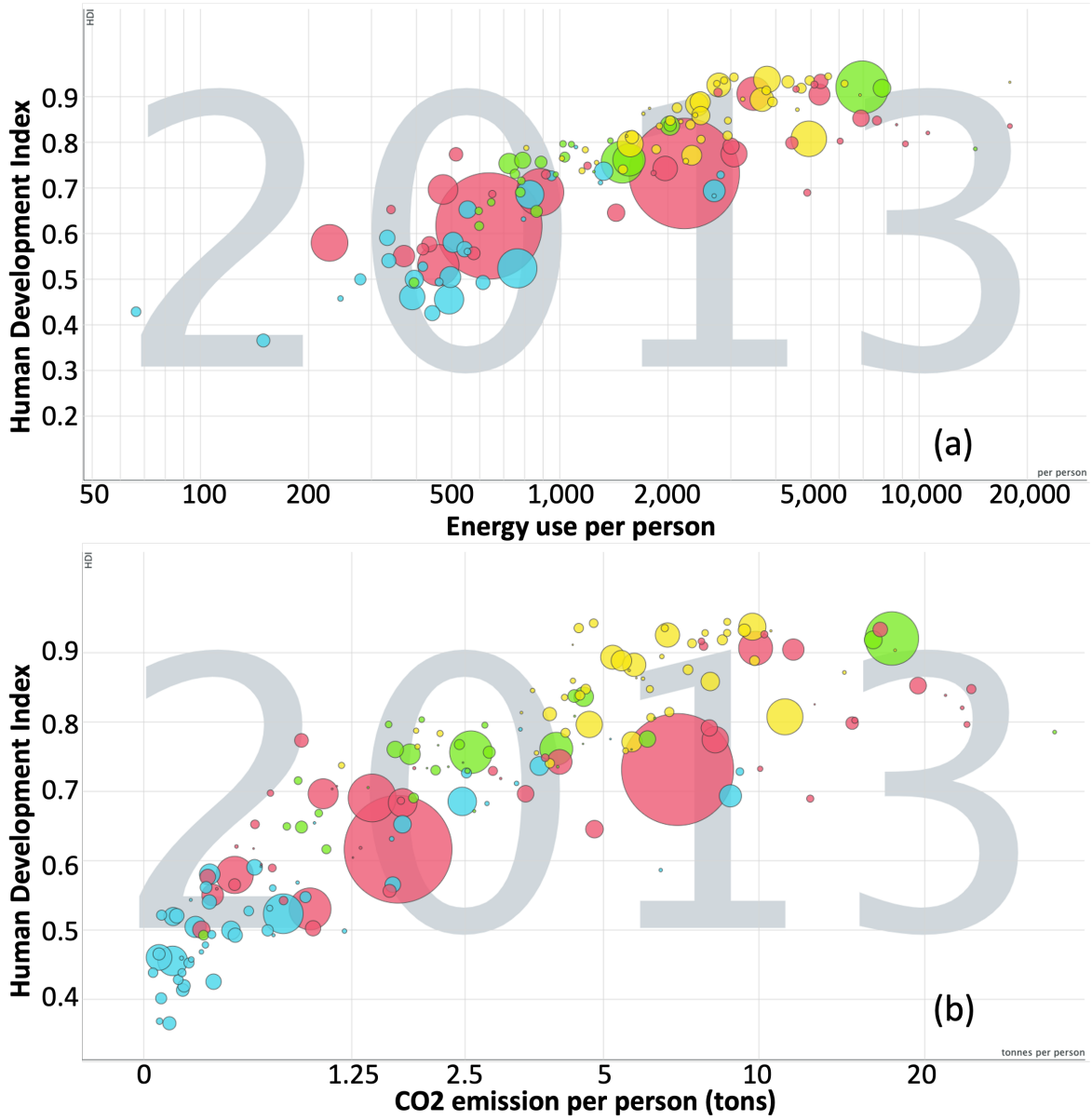

Figure 1.1: The Human Development Index (HDI) [5] is a value that considers three parameters: 1) a long-healthy life, 2) being knowledgeable, and 3) standard of living. There is a strong positive correlation between energy use per person and HDI (panel a). However, CO_2 emissions similarly increase and cause harm to the planet (panel b). Figures are adapted from [6].

1.1 Fusion Energy

Nuclear power can be produced from *fission* or *fusion* reactions. Although naming looks a bit similar and both reactions are exothermic, the two processes are very different from each other. In a *fission* reaction, a heavy and unstable nucleus is *split* into two lighter nuclei and can release energy in the process. The oppositie scenario takes place in a *fusion* reaction, where two light nuclei *combine* to form a larger nucleus and release energy. Naturally occurring fusion happens in the sun, where large gravitational fields pull nuclei into the core. The nuclei have large amounts of kinetic energy to overcome the electrostatic repulsion and get close enough such that the nuclear strong force activates a fusion reaction. The mass difference between the reactants and products is converted into kinetic energy according to Einstein's formula:

$$E = mc^2 \tag{1.1}$$

where the speed of light $c = 3 \times 10^8\,\mathrm{m/s}$. This mass difference is significantly larger for fusion reactions than it is for fission reactions, see Figure 1.2. Although *fission* power plants currently contribute to electricity grids throughout the world, they are dangerous since harmful weapons-grade radioactive waste is produced in the fuel rods. On the other hand, the anticipated amount of activation in the materials is substantially less for *fusion* power plants. The fusion fuel comes from water and abundantly safe materials found in nature. Also, there is no risk of nuclear weapons proliferation or a power plant meltdown for a *fusion* device. In a future where nuclear power plays an important role in the production of clean energy, controlled nuclear *fusion* is the most promising candidate.

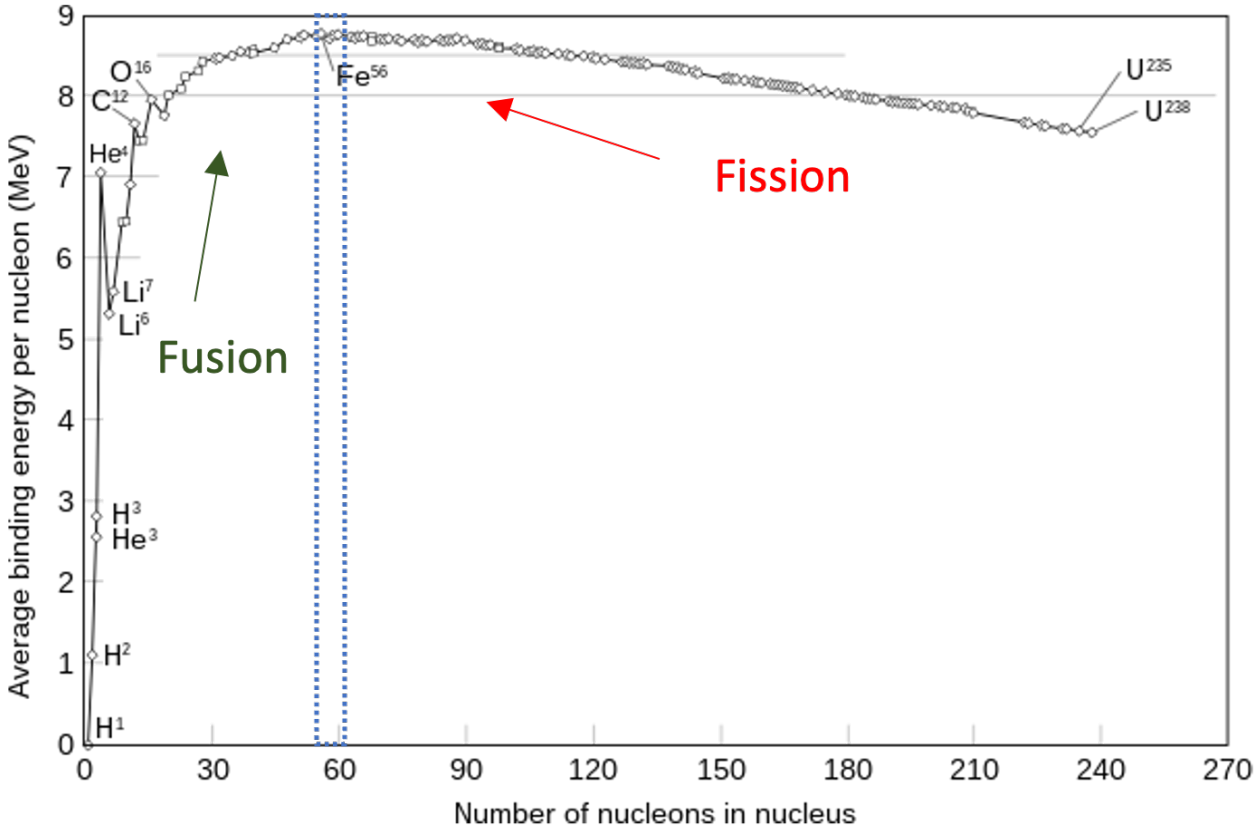

Figure 1.2: The binding energy curve demonstrates energetically favorable regions for *fusion* and *fission* reactions on the left and right of the nuclear stability region (blue dashed column), respectively. Since deuterium, H^2, and tritium, H^3, are low on this curve, relatively larger amounts of energy can be produced from fusion reactions between these two nuclei. Figure is adapted from [7].

There are many nuclear reactions that are useful for the production of fusion energy, and the most promising three for magnetic confinement fusion are the following:

$$\begin{aligned} \mathrm{D} + \mathrm{D} &\xrightarrow[50\%]{} \mathrm{T}\,(1.01\,\mathrm{MeV}) + p\,(3.02\,\mathrm{MeV}) \\ &\xrightarrow[50\%]{} {}^{3}\mathrm{He}\,(0.82\,\mathrm{MeV}) + n\,(2.45\,\mathrm{MeV}) \end{aligned} \tag{1.2}$$

$$\mathrm{D} + \mathrm{T} \xrightarrow[100\%]{} \alpha(3.5\,\mathrm{MeV}) + n\,(14.1\,\mathrm{MeV}) \tag{1.3}$$

$$\mathrm{D} + {}^{3}\mathrm{He} \xrightarrow[100\%]{} \alpha(3.6\,\mathrm{MeV}) + p\,(14.7\,\mathrm{MeV}), \tag{1.4}$$

where D is deuterium ("heavy" hydrogen ${}^{2}_{1}\mathrm{H}$), T is tritium ("heavier" hydrogen ${}^{2}_{1}\mathrm{H}$), α is ${}^{4}_{2}\mathrm{He}$, n is a neutron, and p is a proton. From these equations, the most favorable is D-T fusion (Equation 1.3) since it has the largest cross section at low energy and can produce large amounts of energy. Figure 1.3 shows the reactivity averaged over a Maxwellian distribution function for all three reactions.

The triple product is a useful metric of success in magnetic confinement fusion that indicates the necessary conditions to reach "ignition" (self-sustaining plasma), and for a D-T plasma it is defined as follows:

$$nT\tau_E \geq 3 \times 10^{21}\,\mathrm{m}^{-3}\mathrm{keVs}, \tag{1.5}$$

where n is the ion density, T is the ion temperature and and τ_E is the energy confinement time [8]. In an ignited state, the plasma temperature is sustained against energy losses by the internal alpha self heating produced from the fusion reactions. Energetic lasers were recently used to compress a small pellet of D-T fuel to the high temperatures and pressures needed to achieve "ignition" at the National Ignition Facility [9]. The planned International Thermonuclear Experimental Reactor (ITER) is a magnetic confinement fusion device and projected to achieve ignition within the 10–20 keV range [10]. Parts of this thesis contributed to the overall goal of reaching ignition in magnetic confinement fusion energy research.

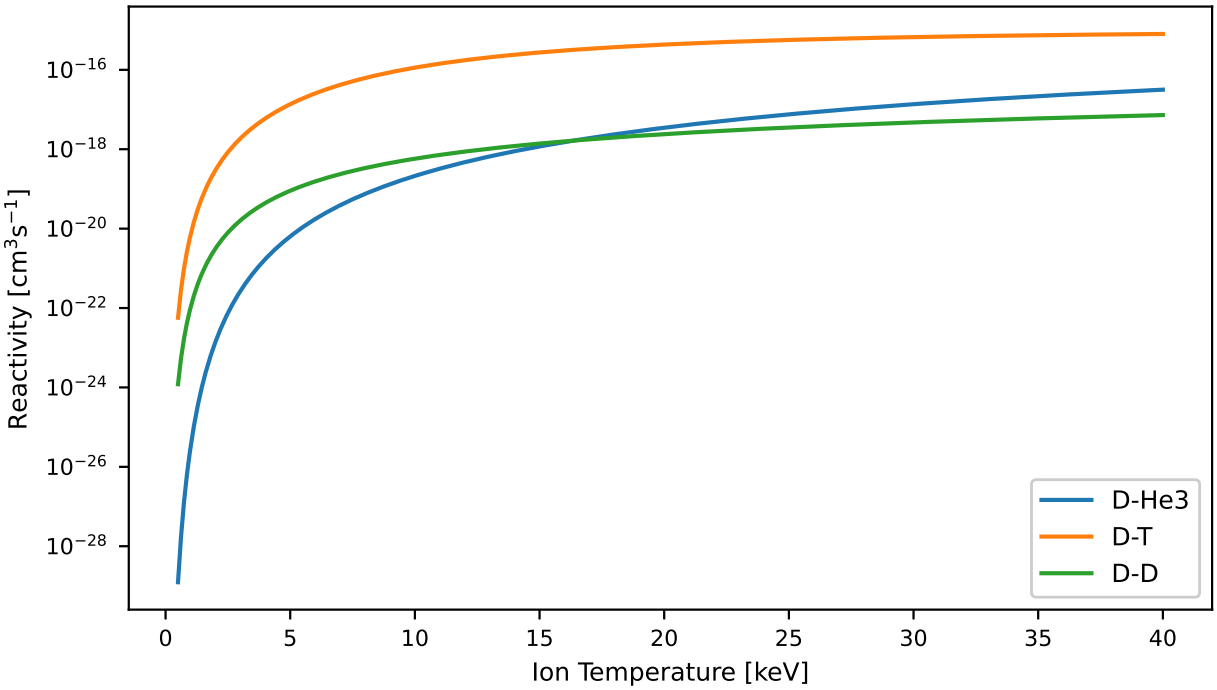

Figure 1.3: Reactivities for the three most promising fusion reactions calculated using Table VII of [11]. D-T fusion can be 1–2 orders of magnitude higher than the other two reactions.

1.2 Tokamaks

The word *Tokamak* is Russian and means toroidal apparatus for the production of controlled nuclear fusion reactions in a high temperature plasma. Originally conceptualized by Soviet physicists Igor Tamm and Adrei Sakharov in the 1950s [12], these devices are donut-shaped vessels that produce strong magnetic fields and confine plasma. Some authors maintain that spherically shaped devices are the leading candidate for a fusion nuclear science facility (FNSF) [13], but conventional (D-shaped) tokamaks also play an important role in fusion since they can withstand intense pressures and excel in plasma shaping capabilities.

The toroidal coordinate system (R, ϕ, Z) used to describe the plasma inside a tokamak is shown in Figure 1.4. The major radius and elevation are denoted by R and Z, respectively. The spatial coordinate (ϕ) that wraps around the axis of symmetry ($R = 0$) is positive in a right-handed (thumbs up) orientation. The 2D coordinate system perpendicular to the toroidal direction (cross-sections of the plasma) is the poloidal plane and characterized by minor radius r and poloidal angle θ. The "origin" of the poloidal plane ($R = R_0$) is the torus axis and usually located in the core of the plasma.

External coils are used to produce the helical magnetic fields of a tokamak, see Figure 1.5. The center stack and outer poloidal field coils produce an electric field in the plasma that can drive current in the toroidal direction. This plasma current produces the poloidal magnetic field. An array of coils that encircle the torus produces the toroidal magnetic field. The resulting field is helical and winds around the vessel about the machine axis.

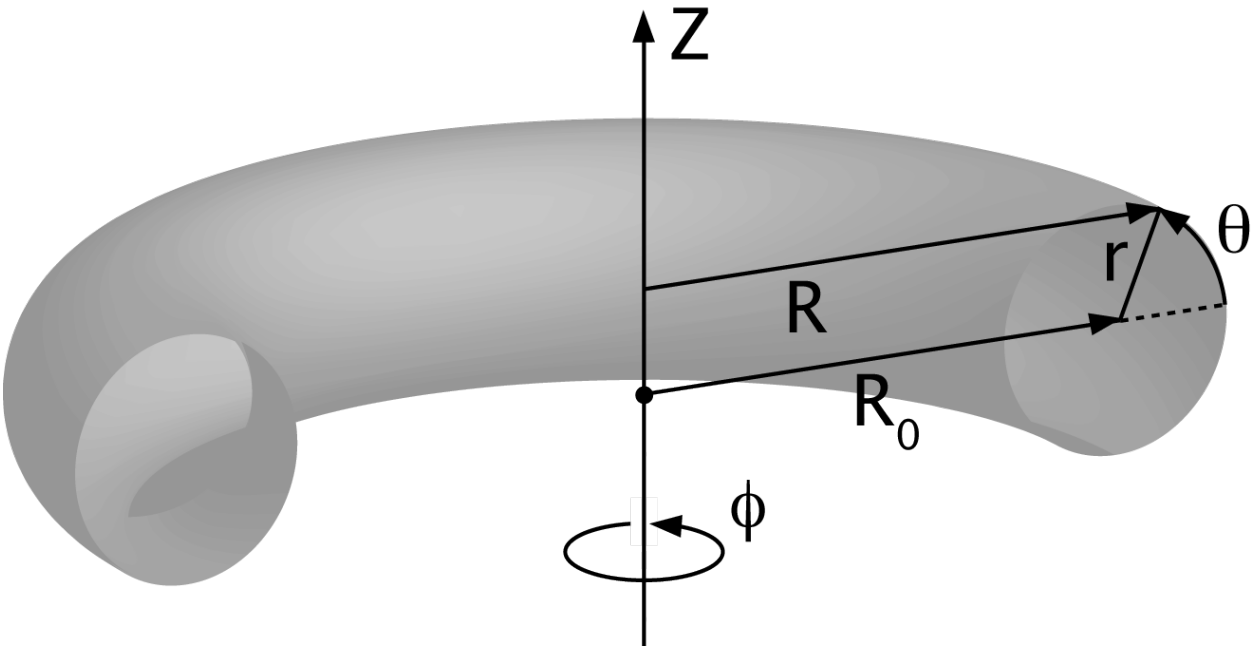

Figure 1.4: A diagram of the toroidal coordinate system (R, ϕ, Z) commonly used to describe tokamak plasmas. The poloidal radius and angle are denoted by r and θ. Also, R_0 is the location of the torus axis (usually aligns with the magnetic axis in fusion research). Figure is from [14]

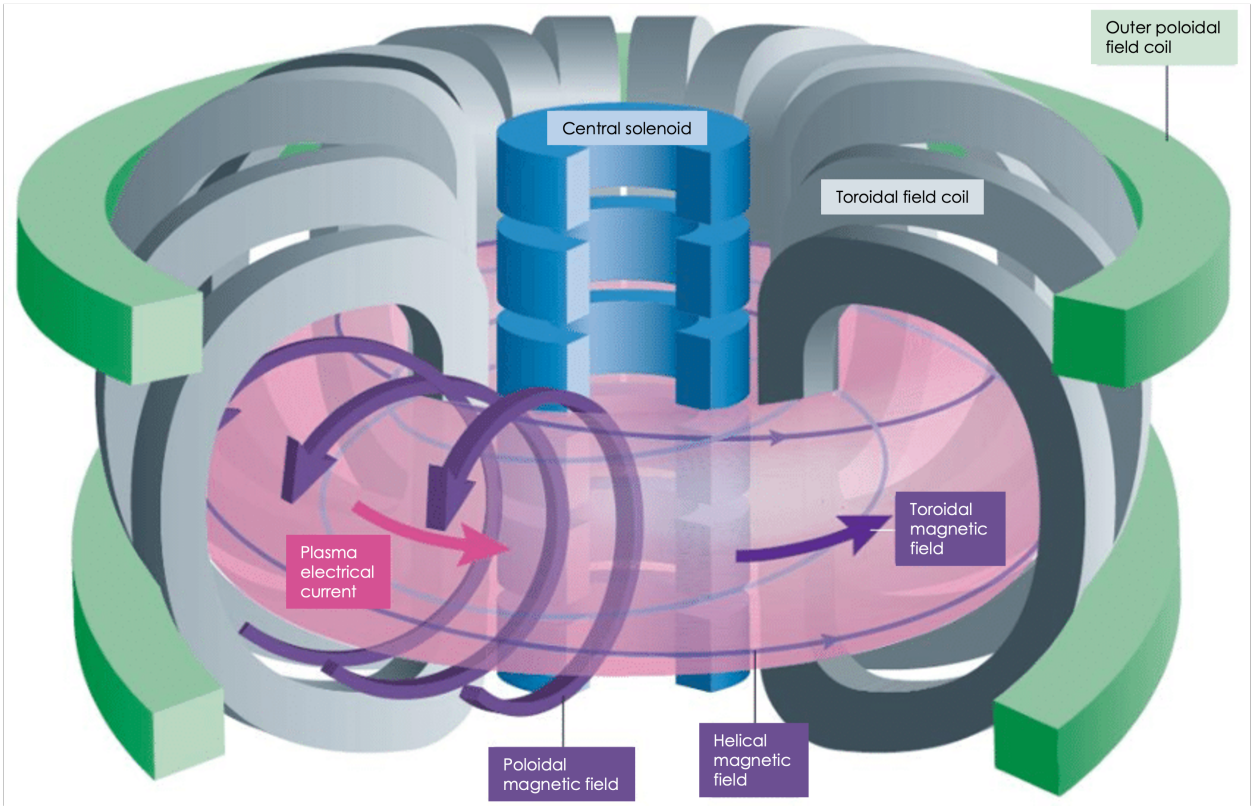

Figure 1.5: A schematic design of the fields and currents of a fusion device. An array of coils produces the toroidal field. The center stack and poloidal coils drive a plasma current that produces a poloidal magnetic field. Both fields create a net helical field that wraps around the device in the toroidal direction. Figure is from [15]

To get a burning plasma, inductive and non-inductive methods are used to raise the temperature. For inductive methods, currents are driven through the center stack of coils in the middle of the device that produce a plasma current and raise the temperature via "ohmic" heating. Inductive current drive requires a pulsed reactor system and can create issues associated with thermal cycling of the walls and a pulsing magnetic circuit design [16]. For non-inductive methods, Neutral Beam Injection (NBI) or radio-frequency (RF) waves are used to heat the plasma. Injected neutrals can thermalize and impart their energy onto the bulk plasma. Resonant RF waves can change the cyclotron motion of bulk ions (or electrons) and raise the temperature. Additionally, these non-inductive heating mechanisms can create a small population of *fast ions* (a class of super-thermal particles) that are important to study. Section 1.3 discusses them in greater detail.

The DIII-D National Fusion Facility is the largest operational tokamak in the United States. There are eight NBI systems at DIII-D available for heating the plasma. Also, two types of RF heating are available: ion cyclotron resonance heating (ICRH) and electron cyclotron resonance heating (ECRH). Fast ion populations can be produced during DIII-D experiments that utilize these heating mechanisms. DIII-D is a well diagnosed tokamak with several fluctuation diagnostic systems that can be used to indirectly study the effects of fast-ion driven instabilities. Diagnostic and plasma information could be relayed to actuators for real-time control of AEs in DIII-D experiments [17–20]. Figure 1.6 shows a cutaway of the DIII-D tokamak.

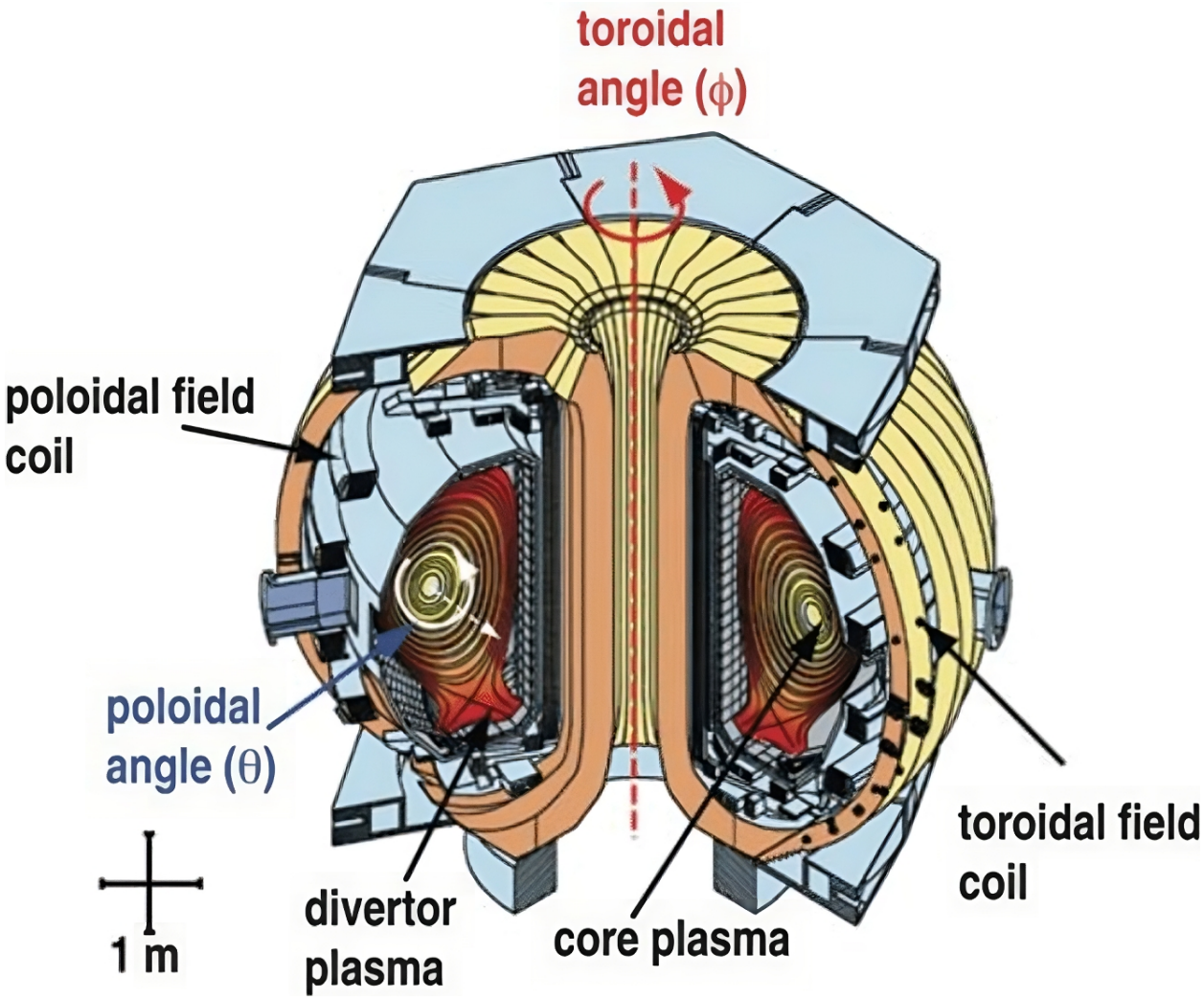

Figure 1.6: A cutaway 3D view of the DIII-D tokamak. The toroidal and poloidal field coils are located outside the walls of the vessel. The divertor region safely extracts lost particles. Figure is from [21]

1.3 Fast Ions

In order to get into the self-sustaining burning plasma regime, NBI and RF heating are commonly used to raise the temperature of the plasma and produce fusion reactions. Fast ions are a type of energetic particle born from these processes with the following gyroradius and speed ordering [22]:

$$\begin{aligned} &\rho_f \gg \rho_i \gg \rho_e \\ &v_e \gg v_f \gg v_i \ , \end{aligned} \tag{1.6}$$

where the subscripts f, i and e denote fast ion, thermal ion and thermal electron, respectively. The energy of thermal ions can be between 1 keV to 10 keV, and fast ions are commonly between 50 keV to 100 keV. In ITER-like burning plasmas, fast ions are expected to have energies in the MeV range.

Distribution functions are used to describe thermal and fast ions. An arbitrary distribution function, F, depends on position, $\mathbf{r}$, and velocity, $\mathbf{v}$ (plus time, t). The background thermal plasma is relatively simple since it can be described using a thermal Maxwellian distribution function. On the other hand, the fast-ion distribution function is anisotropic without a functional form. The spatial component of the fast-ion distribution function can be expressed in cylindrical coordinates: radius R, elevation Z, and toroidal angle ϕ. Since tokamaks can be considered an axisymmetric device, the toroidal angle is usually omitted and fast ions can be described using only R and Z. The velocity component is usually described in the guiding center coordinate system with respect to the magnetic field: energy E, pitch $p = v_\parallel/v$, and gyroangle γ. Since the gyroangle is assumed to be uniformly distributed over 0 to 2π, this dimension is omitted and the fast-ion distribution function is reduced to four dimensions (E, p, R, Z). Figure 1.7 shows an example of a fast-ion distribution function studied in chapter 2.

Poorly behaved fast ions can create issues for the prospects of an ignited burning plasma. Fast ions can resonate with a class of plasma wave instabilities called Alfvén eigenmodes [23]. Resonant fast ions can transfer energy to the wave, drive the plasma unstable and degrade energy confinement [24, 25]. Also, particle redistribution can expel fast ions from the plasma [24–30] and damage the inner walls of the vessel [31, 32]. Uncontrolled fast ions transfer less energy to the thermal plasma and deteriorate fusion performance. Understanding the distribution of fast ions and their interactions with AEs is an important field of research.

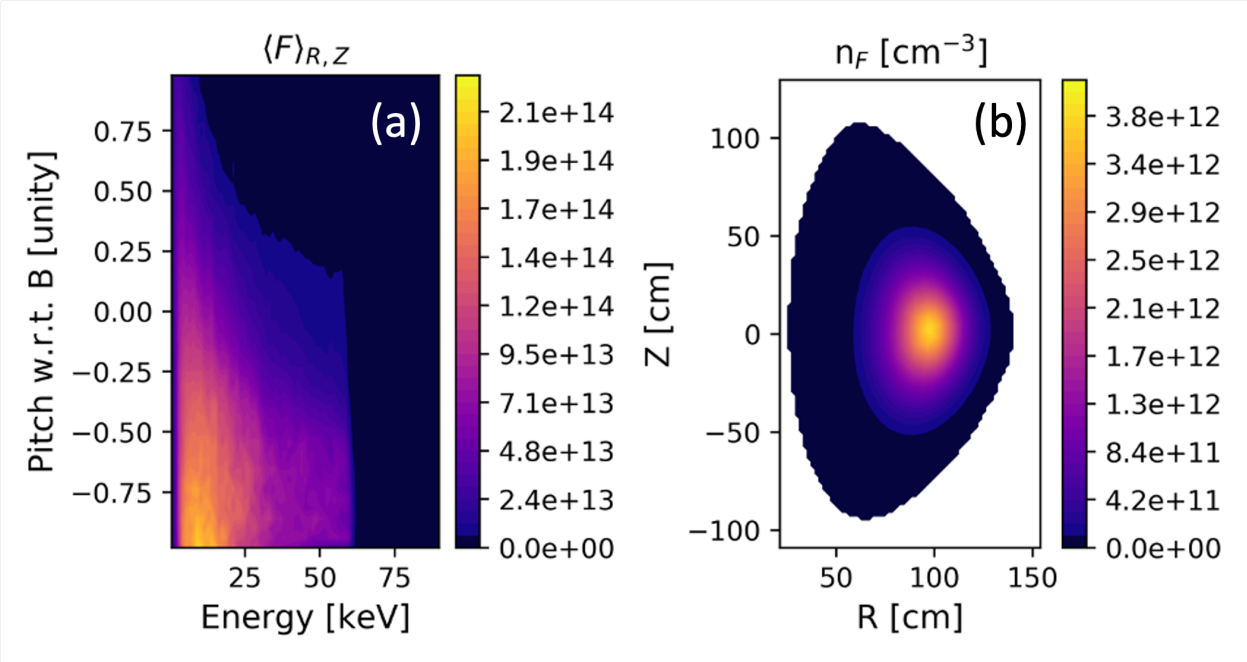

Figure 1.7: An example fast-ion distribution function for an actual Mega Amp Spherical Tokamak (MAST) discharge #29908, which is studied in greater detail in section 2.6. Since the distribution function is multi-dimensional, projections are plotted here for visualization purposes. Panel (a) shows integration over spatial coordinates R and Z and projection onto (E, p)-space. Panel (b) shows the fast-ion density (integration over velocity space).

1.4 Outline

This dissertation is a computationally oriented project in energetic particle research primarily focused on three areas:

- Development of 3 MeV proton weight functions (verified on MAST-U)
- Conceptual design of Spin Polarized Fusion Experiments at DIII-D
- Machine learning-based classification of fast-ion driven instabilities at DIII-D

Chapter 2 discusses the phase-space sensitivity of 3 MeV proton diagnostics and the implementation of the algorithm into the FIDASIM framework [33–35]. Chapter 3 uses the tools developed for the 3 MeV proton weight calculations and generalizes them to produce Charged Fusion Product (CFP) diagnostic signals for the conceptual design of spin polarized fusion experiments at DIII-D. Chapter 4 builds Artificial Intelligence (AI) to detect AEs using CO_2 Interferometer data and expert-made labels on DIII-D. The first four appendices provide supplementary details for chapter 3 and discuss: A) numerical methods used to calculate CFP signals in the high T_i scenario, B) the generalization of the velocity-space probability factor originally calculated for beam-plasma signals produced from D-D reactions, C) the implementation of the CFP algorithm in FIDASIM, and D) an alternative method to more accurately assess uncertainties in the CFP calculations. Appendix E comments on Machine Learning methods that were initially used to detect AEs prior to the training of Recurrent Neural Networks discussed in chapter 4.

Chapter 2

Velocity-space Weight Function of 3 MeV Protons

2.1 Introduction

The weight function plays a key role in Energetic Particle research. The weight function $W(X)$ describes the sensitivity to phase-space variables X of a diagnostic signal and is used in forward modeling of expected signals [33], in tomographic inversions to infer the distribution function [36] and for qualitative interpretation of experimental dependencies [37]. Mathematically, W determines which portions of the energetic particle distribution function $F(X)$ contribute to a measured signal C,

$$C = \int W(X)F(X)\,dX. \tag{2.1}$$

Weight functions have already been developed for many fast-ion diagnostics such as fast-ion D-alpha (FIDA) [38, 39], collective Thomson scattering [40], neutral particle analyzer (NPA) [33, 41], neutron [42–44], gamma-ray [45, 46] and fast-ion loss detector [47] diagnostics. In the

present work, an algorithm to calculate W for a 3 MeV proton diagnostic such as the one at MAST [48] is developed. To date, the majority of these weight functions were developed for two-dimensional velocity space but recent work [39] utilizes three-dimensional orbit weight functions.

In the $\sim$ 0.4 T field of MAST, the 3-MeV proton gyroradius is so large that ions escape in (approximately) one half of a gyro-orbit. Although we specifically consider the MAST diagnostic installation, the algorithm developed here applies equally to more complicated situations, such as the 3-MeV proton orbits that were used to measure d-d spatial profiles during lower hybrid and neutral beam heating in the 5 T Princeton Large Torus [49]. It should also be noted that the basic algorithm applies to any escaping charged fusion reaction product, including the 1.0 MeV triton produced in d-d reactions and the 15 MeV proton produced in d-^{3}He reactions.

The MAST diagnostic measures 3 MeV protons produced in d(d,p)t fusion reactions between fast ions and thermal deuterons in the plasma core. (As discussed below, protons are also produced in beam-beam and thermonuclear reactions.) The emitted protons escape the tokamak on curved orbits, pass through a collimating structure, and are detected. Conceptually, the calculation is analogous to calculation of the weight function of a neutron spectrometer but there are complications. Unlike with neutrons, photons, or neutrals, the "sightlines" are curved trajectories that depend upon the proton velocity; the orbit curvature also alters the solid angle accepted by the collimator. A further complication is that the energy of the emitted proton depends upon the velocities of the reactants and the direction of emission, so the "sightline" itself depends upon the reaction kinematics, with the consequence that different proton energies probe different volumes in both velocity and configuration space. Because the d-d reaction is anisotropic, the reaction probability also depends upon these velocities.

The presented algorithm takes all of these complications into account. Section 2 provides

an overview of the approach. Section 2.3 explains how to compute the effective solid angle of the curved "sightlines" that are accepted by the collimating structure. Calculation of the rate of relevant d-d reactions involves two steps: the basic reaction rate (Sec. 2.4.1) and determination of the portion of the fast-ion population that produces a proton with the measured energy and trajectory (Sec. 2.4.2). The computational approach adopted to calculate these weight functions is described in Sec. 2.5, followed by verification of the calculations in Sec. 2.6. Section 2.7 contains formulas for velocity-space and orbit weight functions and shows an example for a MAST detector. Conclusions appear in Sec. 2.8.

2.2 Formulation of the problem

If the signal-to-noise ratio of the instrument permits, the measured quantity is an energy-resolved count rate at the detector. We express the d-d reaction in standard nuclear physics notation 2(1,3)4, where particle 2 is the thermal deuterium, particle 1 is the fast ion, particle 3 is the 3-MeV proton, and particle 4 is the triton. Our concern is the d(d,p)t reaction so $m_1 = m_2 = 2m_p$, $m_3 = m_p$ and $m_4 = 3m_p$, with m_p the proton mass. The measured energy-resolved count rate is $C(E_3, \Delta E_{bin})$, where E_3 is the proton energy and ΔE_{bin} is the energy resolution of the measurement.

A limitation of the present work is that the calculated weight function applies exclusively to reactions between an energetic "fast-ion" population and a slower, thermal population. In other words, the fast-ion (particle 1) is the beam, particle 2 is a thermal deuterium reactant, particle 3 is the measured 3-MeV proton, and particle 4 is undetected. This type of reaction is customarily called "beam-plasma" in fusion research. In reality, "beam-beam" reactions between pairs of fast ions and "thermonuclear" reactions between pairs of thermal deuterons also occur; in both of these situations, the two reacting ions often have comparable speeds. Since the beam-plasma reaction rate depends linearly on the fast-ion distribution function,

its weight function is well-suited for tomographic inversion to infer the distribution function using standard matrix methods; this is not true for beam-beam reactions. However, on two devices where 3-MeV proton diagnostics are currently implemented or planned, MAST-U [48] and NSTX-U [50], beam-plasma reactions predominate. For example, in the L-mode NSTX-U plasma of [51], beam-beam reactions constitute $< 11\%$ and thermonuclear reactions constitute $< 1\%$ of the total rate. Similarly, in the MAST experiments of [52], beam-beam reactions constituted $\sim 10\%$ of the total.

Since the escaping proton orbits are essentially collisionless (fractional energy change $< 10^{-6}$), the phase-space volume accepted by the detector can be related to the phase-space volume traversed by the curved "sightlines," so the measured count rate is [53]

$$C(E_3, \Delta E_{bin}) = \int\int\int dl\, dA\, d\Omega\, S(\mathbf{r}, \mathbf{v}_3), \tag{2.2}$$

where $\int dl$ represents integration over the sightline, $\int dA$ represents integration over the detector area, $\int d\Omega$ represents integration over the solid angle accepted by the collimating structure, and $S(\mathbf{r}, \mathbf{v}_3)$ represents the emissivity (in reactions/volume-time) of protons that are emitted at position $\mathbf{r}$ along the sightline with the correct values of E_3 and solid angle. As in the formulation of the weight function for a neutron collimator [42], the emissivity can be divided into two pieces, one piece that describes the d-d reactivity for the selected reaction kinematics, and another piece that describes the number of fast ions that can produce a proton with the velocity $\mathbf{v}_3$ accepted by the specified sightline,

$$S(\mathbf{r}, \mathbf{v}_3) = \int d\mathbf{v}_1 \int d\mathbf{v}_2\, R(\mathbf{v}_1, \mathbf{v}_2, \mathbf{v}_3, \mathbf{r}) p_{gyro}(\mathbf{v}_1, \mathbf{v}_2, \mathbf{v}_3) f_1(\mathbf{v}_1, \mathbf{r}) f_2(\mathbf{v}_2, \mathbf{r}). \tag{2.3}$$

The emissivity R depends upon the d-d cross section (including anisotropy), the relative velocities of the reactants $|\mathbf{v}_1 - \mathbf{v}_2|$, and the emitted proton's velocity $\mathbf{v}_3$. In Sec. 2.4.1, the integration over the distribution function f_2 of the target deuterons is incorporated

into the emissivity R, making R a function of the ion temperature T_i, the rotation velocity $\mathbf{v}_{rot}$, and the deuterium target density n_d. In this work, the fast-ion distribution function f_1 is represented by a guiding-center distribution function $F(v_\parallel, v_\perp, \mathbf{r})$; the third velocity coordinate, the gyroangle γ associated with the fast gyromotion, is assumed of uniform probability and is not explicitly shown. (Here, $v_\parallel$ is the component of the fast-ion velocity along the magnetic field $\mathbf{B}$ and $v_\perp$ is the magnitude of the perpendicular velocity.)

The function $p_{gyro}(\mathbf{v}_1, \mathbf{v}_2, \mathbf{v}_3)$ represents the probability density that the gyroangle of the fast ion has the correct value to produce the measured proton. In practice, it is advantageous [42] to consider intervals of speed v_3 (or proton energy E_3). If v_3 is interpreted this way, p_{gyro} represents the probability that the selected fast ion has a gyroangle that produces protons within the specified range of speeds.

Recall from Eq. 2.1 that the weight function is defined through the relation $C(E_3) = \int W(X, E_3) F(X)\, dX$. The goal of the following sections is to simplify and rearrange Eqs. 2.2 and 2.3 into the form of Eq. 2.1 in order to extract the weight function W. To that end, the next section explains how to simplify and calculate the $\int\int\int dl\, dA\, d\Omega$ term that describes the sightlines and collimating structure. The emissivity R is simplified in Sec. 2.4.1 and formulas for the probability p_{gyro} are given in Sec. 2.4.2.

2.3 "Sightlines" selected by the collimating structure

The treatment of the sightlines follows [53]. Figure 2.1 illustrates the bundles of "rays" collected by four MAST proton detectors in a particular equilibrium. Owing to the large proton gyroradius in the ~ 0.4 T MAST field, protons escape before they complete a full gyro-orbit. Although the effective solid angle is largest for a central sightline, protons have a finite probability of striking the detector for a range of different incident velocity vectors.

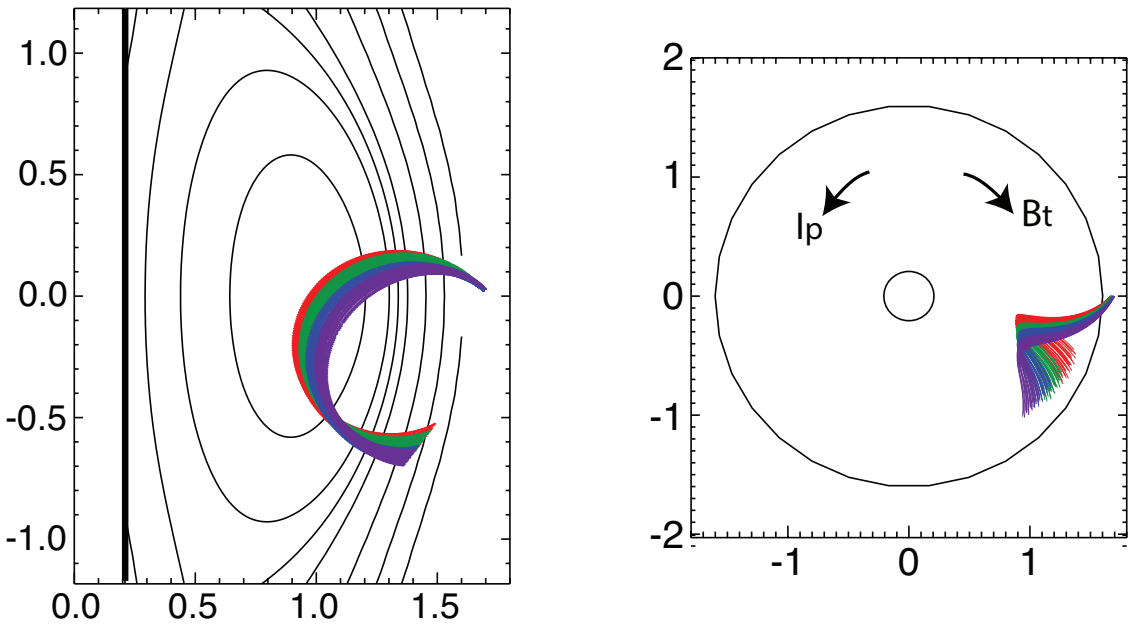

Figure 2.1: Elevation (left) and plan (right) views of 3.03 MeV proton orbits (colors) that reach the four MAST proton detectors in a particular equilibrium. The thickness of the lines is proportional to the effective transmission T. The black lines in the elevation represent flux surfaces (thin lines) and the inner wall of the vacuum vessel (thick line). The directions of plasma current I_p and toroidal field B_T are also indicated.

A full orbit code that integrates the equations of motion with an Adams-Bashford-Moulton scheme calculates the trajectory represented by $\int dl$. Since the orbit is collisionless, time is reversed in the calculation in order to calculate orbits backward from the detector into the plasma. Each trajectory has an effective weight represented by the product $\int\int dA\, d\Omega$. Since the magnetic field changes little on the scale of the collimating structure, incident orbits with the same velocity can be considered identical over the entire area of the detector. With this approximation, we can replace $\int\int dA\, d\Omega$ by $\mathrm{A}\int T(\Omega)\, d\Omega$, where the transmission function $T(\Omega)$ is proportional to the fraction of the detector area "illuminated" by a particular incident velocity vector.

Define a central velocity vector on the axis of the collimator, i.e., from the center of the aperture to the center of the detector. Our goal is to compute $AT(\Omega)$ for a representative sample of orbits that strike the detector. Consider a cylindrical collimating structure of

radius a and length d (Fig. 2.2a). If the orbits were straight, velocity vectors that tilt from the collimator axis by $\tan(2a/d)$ strike the edge of the detector. Select velocity vectors that travel from the center of the detector to points on the aperture plane. Since the actual orbits are curved, expand the area of the candidate points on the aperture plane by an amount $\delta a = \rho - \sqrt{\rho^2 - d^2}$, where ρ is the gyroradius, ensuring that all possible velocity vectors are considered. Use the sunflower algorithm that includes judiciously selected boundary points [54] to uniformly sample velocity vectors on this plane. (The sunflower arrangement uses golden ratios for angle increments and square roots for radius increments.) For each velocity vector, calculate the actual orbit between the aperture plane and the center of the detector. Next, to determine the fraction of the detector area "illuminated" by this velocity, use the sunflower algorithm to uniformly sample positions on the detector plane. Shift the orbit to various positions on the detector plane to calculate the fraction of the detector area that is illuminated by this velocity vector. Figure 2.2b shows the portion of the detector area illuminated by a particular incident velocity vector. This fraction is proportional to the desired transmission function $T(\Omega)$.

To check the accuracy of this calculation, replace the actual curved orbits with straight orbits. In this case, for small a/d, the program correctly calculates that $\int\int dA\, d\Omega = (\pi a^2)^2/d^2$, a familiar result in geometrical optics.

The output of this calculation is a set of velocity vectors at the detector that have non-zero transmission weights T. For each of these velocity vectors, follow the proton orbit backwards in the equilibrium field. For each channel, this bundle of curved trajectories constitutes the detector field of view or "sightline."

Note that the measured sightlines depend upon the proton energy. Typical changes in energy (Sec. 2.4) shift the trajectory through the plasma by a few centimeters radially (Fig. 2.3). Although the shift is modest, the fast-ion distribution function often has a large density gradient, so the shift in orbit must be properly treated. The transmission factors T also

depend upon proton energy (Fig. 2.4), so this dependence is also taken into account.

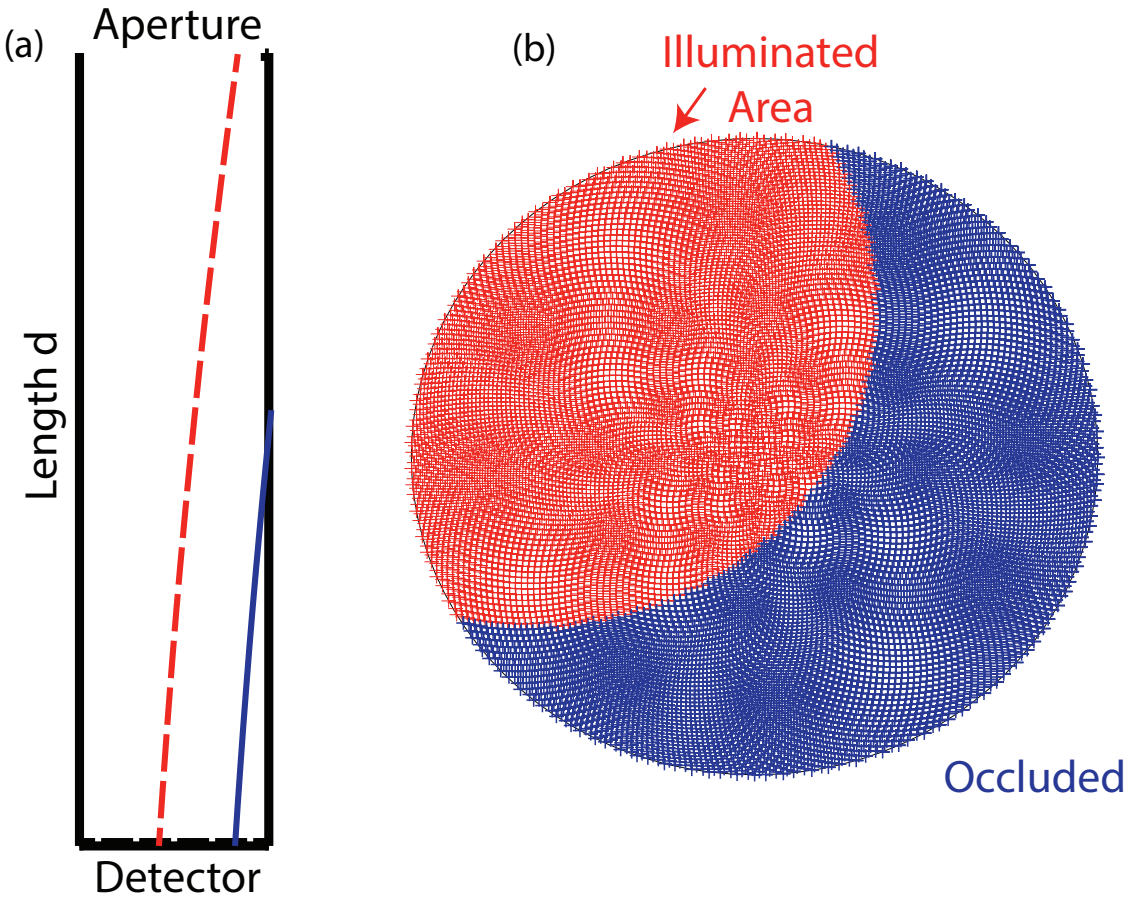

Figure 2.2: (a) Schematic diagram of a cylindrical collimator. For a given orientation of the incident proton velocity, some orbits reach the detector (red), while others do not (blue). (b) For a given incident velocity vector, only the red portion of the detector is illuminated. The figure also shows the sunflower sampling of the detector area.

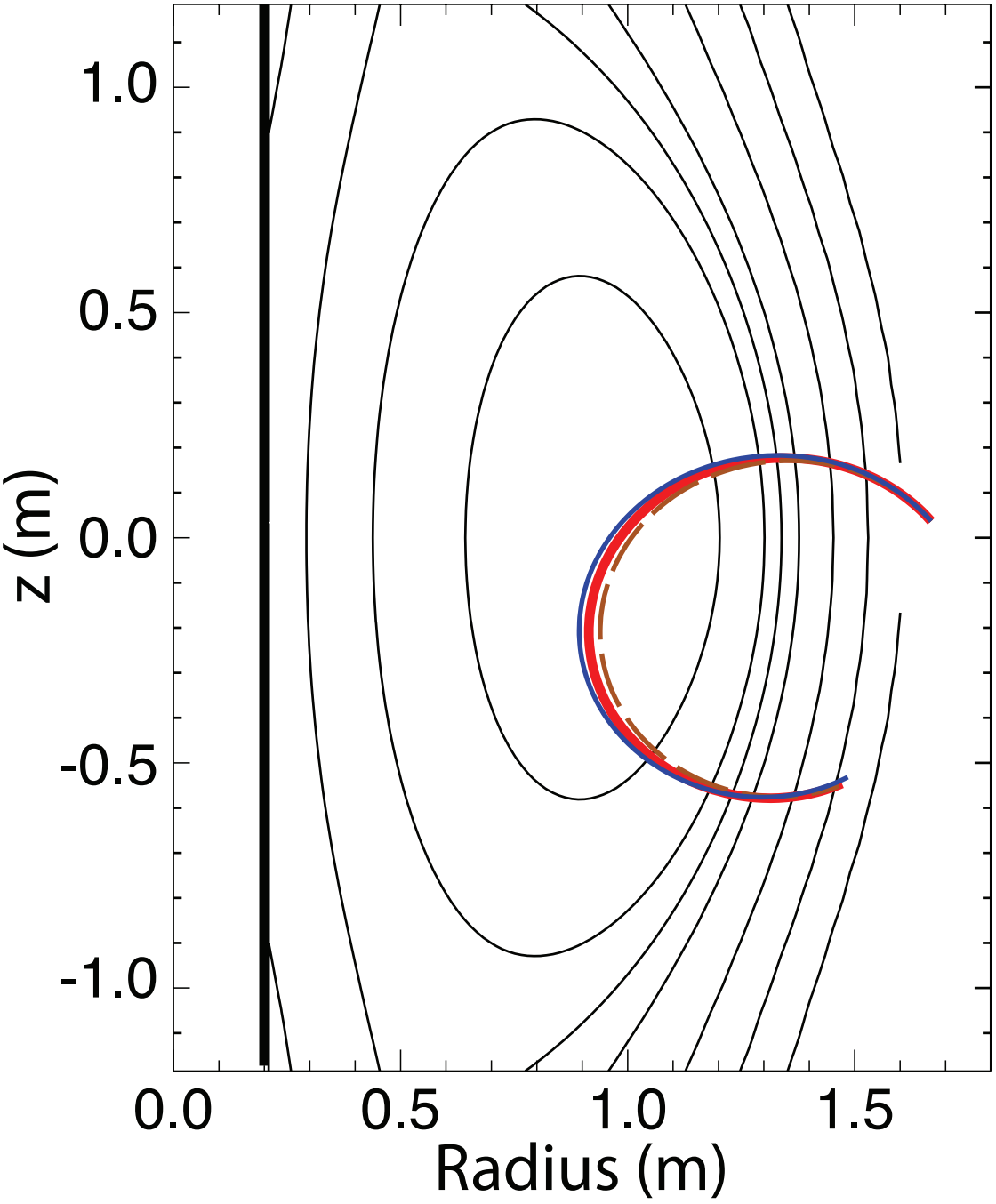

Figure 2.3: (R, z) projection of orbits that enter the detector with the same orientation for energies of 2730 (brown), 3030 (red), and 3330 keV (blue). The orbit shifts a few centimeters.

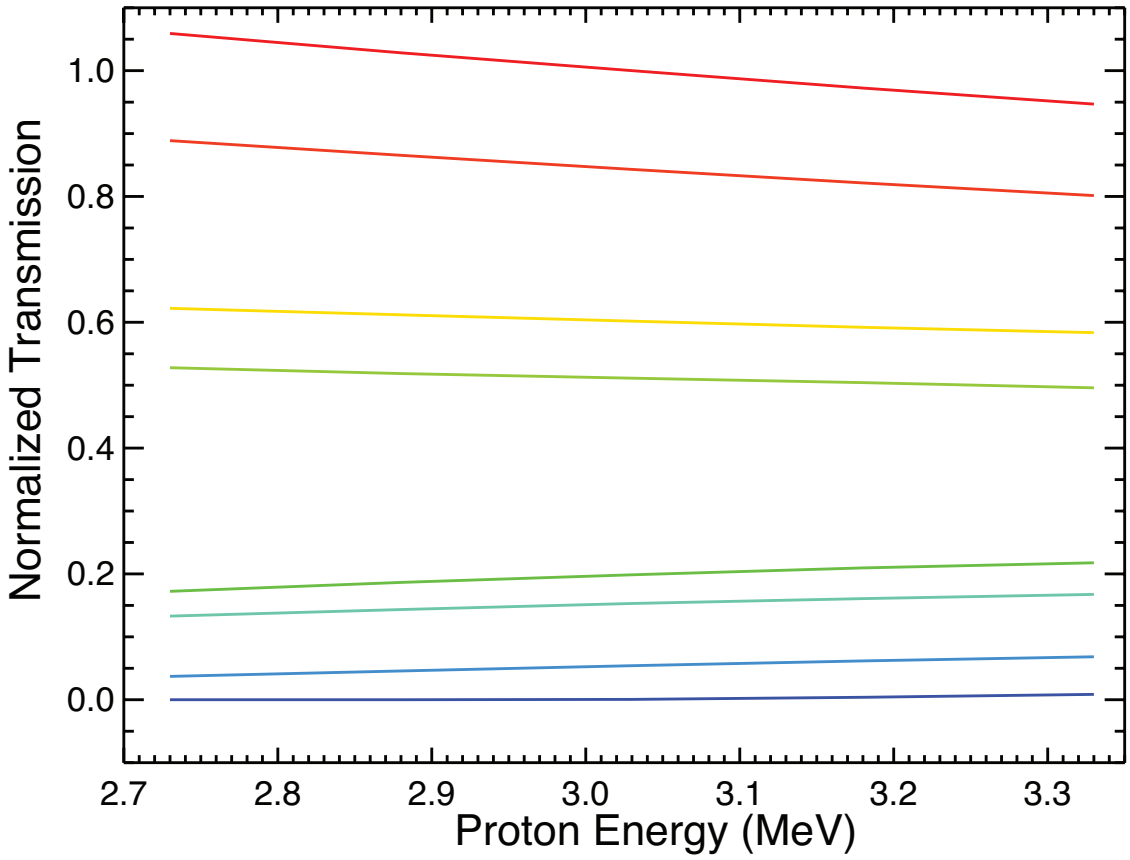

Figure 2.4: The overall transmission of the collimator increases with energy because the incident orbits are straighter. A variety of different incident velocity vectors are shown. The curves are normalized to the transmission of the maximum velocity vector for $E_3 = 3.03$ MeV.

2.4 Reaction kinematics and probability

For the reaction 2(1,3)4, particle 2 is the thermal deuterium, particle 1 is the fast ion, particle 3 is the 3-MeV proton, and particle 4 is the triton. The energy of the proton (Eq. 29 of [55]) is

$$E_3 = \frac{3}{4}(Q+K) + V\cos\theta\sqrt{\frac{3}{2}(Q+K)m_p} + \frac{1}{2}m_p V^2, \tag{2.4}$$

where $Q = 4.04$ MeV, $K = \frac{1}{2}m_p|\mathbf{v}_1 - \mathbf{v}_2|^2$, $\mathbf{V} = \frac{1}{2}(\mathbf{v}_1 + \mathbf{v}_2)$ is the center-of-mass velocity, and θ is the angle between $\mathbf{V}$ and the proton velocity in the center-of-mass frame $\mathbf{v}_3'$.

For a 100 keV deuterium beam (a relatively large value for positive neutral beam sources) interacting with typical values of $\mathbf{v}_2$, $K \lesssim 0.05$ MeV, a small value.

The first term on the right-hand side (RHS) of Eq. 3.2 gives the nominal proton energy of 3.03 MeV. The shift in energy from the nominal value is determined almost entirely by the middle term on the RHS. The largest absolute value of the middle term occurs for $\cos\theta = \pm 1$, so the shift in energy of the proton from the nominal 3.03 MeV value is

$$\Delta E_3 \simeq \frac{1}{2}v_1\sqrt{\frac{3}{2}Qm_p} = \frac{1}{2}\sqrt{\frac{3}{2}E_1 Q} \lesssim 0.39 \text{ MeV}, \tag{2.5}$$

for $E_1 = m_p v_1^2 = \frac{1}{2}m_D v_1^2 \simeq 0.10$ MeV. This implies that the fractional change in energy is $\Delta E_3/E_3 \lesssim 13\%$. Equation 2.5 determines the energies E_3 for which the proton spectrum is calculated.

At any particular location in the plasma, both the orientation and energy of the proton is known, so the proton velocity vector in the lab frame $\mathbf{v}_3$ is a known quantity in the following calculations.

2.4.1 Emissivity R

The goal of this subsection is to simplify the fusion emissivity $R(\mathbf{v}_1, \mathbf{v}_2, \mathbf{v}_3, \mathbf{r})$ that appears in Eq. 2.3.

There are three relevant rest frames. The proton velocity $\mathbf{v}_3$ is known in the lab frame. The effect of the target distribution function $f_2(\mathbf{v}_2)$ on the reaction rate is most easily computed in the rotating plasma frame. The effect of anisotropy is known in the center-of-mass frame.

The first step is to eliminate the integral over $\mathbf{v}_2$ that appears in Eqs. 2.2 and 2.3. After integrating over the Maxwellian target distribution, $\int \sigma(v_{rel}) v_{rel} f_2(\mathbf{v}_2, \mathbf{r})\, d\mathbf{v}_2$ becomes $n_d \langle \sigma v \rangle$, where n_d is the deuterium density and $\langle \sigma v \rangle$ is the averaged reactivity. (Here, the relative velocity is $v_{rel} \equiv |\mathbf{v}_1 - \mathbf{v}_2|$.) Both n_d and $\langle \sigma v \rangle$ are functions of position. In the plasma frame, the velocity of the fast ion is $\mathbf{v}_1^{pl} = \mathbf{v}_1 - \mathbf{v}_{rot}$. To evaluate $\langle \sigma v \rangle$ we use Eqs. 8 and 9 of Bosch and Hale [11], using the coefficients given in their Table IV for the cross-section σ, with v_1^{pl} for the projectile speed, and average σv over a Maxwellian target that has temperature T_i. The resulting $\langle \sigma v \rangle$ is a function of $\mathbf{v}_1$, $\mathbf{v}_{rot}$, and T_i.

The d(d,p)t reaction is anisotropic. Brown and Jarmie [56] parameterize the differential cross section in the center-of-mass frame by

$$\sigma(\theta) = a + b \cos^2 \theta + c \cos^4 \theta. \tag{2.6}$$

The coefficients a, b, and c are functions of energy and are given in their Table I. We know θ from

$$\cos \theta = \frac{\mathbf{V} \cdot \mathbf{v}_3'}{V v_3'}, \tag{2.7}$$

where the center-of-mass velocity $\mathbf{V}$ is

$$\mathbf{V} = \frac{1}{2}(\mathbf{v}_1 + \langle \mathbf{v}_2 \rangle) \simeq \frac{1}{2}(\mathbf{v}_1 + \mathbf{v}_{rot}) \tag{2.8}$$

and $\mathbf{v}_3' = \mathbf{v}_3 - \mathbf{V}$ is the proton velocity in the center-of-mass frame.

The relative velocity in the center-of-mass frame is $2v_1'$, where $\mathbf{v}_1' = \mathbf{v}_1 - \mathbf{V}$ is the beam velocity in the center-of-mass frame. To get the Brown-Jarmie coefficients for this particular reaction use the relative energy to interpolate for a, b, and c. Our goal is to compute the effect of anisotropy on the Bosch-Hale value of $\langle \sigma v \rangle$ we have already found. If the reaction was isotropic, the integral of the differential cross section over θ gives a total cross section that is proportional to $a + b/3 + c/5$, so the anisotropy enhancement/deficit factor is

$$\kappa = \frac{a + b\cos^2\theta + c\cos^4\theta}{a + b/3 + c/5}. \tag{2.9}$$

Therefore, the reactivity for this reaction is $\kappa\langle \sigma v \rangle$ and the emissivity is $n_d \kappa \langle \sigma v \rangle$.

2.4.2 Calculating p_{gyro}

The goal of this subsection is to determine the number of fast ions in velocity space that can produce a reaction with the specified value of $\mathbf{v}_3$.

Jacobsen *et al.* [42] calculated velocity-space weight functions for neutron spectroscopy using the d(d,n)^{3}He reaction. Since $\mathbf{v}_3$ is known, they found that the calculation is simpler in the lab frame than in the center-of-mass frame. For simplicity, they assumed negligible target velocity ($\mathbf{v}_2 = 0$) in their treatment of the reaction kinematics (but *not* in the calculation of R discussed in the previous subsection). In the following, we do not make this assumption but ultimately conclude that it is justified for typical parameters.

Following the derivation of Jacobsen *et al.*, the weight function for a particular fast ion with velocity $(v_\perp, v_\parallel)$ [or (energy,pitch)] is proportional to a factor proportional to the reaction rate and a kinematics-dependent velocity-space factor. Symbolically, the velocity-space weight function $w(E_{p1}, E_{p2}, \phi, v_\parallel, v_\perp, \mathbf{v}_{rot}, \mathbf{r})$ is found for emitted proton energies between E_{p1} and E_{p2} that are emitted at an angle ϕ with respect to the magnetic field by a reaction between a fast ion with parallel and perpendicular velocities $v_\parallel$ and $v_\perp$ and target ions that rotate at $\mathbf{v}_{rot}$ and have temperature T_i at the spatial location $\mathbf{r}$. This weight function is the product of a reaction rate and a conditional probability p_{gyro} that depends upon the reaction kinematics,

$$R(\phi, v_\parallel, v_\perp, \mathbf{v}_{rot}, T_i) \times \text{prob}(E_{p1} < E_3 < E_{p2} | \phi, v_\parallel, v_\perp, \mathbf{v}_{rot}). \tag{2.10}$$

For the conditional probability, two components of the fast-ion velocity $\mathbf{v}_1$ are known but the third component, the gyroangle γ, is not. The goal of the kinematics calculation is twofold: (1) Find which gyroangles can produce a proton with the specified value of $\mathbf{v}_3$ and (2) determine the value of $\cos\theta$ to use in Eq. 2.9. Since gyromotion is assumed uniform, the fraction of fast ions p_{gyro} with the specified values of $(v_\perp, v_\parallel)$ that can produce this proton is equal to

$$p_{gyro} = \frac{\Delta\gamma}{2\pi}, \tag{2.11}$$

where $\Delta\gamma$ represents the range of gyroangles that produces protons in a specified energy range, $E_{p,1} < E_3 < E_{p,2}$.

Including the plasma rotation but assuming zero temperature of the target species, the equations of energy and momentum conservation in the lab frame are

$$\frac{1}{2}m_1 v_1^2 + \frac{1}{2}m_2 v_{rot}^2 + Q = \frac{1}{2}m_4 v_4^2 + \frac{1}{2}m_3 v_3^2 \tag{2.12}$$

and

$$m_1\mathbf{v}_1 + m_2\mathbf{v}_{rot} = m_3\mathbf{v}_3 + m_4\mathbf{v}_4. \tag{2.13}$$

Use momentum conservation to eliminate v_4 in Eq. 2.12 and replace the masses with their values for the d(d,p)t reaction. Introduce coordinates $(\hat{a}, \hat{b}, \hat{c})$ where $\hat{b}$ is along the magnetic field, $\hat{a}$ is oriented along the perpendicular component of the emitted proton, and $\hat{c}$ is orthogonal to the other unit vectors. Choose the origin of the fast-ion gyroangle γ so $\cos\gamma = 1$ when the gyroangle is aligned with $\hat{a}$. The fast-ion velocity is

$$\mathbf{v}_1 = \hat{b}v_\parallel + \hat{a}v_\perp \cos\gamma + \hat{c}v_\perp \sin\gamma, \tag{2.14}$$

the proton velocity is

$$\mathbf{v}_3 = \hat{b}v_3 \cos\phi + \hat{a}v_3 \sin\phi \tag{2.15}$$

and the rotation velocity is

$$\mathbf{v}_{rot} = \hat{b}v_b + \hat{a}v_a + \hat{c}v_c. \tag{2.16}$$

After substitution, the equation for the gyroangle is

$$\begin{aligned} v_\perp \left(\sin\phi - \frac{2v_a}{v_3}\right)\cos\gamma = \; & v_3 - \frac{3Q}{2v_3 m_p} - (v_\parallel + v_b)\cos\phi \\ & - v_a \sin\phi - \frac{1}{2}\frac{v_1^2 + v_{rot}^2}{v_3} + \frac{2v_b v_\parallel}{v_3} \\ & - \frac{v_{rot}^2}{2v_3} + \frac{2v_c v_\perp \sin\gamma}{v_3}. \end{aligned} \tag{2.17}$$

Since the last term on the right-hand side (RHS) is quite small, this equation is easy to solve iteratively for $\cos\gamma$.

For the anisotropy calculation, $\cos\theta$ is given by Eq. 2.7. All of the needed velocities are known.

In practice, the rotation velocity can be neglected in the calculation of γ and $\cos\theta$. Since Eq. B.1 is solved for $\cos\gamma$, both a positive gyroangle γ_+ and a negative gyroangle γ_- satisfy the equation. If rotation is neglected, these angles are equal and opposite. With rotation, the final term in Eq. B.1 that is proportional to $\sin\gamma$ causes an asymmetry between positive and negative gyroangles. However, as shown in Fig. 2.5a, even for a relatively large rotation velocity of 2×10^5 m/s, the difference in these angles is very small. Similarly (not shown), the center-of-mass angle $\cos\theta$ depends very weakly on the sign of γ.

To get p_{gyro}, we want to calculate a pair of gyroangles γ for two energies $E_{p,1}$ and $E_{p,2}$; this gives us an effective width in velocity space. (We actually want to calculate this pair for both γ_+ and γ_- but, since $\gamma_+ \simeq \gamma_-$, we can restrict the calculation to γ_+ and double its probability.) Note that we do *not* want to calculate γ for two actual orbits with different E_3. Instead, we are interested in the *velocity-space* spread of fast-ion gyroangles that produce protons in a specified energy bin ΔE_{bin}. Use Eq. B.1 to find γ_{high} for $E_{p,1} = E_3 + \Delta E_{bin}/2$ and γ_{low} for $E_{p,2} = E_3 - \Delta E_{bin}/2$. The gyroradius probability factor is

$$p_{gyro} \simeq \frac{|\gamma_{high} - \gamma_{low}|}{\pi}. \tag{2.18}$$

There are two potential pitfalls in the numerical calculation of γ from Eq. B.1. One pitfall occurs when the factor $v_\perp(\sin\phi - 2v_a/v_3)$ on the LHS of Eq. B.1 is zero. This occurs when the proton is emitted nearly parallel to the magnetic field or when $\mathbf{v}_1$ and $\mathbf{v}_3$ are nearly parallel or anti-parallel to each other; since both of these conditions occupy small velocity-space volumes, we set $p_{gyro} = 0$ for these special cases.

The second pitfall occurs when an energy bin extends beyond the maximum or minimum

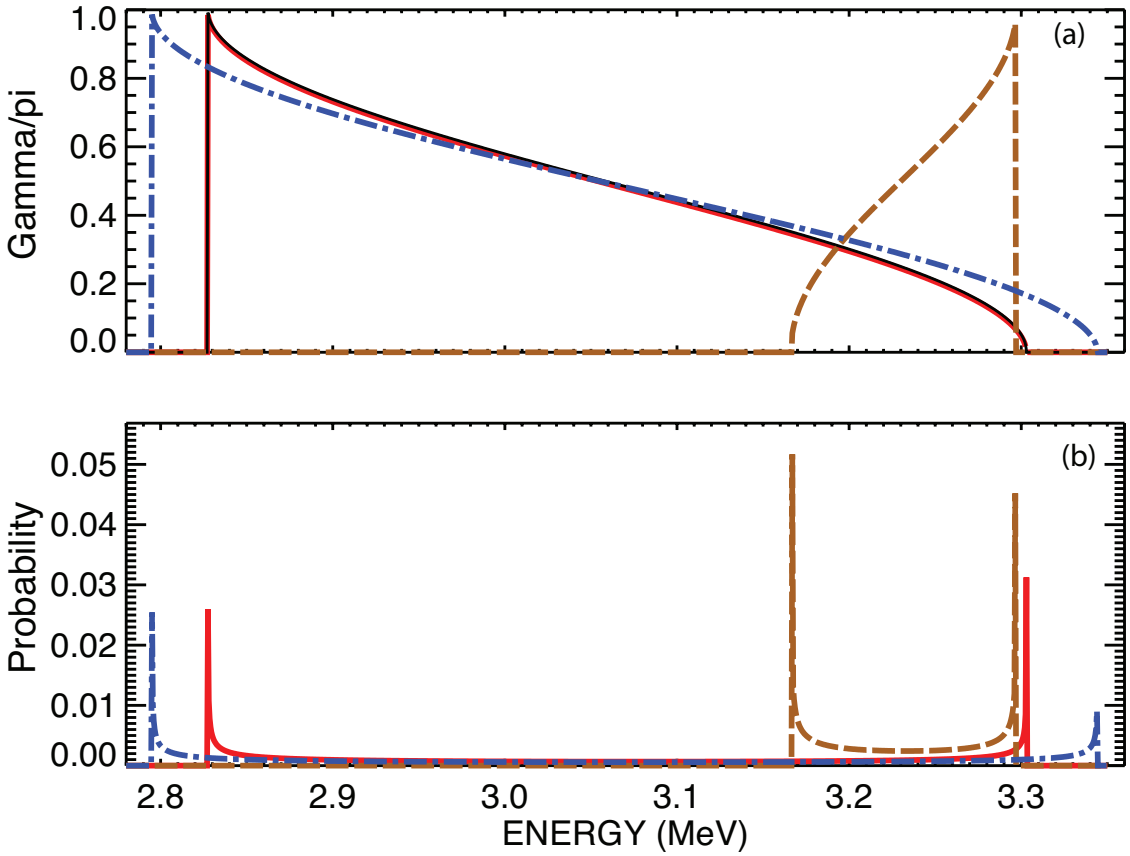

Figure 2.5: Dependence of (a) the absolute value of the normalized gyroangle $|\gamma|/\pi$ and (b) the probability of gyroangles in a specified energy range p_{gyro} on proton energy for $E_1 = 50$ keV and a rotation velocity of 2×10^5 m/s. Solid curves: lab-frame angle $\phi = \pi/2$ and fast ion pitch $v_\parallel/v = 0.5$. Dashed curves: $\phi = -\pi/4$ and $v_\parallel/v = 0.95$. Dot-dashed curves: $\phi = \pi/2$ and $v_\parallel/v = 0$. In (a), for the solid-line case, both γ_+ (red) and γ_- (black) are shown; the curves nearly overlay one another.

values of E_3 that are compatible with the other selected parameters. The maximum and minimum energies occur when the gyroangle is $\gamma = 0$ or $\gamma = \pi$. In these cases, Eq. 2.18 is replaced by $p_{gyro} = \gamma_{bin}$ when $\gamma \simeq 0$ or $p_{gyro} = \pi - \gamma_{bin}$ when $\gamma \simeq \pi$. Here, γ_{bin} is the value of γ evaluated at whichever edge of the energy bin has a value of proton energy permitted by the kinematics.

The maximum and minimum values of E_3 occur when $\cos\gamma \simeq \pm 1$ in Eq. B.1. Use the

quadratic formula to find that the minima and maxima values of the proton speed v_3 are

$$v_3 = \frac{-B + \sqrt{B^2 + 4C}}{2} \tag{2.19}$$

where

$$B = \mp v_\perp \sin\phi - (v_\parallel + v_b)\cos\phi - v_a \sin\phi$$

and

$$C = \frac{3}{2}\frac{Q}{m_p} + \frac{v_1^2 + v_{rot}^2}{2} - 2v_\parallel v_b \mp v_\perp v_a.$$

2.5 Implementation into the FIDASIM framework

Calculation of the 3 MeV proton count rate has been implemented within the framework of the FIDASIM synthetic diagnostic code [33]. Since detailed documentation is available on the FIDASIM GitHub website [57], only a brief summary is provided here.

Data preparation of input files in HDF5 format occurs outside of the framework of the FORTRAN FIDASIM code. As usual, plasma profiles, the fast-ion distribution function, and the equilibrium are prepared using Python or IDL data-preparation routines. The additional input quantities for the 3-MeV proton calculation are the proton sightlines and transmission factors described in Sec. 2.3; they are listed in Table 2.1. The user specifies an array of energies for the proton spectrum. For each detector channel, "nrays" is the number of orbits to consider in the "bundle" of trajectories that strikes the detector. After reading the detector geometry and the equilibrium fields, a Lorentz orbit code calculates the time-reversed orbit (the "sightline") and an IDL code calculates the transmission factor ("daomega") for each specified "ray" for each detector. A typical calculation uses 150 orbital

Table 2.1: New inputs used by FIDASIM in the 3-MeV proton calculation.

Member	Type	Rank	Dimension	Units	Description
nchan	Int	0	Scalar	unity	Number of detector channels
nrays	Int	0	Scalar	unity	Number of "rays"
nsteps	Int	0	Scalar	unity	Maximum number of orbit steps
nenergy	Int	0	Scalar	unity	Number of proton energies
earray	Float	1	[nenergy]	keV	Proton energies
daomega	Float	3	[nenergy,nrays,nchan]	cm^{-2}	Transmission factor
nactual	Float	3	[nenergy,nrays,nchan]	unity	Number of orbital spatial steps
sightline	Float	4	[nenergy,6,nsteps,nrays,nchan]	cm/s cm	Velocity and position in [r,phi,z]

steps, 75 rays, and 11 proton energies.

Figure 2.6 shows a flowchart of the calculation within FIDASIM. After reading the input data, a routine converts the proton orbits (the "sightlines") into the Cartesian coordinate system utilized in FIDASIM. Next, bilinear interpolation is performed to find the fields and plasma parameters at each sightline step. Calculation of the probability factor and gyroangle described in Section 2.4.2 is the first major process in the algorithm. Inputs to subroutine `get_pgyro` are the magnetic field, proton energy, fast-ion energy, fast-ion pitch, plasma rotation and proton velocity. Although the plasma rotation is relatively small in Equation B.1, it is kept in the computations for completeness.

Next, a gyro step is required to get the fast-ion density at the guiding center position. Since the fields, pitch and gyroangle are known, subroutine `pitch_to_vec` calculates the velocity of the fast ion. The velocity, beam mass and fields are then used to determine the guiding center position in subroutine `gyro_step` using the formula for the gyroradius in [58]. Finally, the beam energy and pitch are used to calculate the guiding center fast-ion density at the gyro-step position.

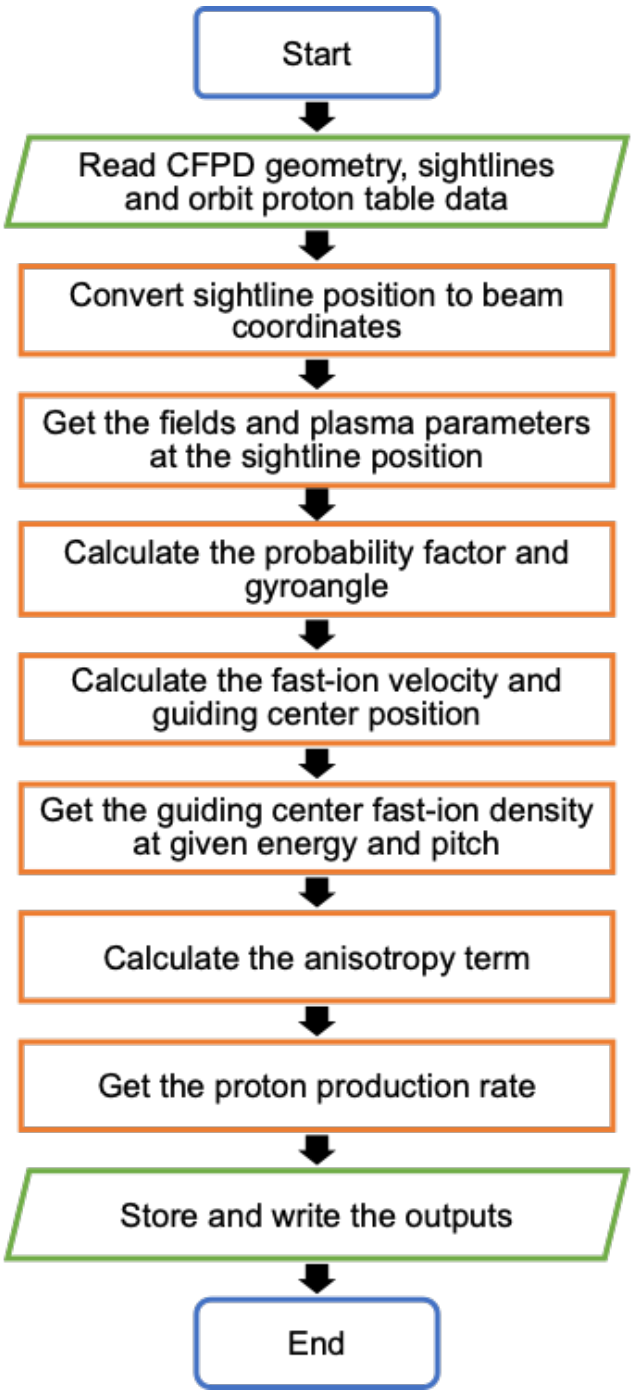

Figure 2.6: Flowchart for the portion of the algorithm that is implemented in the FORTRAN FIDASIM code.

Calculating the reaction rate is the last major process of the algorithm and follows the procedure outlined in Sec. 2.4.1. Linear interpolation is performed to determine the Brown-Jarmie coefficients for the given beam energy. FIDASIM reads in pre-calculated tables for the

neutron and proton branches of the D-D beam-target fusion reaction. Bilinear interpolation is performed to calculate the proton production rate for a given thermal ion temperature and relative velocity between the fast ion and rotation velocities. Finally, the rate is multiplied by the thermal deuterium density.

After looping over detector channels, proton energies, orbit rays, and orbit steps, the code outputs proton spectra for each detector channel.

2.6 Code verification

This section discusses the selection of numerical parameters, the sensitivity of the output to two physics effects, and tests that verify that the code works properly. Two different sets of inputs that are representative of the MAST diagnostic installation are used for these tests. The first set is an artificial case that Netepenko used for the tests described in his Ph.D. thesis [50]. The second is for an actual MAST discharge, #29908. In both cases, the equilibrium is provided by EFIT [59] and the plasma parameters and distribution function are from TRANSP [60].

An initial test found that 5 proton energies is insufficient to resolve the proton spectrum but 13 energies provides adequate resolution. Increasing the number of orbital steps and number of rays did not significantly affect the results but slowed down the algorithm. Thus, nsteps=110 and nrays=50 are used in the following section.

In order to quantify the importance of the anisotropy correction factor, FIDASIM is run using anisotropic (Eq. 2.9) and isotropic ($\kappa = 1$) cross sections. Figure 2.7 shows that inclusion of the anisotropy of the d-d cross section makes a small difference of 4% for an injection energy of 50 keV for MAST conditions. Because many protons are emitted near the center-of-mass angle $\theta \simeq \pi/2$, where anisotropy reduces the cross section, the isotropic calculation is

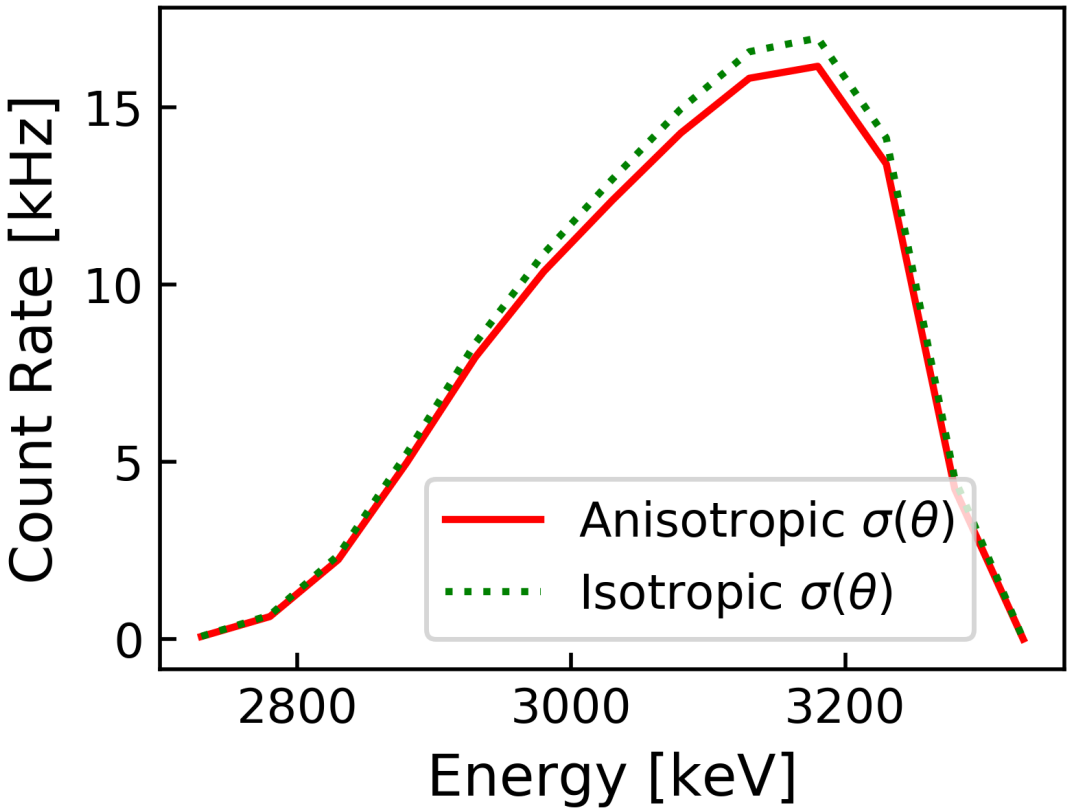

Figure 2.7: Comparison of the proton energy spectrum calculated using the actual anisotropic d-d cross section (solid curve) with a calculation that ignores cross-section anisotropy (dashed).

slightly higher. Since the effect of anisotropy grows with increasing energy, proper treatment of cross-section anisotropy is more important in facilities with higher injection energies or RF accelerated fast-ion tails.

Figure 2.8 compares the spectrum computed using the actual proton orbits to a calculation that utilizes the same orbits and transmission factors for all proton energies. Because higher-energy protons have larger gyroradii, they originate deeper in the plasma, where the fast-ion and thermal densities are larger and the emissivity is larger. Conversely, lower-energy protons originate closer to the plasma edge where the emissivity is smaller. The result is that proper treatment of the orbits shifts the spectrum to higher energies (Fig. 2.8). The overall effect is modest for the MAST installation, however.

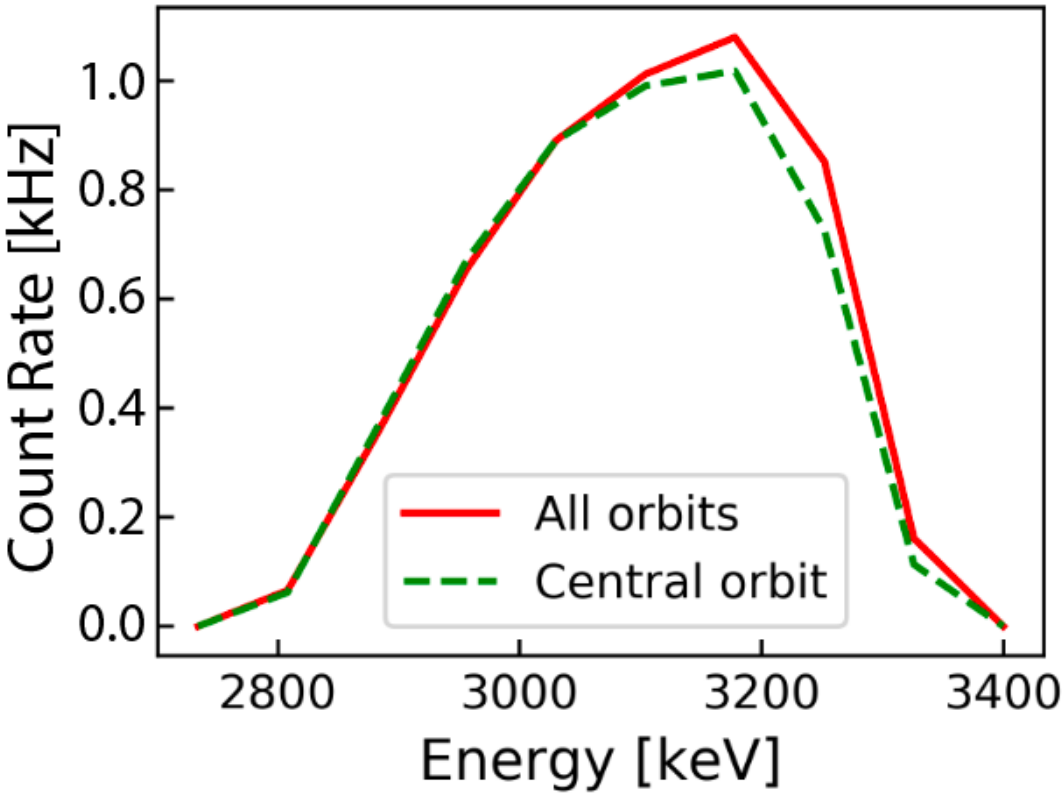

Figure 2.8: Comparison of the proton energy spectrum calculated using the true energy-dependent orbits and transmission factors (solid curve) with a calculation that employs identical orbits and transmission factors for all escaping proton energies (dashed).

To benchmark the code, the calculated count rate was compared with an independent calculation using the formalism described in [50] for the inputs of MAST discharge #29908. The calculations differ by 2-5% for different channels.

As a second verification exercise, the proton spectrum was calculated for a monoenergetic, isotropic distribution function with cold thermal deuterons. This is a condition for which an analytical prediction of the expected spectrum is available [61]. The calculated spectrum has the predicted shape (Fig. 2.9).

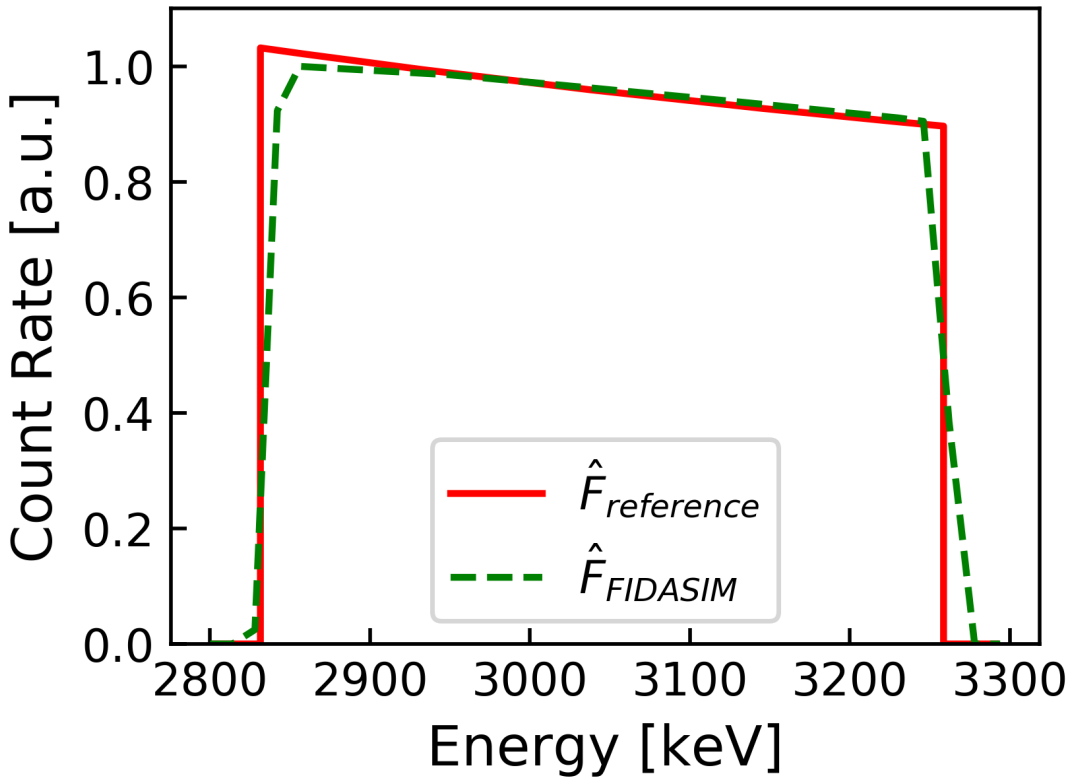

Figure 2.9: Proton energy spectrum for a monoenergetic (30 keV), isotropic, fast-ion distribution function in a plasma with nearly stationary deuterium target ions as computed by analytical theory (solid) and by FIDASIM (dashed).

2.7 Weight functions

The algorithm and program described so far computes the proton spectrum,

$$C(E_{p,1} < E_3 < E_{p,2}) \simeq A \int \int dl\, d\Omega\, T(\Omega) R p_{gyro} F(v_\parallel, v_\perp)\, dv_\parallel\, dv_\perp. \tag{2.20}$$

If we choose to evaluate the protons that come from a single position along the proton "sightline," (i.e., eliminate the integral over the sightline $\int dl$), Eq. 2.20 can be written as a set of factors that multiply the guiding-center fast-ion distribution function F. These factors

constitute the velocity-space weight function w_{2D},

$$w_{2D}(E_3, v_\parallel, v_\perp, \mathbf{r}) = A \int d\Omega T(\Omega) R p_{gyro}. \tag{2.21}$$

Note that, although F is written as a function of $v_\parallel$ and $v_\perp$, it is straightforward to reexpress the velocities in terms of fast-ion energy E_1 and pitch $(v_\parallel/v)$ if one prefers. In addition to its dependence upon fast-ion velocity, w_{2D} depends upon spatial position along the line of sight.

For forward modeling with a specified guiding-center distribution function $F(v_\parallel, v_\perp, \mathbf{r})$, the expected signal is

$$C(E_{p,1} < E_3 < E_{p,2}) = \int dl \int\int dv_\parallel \, dv_\perp w_{2D} F. \tag{2.22}$$

The derived expression can also be used to find three-dimensional weight functions for orbit tomography [39] by appropriately weighting w_{2D} spatially based on the properties of the selected fast-ion orbits.

As an example, Fig. 2.10 shows velocity-space weight functions for a MAST detector. In this example, contributions to w_{2D} have been summed over the orbit to eliminate the spatial dependence of the weight function. The selected channel is the one with the largest toroidal velocity component in Fig. 2.1. Owing to the Doppler shift associated with the $\cos\theta$ term in Eq. 3.2, fast ions that move away from the detector emit protons of reduced energy, while fast ions that head toward the detector emit protons of increased energy. This is the reason that deuterons that travel in the direction of the toroidal field are more likely to produce a low-energy proton than deuterons that circulate against $\mathbf{B}$ in Fig. 2.10a. Conversely, high-energy protons are produced most effectively by deuterons that travel opposite to the toroidal field (Fig. 2.10c). Near the unshifted energy of 3.03 MeV, owing to the gyromotion,

two peaks appear in the weight function (Fig. 2.10b). This occurs because one phase of the gyromotion can cancel the parallel component of motion along **B**, while another phase cancels the opposite parallel motion. The shapes of these three proton-energy-resolved weight functions are qualitatively similar to the FIDA weight functions of [38] and are caused by geometrical effects associated with the gyromotion. If one integrates over energy, the pitch dependence of the weight function essentially disappears (Fig. 2.10d). However, owing to the strong energy dependence of the d-d fusion cross section, all proton energies exhibit a strong dependence on deuteron energy. (When integrated over proton energy and fast-ion pitch, the energy dependence of the weight function is close to the energy dependence of the d-d reactivity σv.) The proton signal is produced primarily by the highest energy ions in the deuterium distribution function.

Although resolving the 3-MeV proton energy spectrum can be challenging, it has been successfully measured previously (e.g., [62]). (The spectra were poorly resolved in MAST but noise-reduction efforts are underway for MAST-U.) Figure 2.10 demonstrates that energy-resolved measurements provide valuable information about the deuterium distribution function.

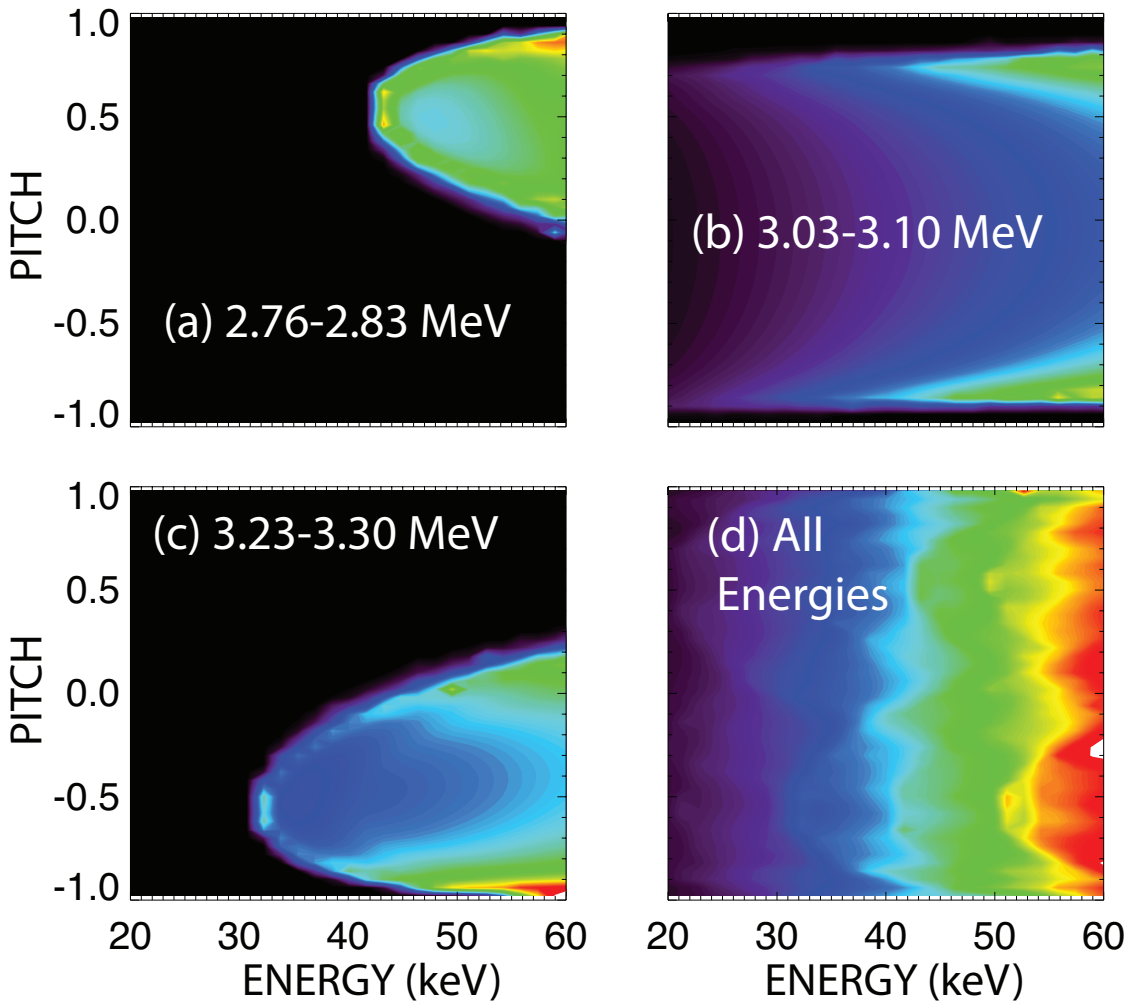

Figure 2.10: Velocity-space weight functions of a MAST 3-MeV proton channel for (a) down-shifted d-d protons, (b) unshifted protons, (c) up-shifted protons, and (d) protons of all energies. The abscissa is the fast-ion energy and the ordinate is $v_{\|}/v$ relative to the magnetic field. (Note that, since the plasma current is opposite to the toroidal field in this example, the sign of the pitch is reversed if pitch is defined relative to plasma current, as in TRANSP.) The same linear rainbow color table is employed in panels (a)-(c); in panel (d), the maximum value of the color table is 3.0 times larger.

2.8 Conclusion

An algorithm and computer program that calculates the count rate and weight function of a 3-MeV proton diagnostic has been developed and tested. The algorithm properly treats effects associated with curved proton orbits, as well as the anisotropy of the d-d cross section. The algorithm and program assumes that the proton signal is produced by beam-plasma reactions, rendering it inapplicable to plasmas with significant beam-beam or thermonuclear reaction rates.

In future work, the 3-MeV proton weight function will be employed in tomographic reconstructions of the fast-ion distribution function in MAST-U plasmas with proton, FIDA, neutron collimator, and neutral particle data.

Chapter 3

Conceptual Design of Spin Polarized Fusion Experiments on DIII-D

3.1 Introduction

The D-T cross-section in magnetically confined fusion plasmas is increased by 50 % when the spins of both nuclei are polarized in the same direction as the local magnetic field [63, 64]. Since the increased reactivity increases alpha heating, the increase in fusion Q is even greater than 50 % without any additional requirement on plasma confinement [65]. Spin-polarized fuel could relax the field and confinement requirements for a fusion reactor.

The retention of spin polarization in the plasma for periods comparable to the burn-up time is imperative to the success of spin polarized fusion. Theoretically [63, 66], depolarization mechanisms from field inhomogeneities or collisions are weak in the core of a tokamak but the polarization lifetime has never been measured. Experiments on a mid-size fusion facility like DIII-D can assess depolarization by inhomogeneous static magnetic fields, plasma waves, and Coulomb collisions in realistic reactor-relevant conditions.

Handling tritium in a research tokamak is hazardous and expensive. Fortunately, the isospin-mirror reaction D $+^3$ He $\rightarrow \alpha$ (3.6 MeV) + p (14.7 MeV) has nearly identical nuclear and spin physics as the D-T reaction [63, 64] and can be used as a proxy.

In addition to modifying the total cross section σ, spin polarization makes the D-^{3}He fusion cross section anisotropic. The differential cross section is [67]

$$\frac{d\sigma}{d\Omega} = \frac{\sigma_0}{4\pi}\left\{1 - \frac{1}{2}P_D^V P_{3He} + \frac{1}{2}\left[3P_D^V P_{3He}\sin^2\theta + \frac{1}{2}P_D^T\left(1 - 3\cos^2\theta\right)\right]\right\} \tag{3.1}$$

where the polar pitch angle θ is the angle between the emitted charged fusion product (CFP) and the local magnetic field at birth. The polarization factors P_{3He}, P_D^V and P_D^T depend on the distribution of the nucleus. The sub-state population fractions in the presence of a magnetic field are N_i, where $i = +1, 0, -1$ and $i = +1/2, -1/2$ for spin–1 and spin-1/2 systems, respectively. The spin configurations are normalized such that $\sum_i N_i = 1$ for each system. The polarization factors in Equation 3.1 can then be expressed using the sublevels as follows: helium-3 polarization $P_{3He} = N_{+1/2} - N_{-1/2} \in [-1, +1]$, deuteron vector polarization $P_D^V = N_{+1} - N_{-1} \in [-1, +1]$, and deuteron tensor polarization $P_D^T = N_{+1} + N_{-1} - 2N_0 \in [-2, +1]$. In the absence of any polarization, the D-^{3}He reaction is isotropic, $d\sigma/d\Omega = \sigma_0/4\pi$.

The concept explored here is to measure unconfined fusion products from D-^{3}He reactions to infer changes in the differential cross section (Equation 3.1) as the polarization changes. Although the total reaction rate depends upon the degree of polarization, its dependence on plasma parameters such as ion temperature T_i is even stronger. Direct measurements of the reaction rate itself for detection of the degree of spin polarization would be a challenge. Instead, relative CFP measurements are preferred over absolute measurements since they are less sensitive to uncertainties in plasma parameters. Three properties of the escaping CFPs are potentially useful as monitors of the differential cross section: pitch, energy, and poloidal distribution. Scintillator based fast-ion loss detectors (FILD) provide accurate relative mea-

surements of the flux vs. pitch $v_\parallel/v$ of escaping CFPs [68]. Pulse-counting silicon detectors can accurately measure the energy distribution of escaping 14.7 MeV protons [69]. An array of detectors that measure the escaping CFP flux at different poloidal positions [70] is also sensitive to the CFP $v_\parallel/v$ at birth. Because most D-^{3}He reaction products are unconfined in DIII-D, all of these techniques are potentially useful as diagnostics of reaction anisotropy.

The energy of a CFP produced by a beam with velocity $\mathbf{v}_1$ interacting with a target ion with velocity $\mathbf{v}_2$ is [55]

$$E_3 = \frac{m_4}{m_3+m_4}(Q+K) + V\cos\theta\sqrt{\frac{2m_3m_4}{m_3+m_4}(Q+K)} + \frac{1}{2}m_3V^2, \tag{3.2}$$

where Q is the fusion energy, $K = \frac{1}{2}m_1m_2|\mathbf{v}_1-\mathbf{v}_2|^2/(m_1+m_2)$ is the relative kinetic energy, $\mathbf{V} = (m_1\mathbf{v}_1+m_2\mathbf{v}_2)/(m_1+m_2)$ is the center-of-mass velocity, and θ is the angle between $\mathbf{V}$ and the CFP velocity in the center-of-mass frame, $\mathbf{v}_3'$. The first term on the right-hand side (RHS) of Equation 3.2 is the nominal CFP energy, $m_4Q/(m_3+m_4) = 14.7$ MeV for protons and 3.6 MeV for alphas. The second term, which is usually much larger than the third term, is a kind of Doppler shift associated with motion of the center of mass toward or away from the detector; it determines the energy shift of the CFP from its nominal value. In this chapter, detection of both protons and alphas are considered.

Two scenarios are covered. In the first, polarized ^{3}He and D pellets are injected into a hot hydrogen plasma to produce thermonuclear reactions that utilize 14.7 MeV proton and 3.6-MeV alpha detection. In the second scenario, a tensor-polarized deuterium pellet is injected into an L-mode hydrogen background plasma that includes neutral beam injection (NBI) of unpolarized ^{3}He. The persistence of changes in CFP signals yields a lifetime measurement.

A paper related to the work in this chapter [71] considers many important issues with

minimal coverage here, including a historical overview of research on spin polarized fusion in tokamaks, details of the relevant nuclear physics, depolarization mechanisms, and benefits for a fusion reactor. The preparation and delivery of polarized fuel pellets is discussed in considerable detail. This companion work also presents a candidate scenario and detection scheme but those topics are treated more thoroughly here.

The present chapter is organized as follows. Section 3.2 presents the experimental scenarios. In section 3.3, maximal values of cross section and tensor polarization are used to assess ideal CFP signals at existing DIII-D ports in the thermonuclear and beam-plasma scenarios, respectively. Next, realistic signal levels using existing polarization technology are quantitatively evaluated (section 3.4). A discussion of additional complications and considerations follows in section 3.5. Conclusions appear in section 3.6. Appendices discuss the numerical methods used to calculate thermonuclear signals, the generalization of the 3 MeV proton weight algorithm (developed in chapter 2) to calculate CFP signals from any general beam-target reaction, and an alternative method to calculate the accuracy of the measurements.

3.2 Thermonuclear and Beam-Plasma Scenarios

The D-^{3}He cross section σ is an extremely strong function of the relative energy of the reactants: it increases seven orders of magnitude between relative energies of 10 and 100 keV. As a result, to obtain an adequate count rate in CFP detectors, reactants with energies several times 10 keV are required. One way to obtain an adequate reaction rate R_{d3He} is to inject neutral beams with $O(100)$ keV energies and utilize beam-plasma reactions. Alternatively, thermonuclear reactions could be employed but the plasma must have ion temperatures $T_i \gtrsim 10$ keV for useful reaction rates. (The reactivity $\langle \sigma v \rangle$ is 33 times larger at $T_i = 10$ keV than at 5 keV.)

The strong dependence of σ on relative energy has several implications. One implication is that direct measurements of the reaction rates to detect changes associated with spin polarization requires plasmas of extraordinary reproducibility, since a 10% change in T_i between 9 and 10 keV changes R_{d3He} by more than 50%, which is more than the maximum possible change associated with polarization. Owing to this strong sensitivity, typical uncertainties in the measured T_i and the deuterium and ^{3}He densities could easily exceed the expected change in signal. To circumvent this difficulty, the relative measurements described here do not depend upon the absolute value of R_{d3He}

Another implication concerns the center-of-mass velocity $\mathbf{V}$. For a beam-plasma scenario, since $v_1 \gg v_2$, the center-of-mass velocity is determined primarily by the beam velocity, $\mathbf{V} \simeq m_1\mathbf{v}_1/(m_1+m_2)$. For 80 keV ^{3}He beam ions, Equation 3.2 then implies a Doppler shift (in MeV) of

$$\Delta E_p \simeq V\sqrt{\frac{8}{5}m_N Q}\cos\theta \simeq 0.75\cos\theta. \tag{3.3}$$

Since this energy shift is large and the differential cross section depends upon θ, Equation 3.3 implies that energy-resolved CFP measurements may be a useful diagnostic of the degree of polarization in a beam-plasma scenario.

The situation is different for a thermonuclear scenario. The fusion reactivity is

$$\langle\sigma v\rangle \equiv \int\int f_1(\mathbf{v}_1)f_2(\mathbf{v}_2)\sigma(|\mathbf{v}_1-\mathbf{v}_2|)|\mathbf{v}_1-\mathbf{v}_2|\,d\mathbf{v}_1\,d\mathbf{v}_2, \tag{3.4}$$

where f_1 and f_2 are the distribution functions of the two reacting species. For thermonuclear d-^{3}He reactions, f_1 and f_2 are isotropic Maxwellian distributions with most probable speeds of $v_{th,d} = \sqrt{2T_i/m_d}$ for deuterium and $\sqrt{\frac{2}{3}}v_{th,d}$ for ^{3}He. Because the cross section is a strong function of relative energy, the most probable reactions are between relatively fast deuterium and ^{3}He ions going in (approximately) opposite directions. Analysis of the integrand of

Equation 3.4 shows that, at $T_i = 10$ keV, the average reacting deuteron has speed of $2.0v_{th,d}$, while the average reacting ^{3}He ion has a speed of $1.4v_{th,d}$, with an average component of velocity opposite to the deuterium direction of $-0.95v_{th,d}$. As a result, the average center-of-mass speed of reacting ions is only $0.71v_{th,d}$ and is on the order of the deuterium thermal velocity for nearly all reactions. Hence, energy-resolved measurements of the CFP doppler shift are not a useful diagnostic of the degree of spin polarization for thermonuclear reactions since the resulting energy spread is too small to be experimentally measured.

3.2.1 TRANSP scenarios

As explained above, a large value of T_i is essential for a thermonuclear scenario. Fortunately, an operational regime with central ion temperature $T_i(0) \gtrsim 20$ keV is obtainable in DIII-D. The regime exploits an internal transport barrier associated with strong $\mathbf{E} \times \mathbf{B}$ shear in plasmas with large toroidal rotation to achieve high ion temperature reproducibly [72]. Figure 3.1 shows two examples of existing DIII-D discharges with quite high central ion temperature. All existing discharges with $T_i(0) > 10$ keV employed deuterium neutral beam injection into a deuterium plasma and had large beam-plasma D-D neutron rates.

In this study, we assume that the polarized D and ^{3}He fuel is delivered in the form of cryogenic pellets. (Neutral beam injection of spin polarized nuclei would facilitate lifetime experiments but suitable sources are presently unavailable.) The use of spin polarized pellets precludes the use of unpolarized deuterium beam injection to create the plasma scenario, because deuterium beams would create a large beam-plasma D-^{3}He reaction rate that would be an unwanted background for thermonuclear reactions between polarized fuel. Accordingly, we envision using hydrogen beams to create the high T_i scenario in a hydrogen (or ^{4}He) background plasma. Once the high T_i condition is established, polarized deuterium and ^{3}He pellets are injected. The resulting plasma likely will have lower values of $T_i(0)$ than existing

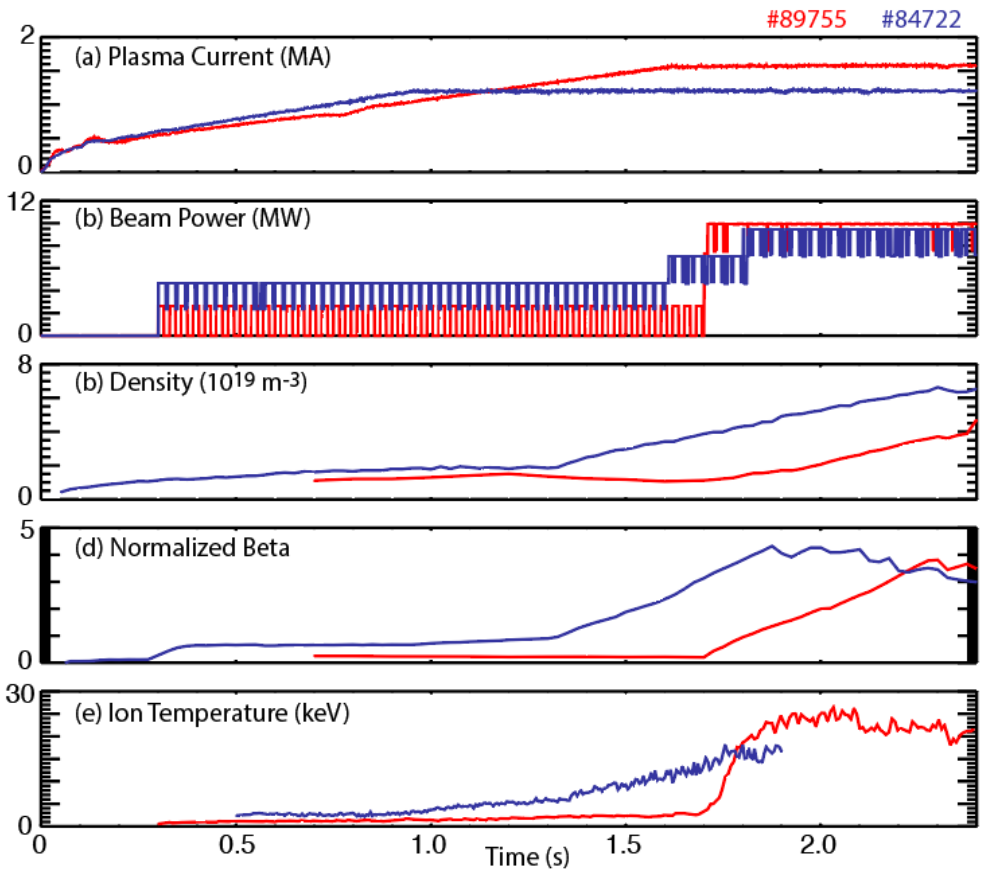

Figure 3.1: (a) Plasma current I_p, (b) injected deuterium beam power P_{inj}, (c) line-average density $\bar{n}_e$, (d) normalized beta β_N, and (e) central ion temperature $T_i(0)$ for two existing DIII-D discharges with T_i far in excess of 10 keV.

shots for three reasons. First, confinement is usually poorer in hydrogen plasmas than in deuterium plasmas [73]; also, less injected beam power and torque will be available. Second, even if the stored energy remains constant, pellet injection will lower the ion temperature by raising the density. Third, reductions in the plasma volume and the re-orientation of some of the beams from on-axis to off-axis may limit access to the previous conditions.

Despite these complications, a hydrogen beam heated scenario with minority populations of polarized deuterium and ^{3}He fuel and $T_i(0) \simeq 10$ keV appears obtainable. Starting with an existing TRANSP [60] run, the ion temperature and rotation were lowered, the neutral beams were changed to hydrogen, and the composition was altered to create a new TRANSP run with the profiles shown in Figure 3.2. The deuterium and ^{3}He densities are both assumed

to be 10% of the electron density. As expected, the D-^{3}He emissivity profile peaks strongly at the magnetic axis (Figure 3.2d). The equilbrium for the thermonuclear scenario has plasma current $I_p = 1.1$ MA, toroidal field $B_T = 2.1$ T, and a monotonically increasing q profile with $q(0) \simeq 1$.

Figure 3.2 also shows the selected profiles for a beam-plasma TRANSP scenario. In this case, the existing shot is a low-current ($I_p = 0.6$ MA), 2.0 T, L-mode discharge that was heated by a single deuterium beam that injected in the midplane in the co-current direction. The analyzed scenario replaces the deuterium beam within the TRANSP code with an unpolarized ^{3}He beam with the same power, voltage, and geometry. TRANSP properly modifies the beam deposition, orbits, and collisional slowing of the beam ions to obtain a realistic ^{3}He fast-ion distribution function. For the thermal plasma, we assume that a tensor-polarized deuterium pellet has been injected, so the thermal composition is switched to primarily hydrogen with a minority deuterium population, together with a small population of thermal ^{3}He fueled by the beam (Figure 3.2b). As in the thermonuclear case, the D-^{3}He emissivity profile peaks strongly at the magnetic axis (Figure 3.2d).

For both of these scenarios, the toroidal field is clockwise when viewed from above, so the curvature and ∇B drifts for ions are downward. Accordingly, we consider detectors that are located at poloidal angles that are in the lower half of DIII-D. If the toroidal field is reversed, suitable ports are in the upper half of the tokamak.

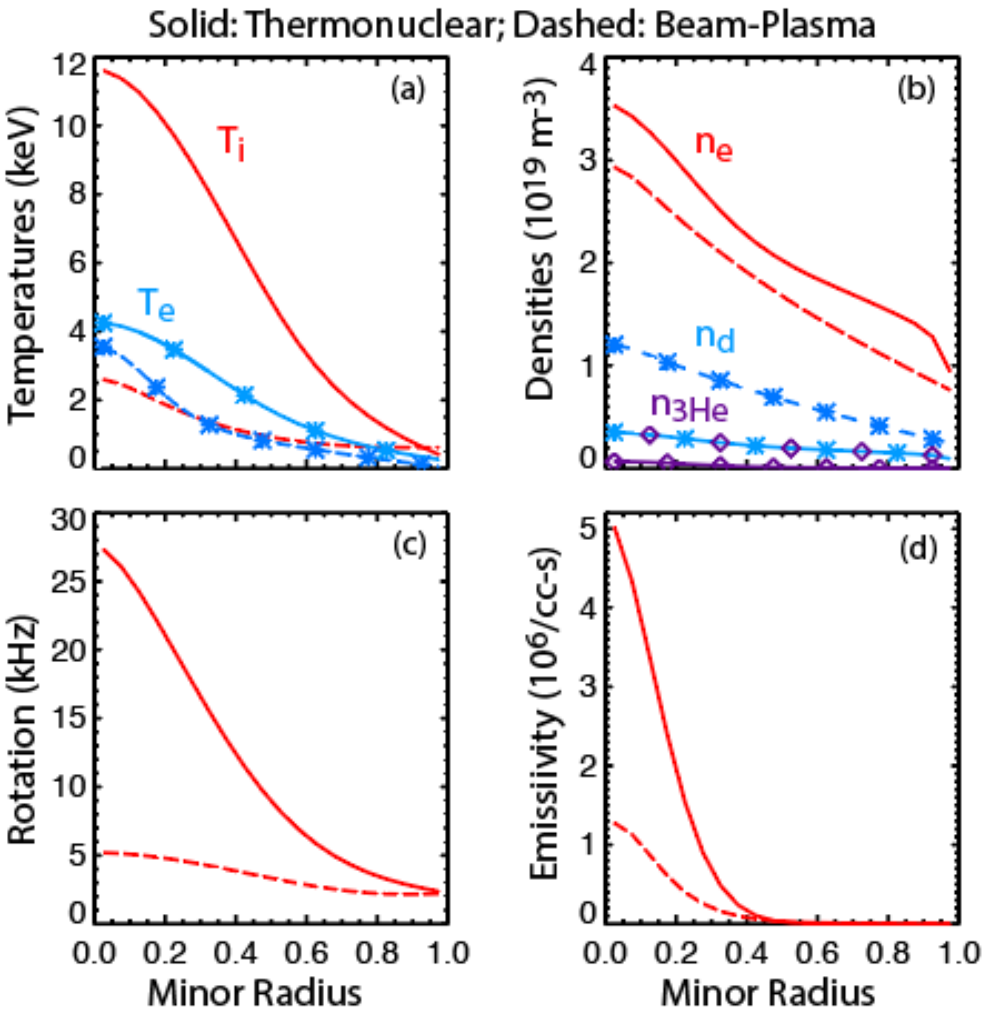

Figure 3.2: Assumed plasma profiles for the thermonuclear (solid lines) and beam-target (dashed) scenarios. (a) Ion (no symbol) and electron (symbols) temperatures; (b) Electron (no symbol), thermal deuterium (*), and thermal ^{3}He (diamond) densities; (c) toroidal rotation; (d) D-^{3}He emissivity. The abscissa is the square root of the normalized toroidal flux ρ.

3.3 Ideal Charged Fusion Product Signals

In this section, the maximum possible effect of spin polarized fuel on CFP signals is computed for the two scenarios described in the previous section. Realistic aspects of the calculations are: the scenarios are plausible discharge conditions obtainable in DIII-D and the calculations utilize existing vacuum ports. However, the calculations do neglect other practical considerations such as detector count rates and limitations in achievable pellet polarizations. These effects are considered in section 3.4. Nevertheless, these idealized calculations have the advantage of clearly identifying the most promising detection strategies.

3.3.1 Method

A naive, "brute force," approach to calculating CFP signals is to launch ions from their birth locations and record their positions and velocities when they strike the wall; however, because detectors typically occupy a small volume in phase space, this method is computationally inefficient and noisy. A far more elegant and efficient approach is to follow orbits backward in time from the detector. Since the slowing down time of charged fusion products is four-to-five orders of magnitude longer than typical orbit times, escaping CFP orbits are collisionless and reversible in time. Further, phase space is conserved along the orbit. Detected orbits are effectively detector sightlines, albeit curved ones that depend upon particle energy, pitch, and the equilibrium fields. Liouville's theorem implies that the detector count rate is [74]

$$C(E_3) = \iiint dl\, dA\, d\Omega\, S(\mathbf{r}, \mathbf{v}_3). \tag{3.5}$$

This method is widely employed in the magnetic fusion community and its validity is well established. For example, in a set of beautiful experiments on TFTR, Zweben et al. compared the pitch [68] and poloidal [70] distributions of promptly lost CFPs with theoretical

predictions.

For simplicity, throughout this section, in all plotted figures, the detected orbits are assumed to have the same detector area A and effective solid angle $\Delta\Omega$ so that the count rate is simply proportional to the integral of the emissivity over the curved sightline trajectory, $C \propto \int Sdl$.

Polarized fuel alters the differential cross section (Equation 3.1). We envision experiments that compare signals from discharges with pellets that are unpolarized, oriented to increase the total cross section, and oriented to reduce the total cross section. We call these three pellet configurations "isotropic," "enhanced," and "suppressed." For the thermonuclear scenario that employs both deuterium and ^{3}He pellets, the differential cross sections for these three spin configurations are

$$\begin{aligned}
\frac{d\sigma_{iso}}{d\Omega} &= \frac{\sigma_0}{4\pi} && \left[P_D^V = P_{3He} = P_D^T = 0\right] \\
\frac{d\sigma_{enh}}{d\Omega} &= \frac{9\sigma_0}{16\pi}\sin^2\theta && \left[P_D^V = P_{3He} = P_D^T = 1\right] \\
\frac{d\sigma_{sup}}{d\Omega} &= \frac{\sigma_0}{16\pi}\left(1+3\cos^2\theta\right) && \left[P_D^T = P_{3He} = 1 = -P_D^V\right]
\end{aligned} \tag{3.6}$$

Here, the values in the right column show the selected polarizations employed in Equation 3.1.

For the beam-plasma scenario where only the deuterium pellet is polarized, the three differential cross sections are

$$\begin{aligned}
\frac{d\sigma_{iso}}{d\Omega} &= \frac{\sigma_0}{4\pi} && \left[P_D^V = P_{He} = P_D^T = 0\right] \\
\frac{d\sigma_{+}}{d\Omega} &= \frac{\sigma_0}{4\pi}\left(\frac{5}{4}-\frac{3}{4}\cos^2\theta\right) && \left[P_D^T = 1 \,\&\, P_{3He} = 0\right] \\
\frac{d\sigma_{-}}{d\Omega} &= \frac{\sigma_0}{4\pi}\left(\frac{1}{2}+\frac{3}{2}\cos^2\theta\right) && \left[P_D^T = -2 \,\&\, P_{3He} = 0\right]
\end{aligned} \tag{3.7}$$

In both scenarios, the differential cross section depends upon the value of θ, the angle between the magnetic field and the emitted fusion product velocity in the center-of-mass frame. This angle is closely related to the CFP pitch angle $\cos^{-1}(v_\parallel/v)$, the only difference being that

the pitch angle is normally evaluated in the lab frame. Here, we define the "pitch" as the ratio of the toroidal velocity to the total speed v_ϕ/v *at the detector.* In general, the value of pitch changes along the orbit, so the value of $\cos\theta$ in Equation 3.6 and Equation 3.7 is not identical to the detected pitch (a) because $v_\parallel/v$ changes along a guiding center orbit and (b) because θ is evaluated in the center-of-mass frame. Nevertheless, to leading approximation, the detected pitch is closely related to $\cos\theta$, so different pellet polarizations should cause differing pitch dependencies at the detector.

Figure 3.3 shows that this expectation is correct, especially for 14.7 MeV protons. This figure plots the integral of the emissivity over the detected orbit, $\int S\,dl$, as a function of detected pitch for the three different differential cross sections in Equation 3.6. Since most of the reactions take place near the magnetic axis (Figure 3.2d), it is the value of the pitch angle near the magnetic axis that determines the differential cross section. Nevertheless, comparison of the dashed and solid curves in Figure 3.3a shows, for 14.7 MeV protons, evaluation of $d\sigma/d\Omega$ using the detected pitch yields nearly the same result as using its actual value at the birth location. Examination of the detected proton orbits (Figure 3.3c) explains why this is the case. At this port, the detected orbit is simply a single Larmor orbit, so $v_\parallel$ hardly changes. (Detailed tracking of the pitch along the orbit shows that the actual change between detector and core is 0.10.) All three signals decrease as the detected pitch increases because the shrinking gyroradius samples farther from the magnetic axis, where the emissivity is smaller. For 14.7 MeV protons in this configuration, in addition to its dependence on the spatial emissivity profile, the detected pitch distribution is directly sensitive to changes in differential cross section.

The situation is more complicated for 3.6 MeV alpha detection. Since the alpha Larmor orbit size is half as large as for 14.7 MeV proton orbits, now the detected sightline samples a portion of the guiding center orbit (Figure 3.3c). Consequently, the pitch at the detector is no longer the same as the pitch near the magnetic axis, so the approximation that the

detected pitch is approximately $\cos\theta$ no longer holds. (Notice the difference between the dashed and solid lines in Figure 3.3b). Detailed tracking along the orbit shows that the pitch changes by 0.5 between the detector and the core for the orbit with initial pitch of 0.6. Another difference is that, at its peak, the predicted signal is much larger than for the 14.7 MeV orbit. This is because the orbital "sightline" is much longer near the magnetic axis than the 14.7 MeV orbit that makes a single pass through the central region (Figure 3.3c).

Similar calculations for the beam-plasma scenario reinforce these conclusions. Since the toroidal field of 2.0 T is similar to the 2.1 T thermonuclear scenario, detected 14.7 MeV protons execute a single Larmor orbit and the detected pitch is nearly identical to the pitch at the magnetic axis, as in the thermonuclear example. However, since the current of 0.6 MA is considerably lower than the 1.1 MA current of the thermonuclear case, the guiding-center orbits of detected 3.6 MeV alphas are more poorly confined, so the detected pitch is closer to the pitch at the magnetic axis than in the thermonuclear case.

In the following subsections, calculations such as those shown in Figure 3.3 appear for both 14.7 MeV protons and 3.6 MeV alpha orbits at poloidal angles of -100°, -77°, -56° and 0° for both the thermonuclear and the beam-plasma scenario. Also, additional complications for the calculations in the beam-plasma scenario are considered.

3.3.2 Thermonuclear Scenario

Several simplifications are permissible for calculations in the thermonuclear scenario. First, since the center-of-mass velocity $\mathbf{V}$ is small, no distinction between the center-of-mass frame and the laboratory frame in the calculation of the differential cross section is required. Second, also because $\mathbf{V}$ is small, the Doppler shift in Equation 3.2 is modest and only modify orbital velocities by $\lesssim$1%, so only CFPs at the nominal birth energy need be considered. The calculated values of $\int S\,dl$ for the three different differential cross sections (Equation 3.6)

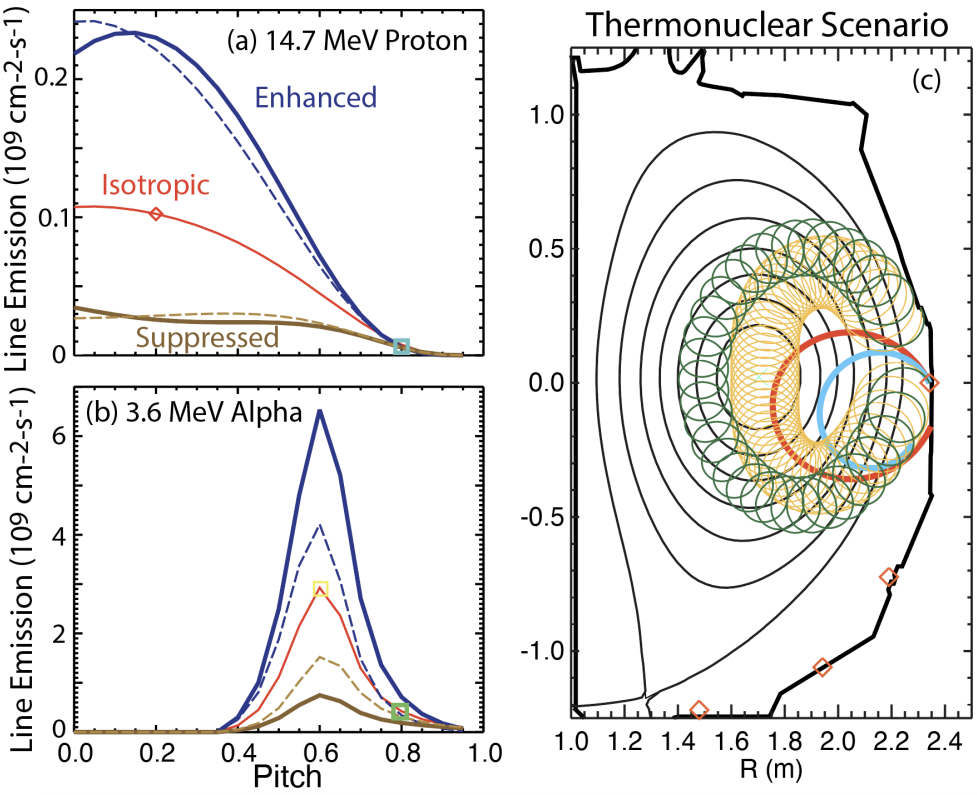

Figure 3.3: $\int S\,dl$ vs. pitch v_ϕ/v at the detector for (a) 14.7 MeV protons and (b) 3.6 MeV alphas measured at the midplane port for enhanced, isotropic, and suppressed differential cross sections (solid lines) in the thermonuclear scenario. The dashed curves are the variation that would occur if the pitch stayed constant on its orbit. The symbols indicate the values of pitch for the four orbits plotted on the right. (c) Elevation of DIII-D. The thin black curves are flux surfaces; the thick black curve represents the vacuum vessel wall. The overlaid nearly circular orbits are 14.7 MeV proton orbits with values of pitch of 0.2 (red) and 0.8 (cyan); the 3.6 MeV alpha orbits have pitch of 0.6 (yellow) and 0.8 (green). The diamond symbols indicate the locations of the four ports examined in this study.

for four different DIII-D ports appear in Figure 3.4a-d and Figure 3.5a-d for protons and alphas, respectively.

As discussed previously, owing to large anticipated variability in the total reaction rate, an actual experiment will rely primarily on relative measurements to assess the degree of nuclear polarization. Consequently, the most promising detection geometries are ones where the shapes of the curves vs. pitch (or port location) differ for the enhanced, isotropic, and suppressed cases. In Figure 3.4(e) and Figure 3.5(e), the pitch dependence of the enhanced

(solid lines) and suppressed (dashed lines) cases for each port are shown after normalization by the isotropic prediction. (The graphs plot $p_i\bar{u}/(u_i\bar{p})$, where p_i and u_i are the polarized and unpolarized signals at a particular pitch value and $\bar{p}$ and $\bar{u}$ are the average polarized and unpolarized signals for the entire array.) For proton detection, the large difference between the enhanced and suppressed cases for the $0°$, $-56°$, and $-77°$ ports (Figure 3.4e) indicates that measurement of the pitch dependence of the 14.7 MeV proton flux at any of these ports is a promising detection technique. In contrast, the similarity of the curves in Figure 3.5e indicates that pitch-resolved measurements of 3.6 MeV alphas at a single port are unlikely to provide useful information.

With an array of detectors, one could compare the ratio of the flux vs. poloidal angle. This is shown for protons and alphas in Figure 3.4f and Figure 3.5f, respectively. (Here, the signals for the different polarizations are normalized by the flux for that polarization at the $-56°$ port.) Here, the situation is reversed: since the enhanced and suppressed curves are similar for the proton case, a poloidal array of 14.7 MeV proton detectors is unlikely to provide useful polarization information. On the other hand, since the curves differ markedly, measurement of the 3.6 MeV alpha flux with three detectors situated at poloidal angles of $-100°$, $-77°$, and $-56°$ is a very promising detection technique.

Representative orbits for these two promising arrangements appear in Figure 3.6. For pitch-sensitive proton detection from the $-56°$ port (Figure 3.6a), detected orbit sightlines all transit close to the magnetic axis but, as in the example of Figure 3.3, the pitch at the magnetic axis is close to the detected pitch, ensuring strong sensitivity to the differential cross section. In contrast, for the poloidal array of 3.6 MeV alpha detectors, strong sensitivity is obtained by measuring different guiding center orbits that all pass through the magnetic axis with different values of pitch (Figure 3.6b). (The orbit detected at a poloidal angle of $-56°$ has little parallel velocity near the magnetic axis, while the orbit detected at $-100°$ has a larger value of $|v_\parallel/v|$.)

Numerical details about the calculation of $\int S\,dl$ appear in Appendix A.

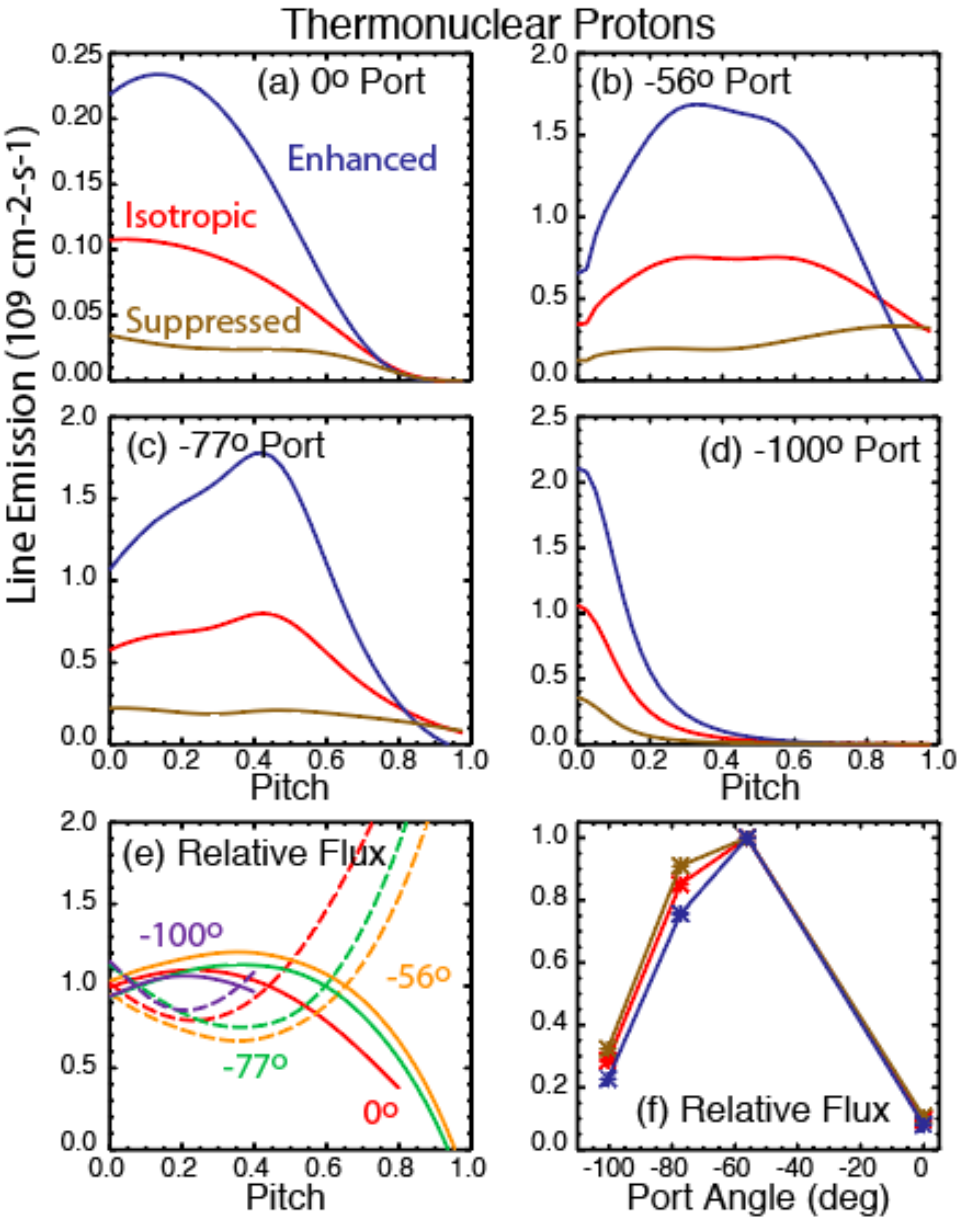

Figure 3.4: (a-d) $\int S\,dl$ vs. pitch for enhanced, isotropic, and suppressed differential cross sections for 14.7 MeV proton detection at four different ports for the thermonuclear scenario. (e) Dependence of the flux for the enhanced (solid) and suppressed (dashed) differential cross sections relative to the isotropic dependence for the same four ports. The curves have been normalized so that the total flux in both cases are equal. (f) Relative flux after integration over pitch vs. port location for the enhanced, isotropic, and suppressed differential cross sections.

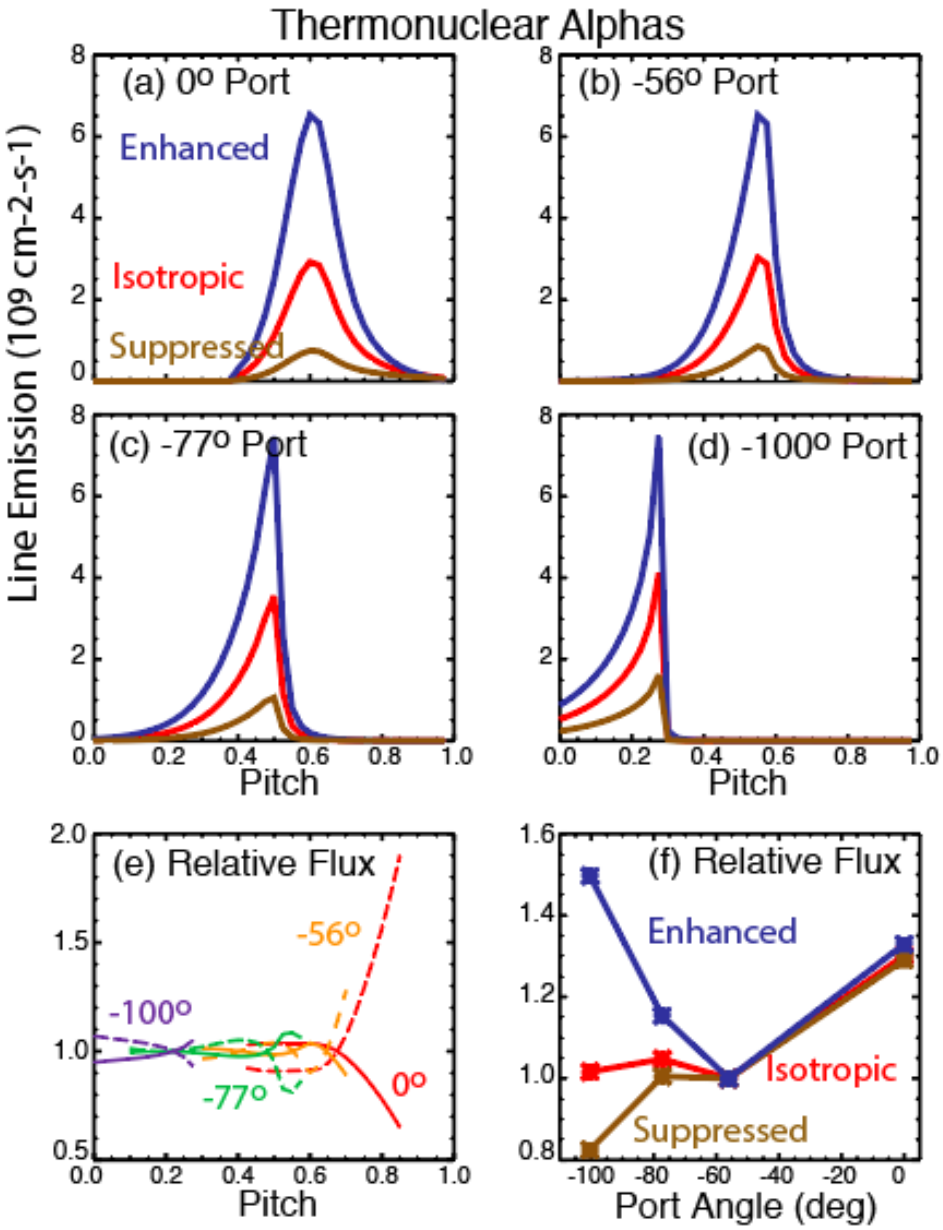

Figure 3.5: Same as Fig. 3.4 but for 3.6 MeV alphas.

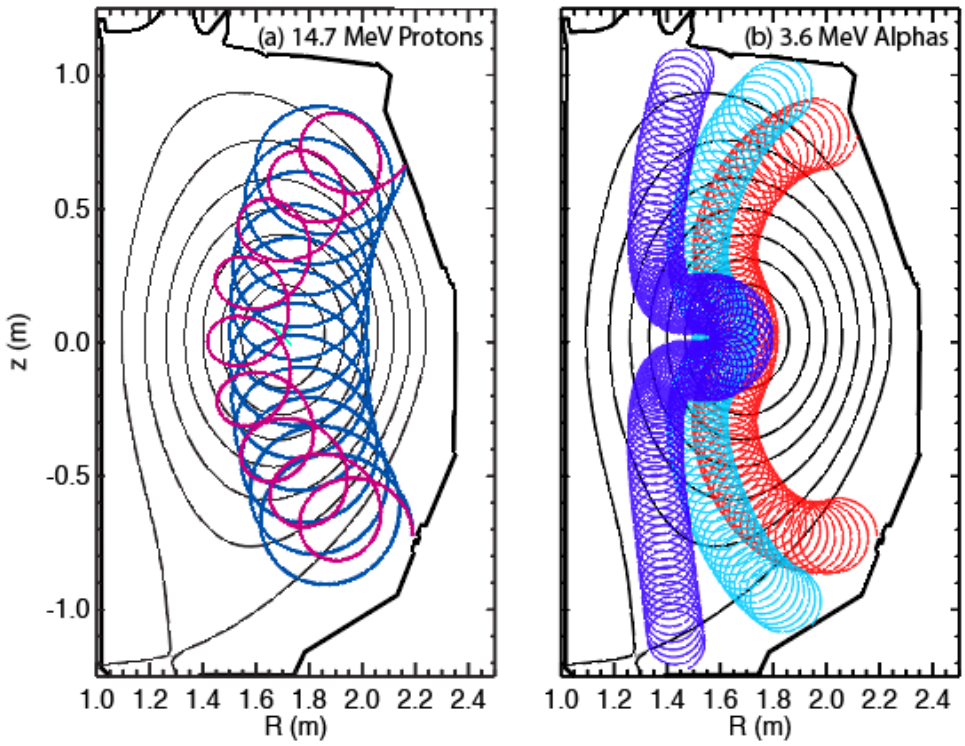

Figure 3.6: (a) Projection of a pair of 14.7 MeV proton orbits that are very sensitive to the differential cross section in the 1.1 MA thermonuclear equilibrium; these are the proton orbits with pitch of 0.4 and 0.8 in Figure 3.4b. (b) Projection of three 3.6 MeV alpha orbits whose ratio is very sensitive to the differential cross section; these are the alpha orbits with the largest values of $\int S\,dl$ in Figure 3.5b-d.

3.3.3 Beam-plasma Scenario

Calculations of CFP signals from beam-plasma reactions are more challenging. For beam-plasma reactions, the energy shift from the nominal value in Equation 3.2 can be appreciable. Chapter 2 shows that the emitted CFP energy depends on the velocities of the reactants and the direction of emission, so the "sightline" trajectory depends upon the reaction kinematics, with the consequence that different CFP energies probe different volumes in both velocity and configuration space.

Ideal energy resolved count rates are calculated in this section. We express the d–^{3}He reaction in standard nuclear physics notation 2(1,3)4, where particle 2 is the thermal deuterium, particle 1 is the ^{3}He beam, particle 3 is the detected CFP, and particle 4 is undetected. Our concern is with both products of the d(^{3}He,p)t reaction, i.e. the representation of particle 3 and 4 are interchangeable. Thus, $m_1 = 3m_p$, $m_2 = 2m_p$, $m_3 = m_p$ or $4m_p$ and $m_4 = 4m_p$ or m_p, respectively, where m_p is the proton mass. The measured energy-resolved count rate (Equation 3.5) is $C(E_3, \Delta E_{bin})$, where E_3 is the CFP energy and ΔE_{bin} is the energy resolution of the measurement.

Similar to the formulation for collimated neutron detection [42], Equation 3.5 and Equation 2.3 can be divided into two parts. One part describes the d–^{3}He reactivity for the selected reaction kinematics, and the second part describes the number of fast ions that can produce a CFP with the velocity v_3 accepted by the specified sightline,

$$S(\mathbf{v}_3, \mathbf{r}) = \int d\mathbf{v}_1 \int d\mathbf{v}_2 \, R(\mathbf{v}_1, \mathbf{v}_2, \mathbf{v}_3, \mathbf{r}) p_{gyro}(\mathbf{v}_1, \mathbf{v}_2, \mathbf{v}_3) f_1(\mathbf{v}_1, \mathbf{r}) f_2(\mathbf{v}_2, \mathbf{r}). \tag{3.8}$$

The emissivity R depends upon the D-^{3}He cross section (including anisotropy), the relative velocities of the reactants $|v_1 - v_2|$, and the emitted CFP's velocity v_3. Integration over the thermal distribution function f_2 is merged into the emissivity R, making R a function of the ion temperature T_i, the rotation velocity v_{rot}, and the deuterium target density n_d. The

velocity space factor $p_{gyro}(v_1, v_2, v_3)$ represents the probability density that the gyroangle of the fast ion has the correct value to produce the measured proton. Equation 2.11 An expression for p_{gyro} for detection of 3-MeV protons produced in D-D reactions appeared in chapter 2. The generalization of p_{gyro} for arbitrary reactant mass appears in Appendix B and supplementary details about the algorithm in FIDASIM are in Appendix C.

There are three relevant rest frames to consider. The CFP velocity v_3 is known in the lab frame. The effect of the target distribution function $f_2(v_2)$ on the reaction rate is most easily computed in the rotating plasma frame. Effects from anisotropy are computed in the center-of-mass frame. Refer back to chapter 2 for supplementary details.

Calculations are done within the FIDASIM framework [33, 34]. A new version of the CFP algorithm based on the work in chapter 2 is developed to calculate Equation 3.5 for diagnostics that measure CFPs produced from D-^{3}He fusion reactions between a ^{3}He beam ion distribution function and a thermal deuteron. Initial calculations of time-reversed CFP orbits compute effective solid angles and sightlines for the relevant range of incident proton or alpha velocity vectors. For each sightline, using the precomputed orbit as input, FIDASIM calculates the reactivity averaged over the thermal distribution of the 'target' deuterons from Bosch and Hale coefficients [11] and the probability p_{gyro} that a fast ion of specified energy and pitch has a gyroangle that is consistent with the kinematic equations. The code can be viewed online on the FIDASIM GitHub page [57], and documentation is found at [35].

Pitch spectra for the three polarization modes in Equation 3.7 for the previously mentioned DIII-D ports are shown in Figure 3.7a-d and Figure 3.8a-d for protons and alphas, respectively. The interpretation is similar to the thermonuclear case. Since large variations are observed between the $d\sigma_+/d\Omega$ and $d\sigma_-/d\Omega$ cases, Figure 3.7e suggests that measurement of the pitch dependence of the 14.7 MeV proton flux at any of the four ports is promising, whereas the similarity of the curves in Figure 3.8e shows that pitch-resolved measurements of 3.6 MeV alphas at a given port would not provide useful information.

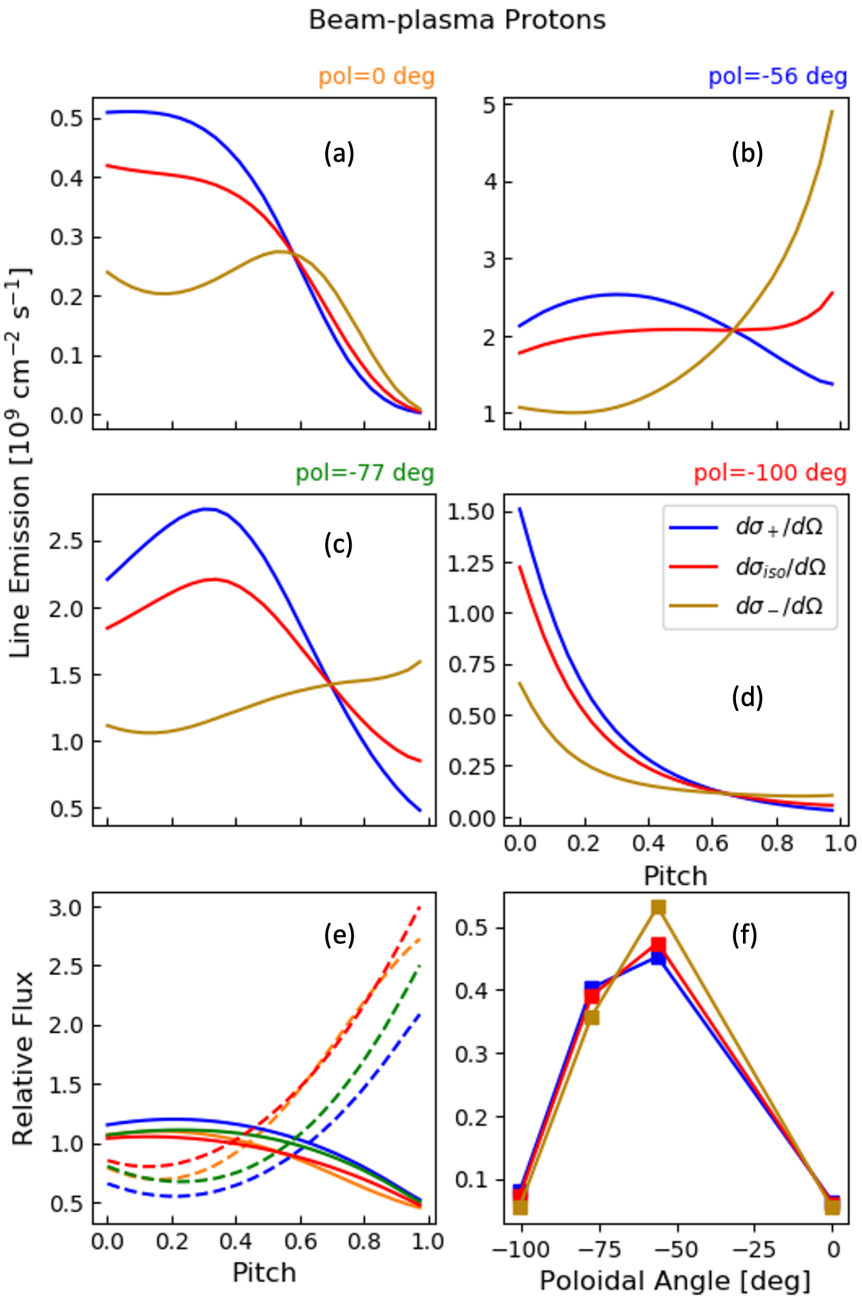

Figure 3.7: (a-d) Flux vs. pitch for the three differential cross sections of Equation 3.7 for 14.7 MeV proton detection at four different ports for the beam-plasma scenario. The signals are integrated over energy. Panels (e) and (f) are in the same format as Figure 3.4 e&f, where red, green, blue, and cyan are -100°, -77°, -56° and 0° in panel (e), respectively.

Comparisons of the ratio of the flux vs. poloidal angle appear in Figure 3.7f and Figure 3.8f for protons and alphas, respectively. Again, the takeaways are similar to the conclusions for the thermonuclear scenario. Proton detection shows little variation and alpha detection

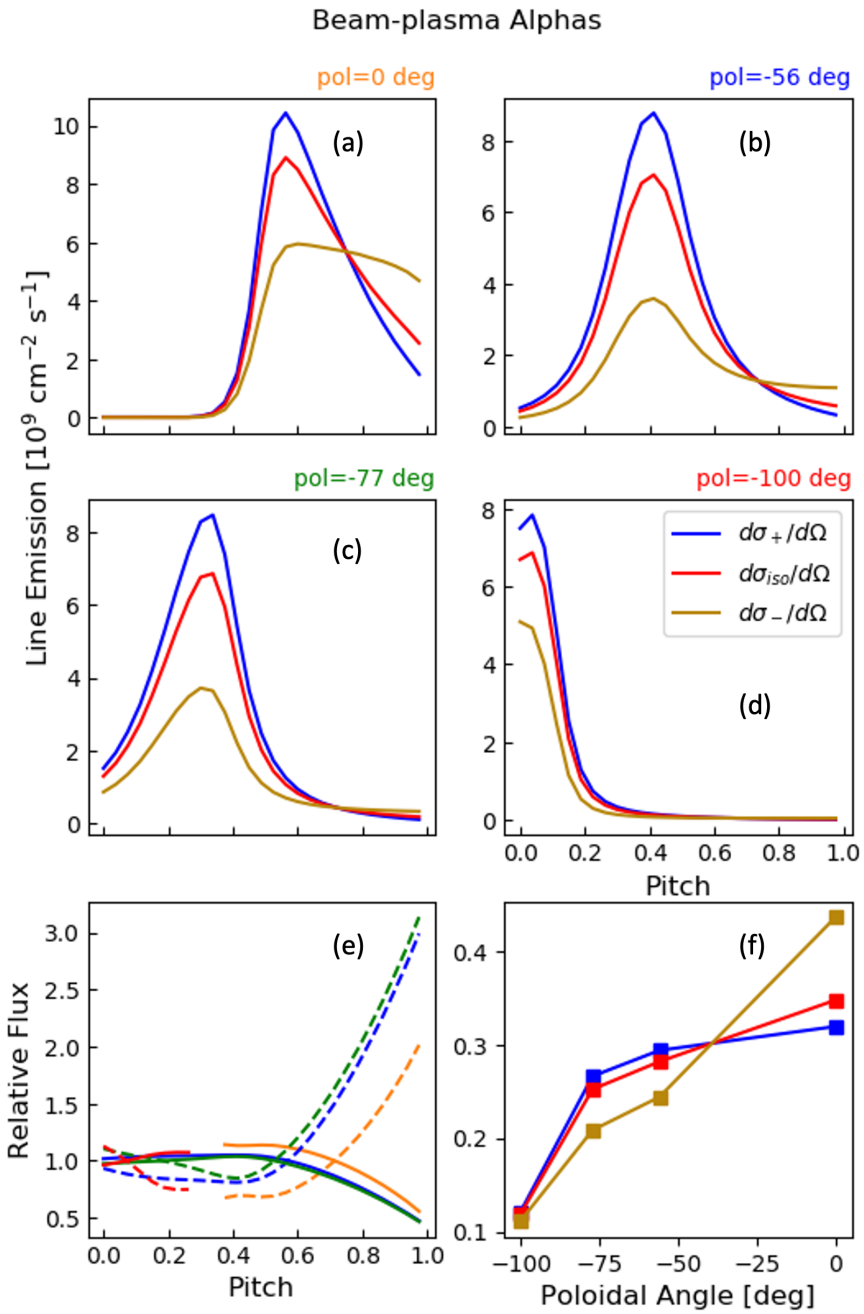

Figure 3.8: Same as Figure 3.7 but for alphas.

shows large variations between the $d\sigma_+/d\Omega$ and $d\sigma_-/d\Omega$ cases. A poloidal array of detectors measuring 3.6 MeV alphas would provide useful information, whereas an array of 14.7 MeV proton detectors would not.

Energy resolved spectral signals for protons are shown in Figure 3.9 for the four ports.

Because the Doppler shift is proportional to $V \cos\theta$ (Equation 3.2), the CFP energy is sensitive to the dependence of the differential cross section $d\sigma/d\Omega$ on the emitted pitch θ. Consequently, to a large extent, the energy dependence resembles the pitch dependence. For example, large values of pitch have stronger signals for the $d\sigma_-/d\Omega$ case, while the $d\sigma_+/d\Omega$ case produces stronger signals for small pitch. As a result, when the predicted signals are integrated over pitch, as in Figure 3.10, low energies that are associated with large pitch have the strongest signals for the $d\sigma_-/d\Omega$ case but higher energies that are associated with small pitch have the largest signals for the $d\sigma_+/d\Omega$. In particular, the -56° port in Figure 3.10c shows the largest variation in energy.

In contrast, the alpha energy spectrum is insensitive to the type of polarization. This is expected, since most alphas measured at a particular port are emitted with nearly identical pitch (Figure 3.8).

The best proton and alpha orbits for the beam-plasma scenario are shown in Figure 3.11. Similar to the thermonuclear scenario, the -56° port (Figure 3.11a) is best for pitch-sensitive proton detection since sightlines pass near the magnetic axis. On the other hand, a poloidal array is best for 3.6 MeV alpha detection since each port samples a narrow range of orbits with the values of pitch that allow the sightline to pass near the magnetic axis (Figure 3.11b). This is encouraging since the beam-plasma signals utilize a lower-current (0.6 MA) equilibrium than the higher current (1.1 MA) thermonuclear scenario, implying that the choice of an attractive detector configuration is not strongly dependent upon the equilibrium. Using FIDASIM to calculate CFP signals, the conclusions of this section match the thermonuclear scenario, and additionally show that energy-resolved detection of 14.7 MeV protons is a possible detection technique. (Energy detection is even more favorable if the beam is higher energy and more tangential than the DIII-D beams.)

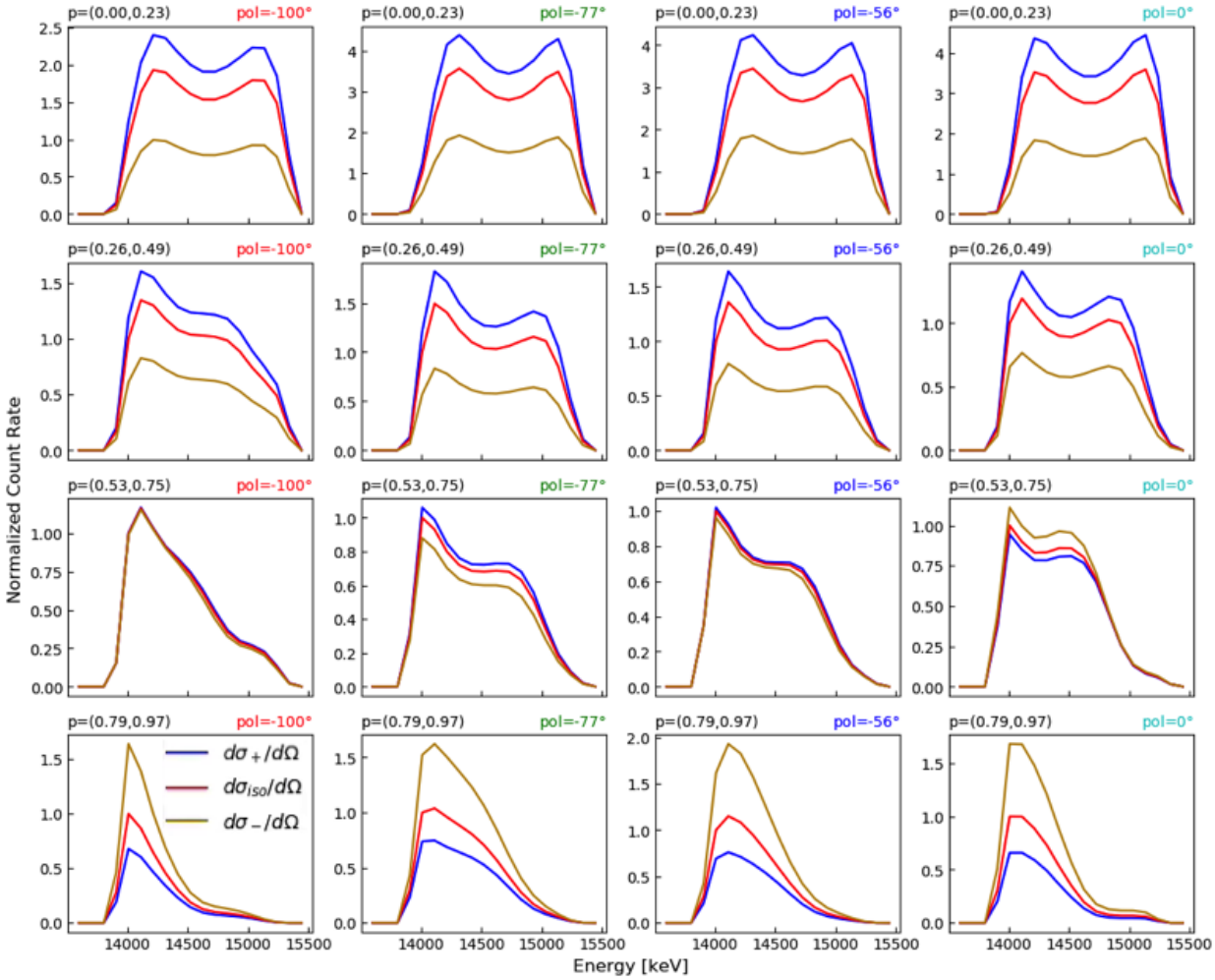

Figure 3.9: FIDASIM calculated energy distributions for 14.7 MeV proton detection in the beam-plasma scenario for the four ports. All three polarization cases are shown. Signals are integrated over successive intervals of pitch $\simeq 0.25$.

3.4 Accuracy estimates

The previous section showed several promising options for detection of the degree of polarization, including a pitch-resolving 14.7-MeV proton detector for both the thermonuclear and beam-plasma case, a poloidal array of 3.6-MeV alpha detectors for the thermonuclear case, and energy-resolved proton measurements for the beam-plasma case. But these calculations all assumed ideal detectors and polarizations. This section provides realistic, quantitative assessments of the feasibility of these detection techniques.

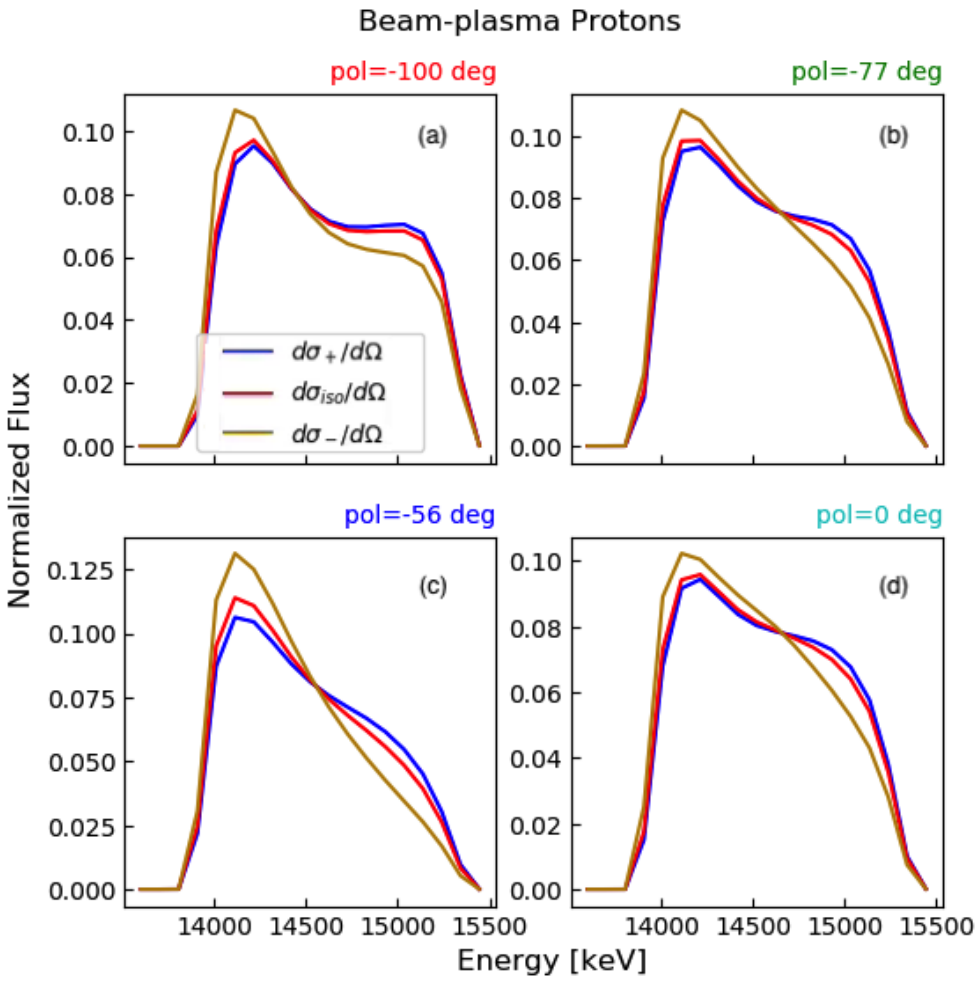

Figure 3.10: Beam-plasma proton spectra integrated over pitch for the four detector ports.

The first practical complication is that current technology cannot produce fuel pellets with 100% polarization. A reasonable value for vector polarization of ^{3}He is 0.65 [71]. For deuterium, one approach uses an H-D capsule and another approach uses a ^{7}Li-D capsule. The expected values for the H-D capsule are 0.4 for the vector polarization and 0.12 for the tensor polarization [71]. The ^{7}Li-D capsule can potentially deliver larger values of 0.70 and 0.41 for the vector and tensor polarizations, respectively. In the evaluations displayed in the following figures, we consider the more conservative H-D values for the thermonuclear case, i.e., $P_D^V P_{3He} = \pm 0.26$ and $P_D^T = 0.12$ in the expression for the differential cross section (Equation 3.1). For the beam-plasma assessment, we use the more optimistic value of $P_D^T = 0.41$ associated with the ^{7}Li-D pellet. (Significant $d\sigma_-/d\Omega$ tensor polarization varia-

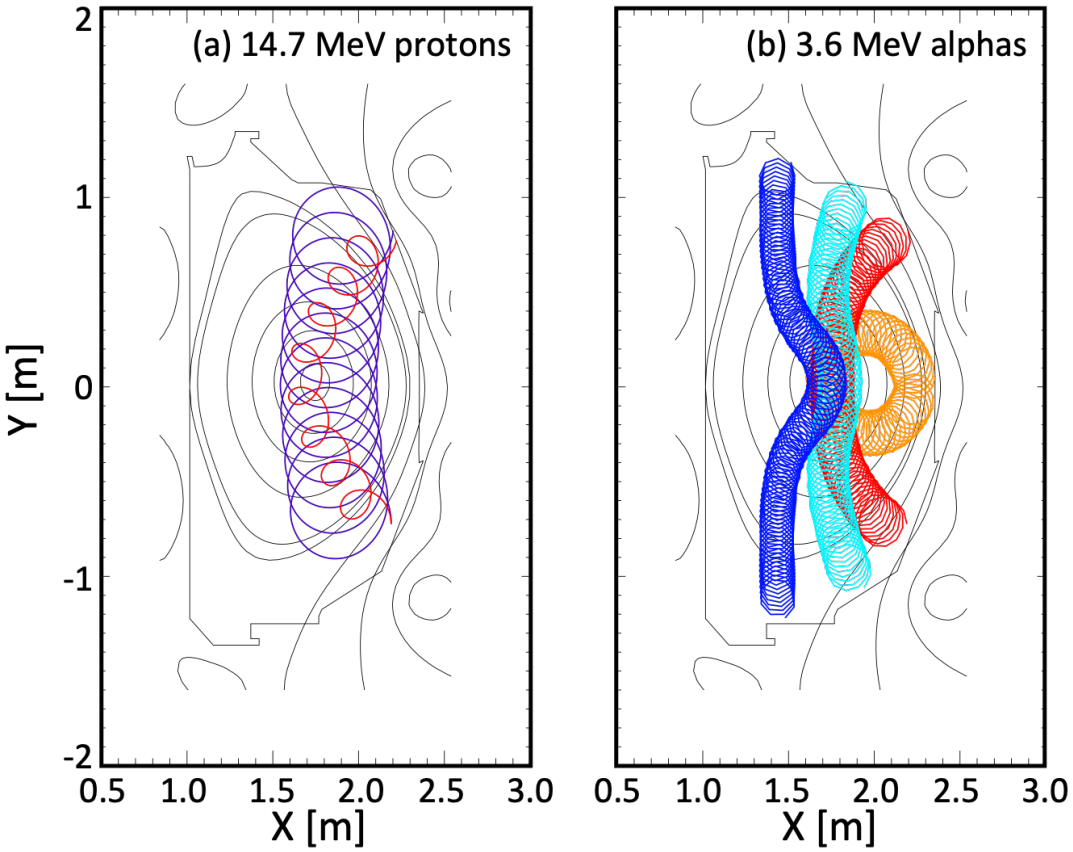

Figure 3.11: (a) Projection of two 14.7 MeV proton orbits with pitch of 0.2 and 0.9 in the beam-target equilibrium. (b) Projection of four 3.6 MeV alpha orbits. Pitch at the detector is different for all four ports and orbits pass near the magnetic axis.

tion is not presently available.) Although these are likely values using existing technology, new schemes discussed in [71] should be able to produce $P_D^V = 1$ and $P_D^T = 1$ and possibly even $P_D^T = -2$ but require extensive research and investment [71]. Figure 3.12(a,b) compares the normalized differential cross sections used in section 3.3 with the realistic cross sections used here.

A second practical complication is detector count rates. According to Equation 3.5, in addition to $\int S\, dl$, the count rate depends upon the area of the detector and its solid-angle resolution. To estimate these, we assume a fast-ion loss detector similar to one currently installed on DIII-D [75]. This detector has a rectangular 1-mm by 3-mm aperture that

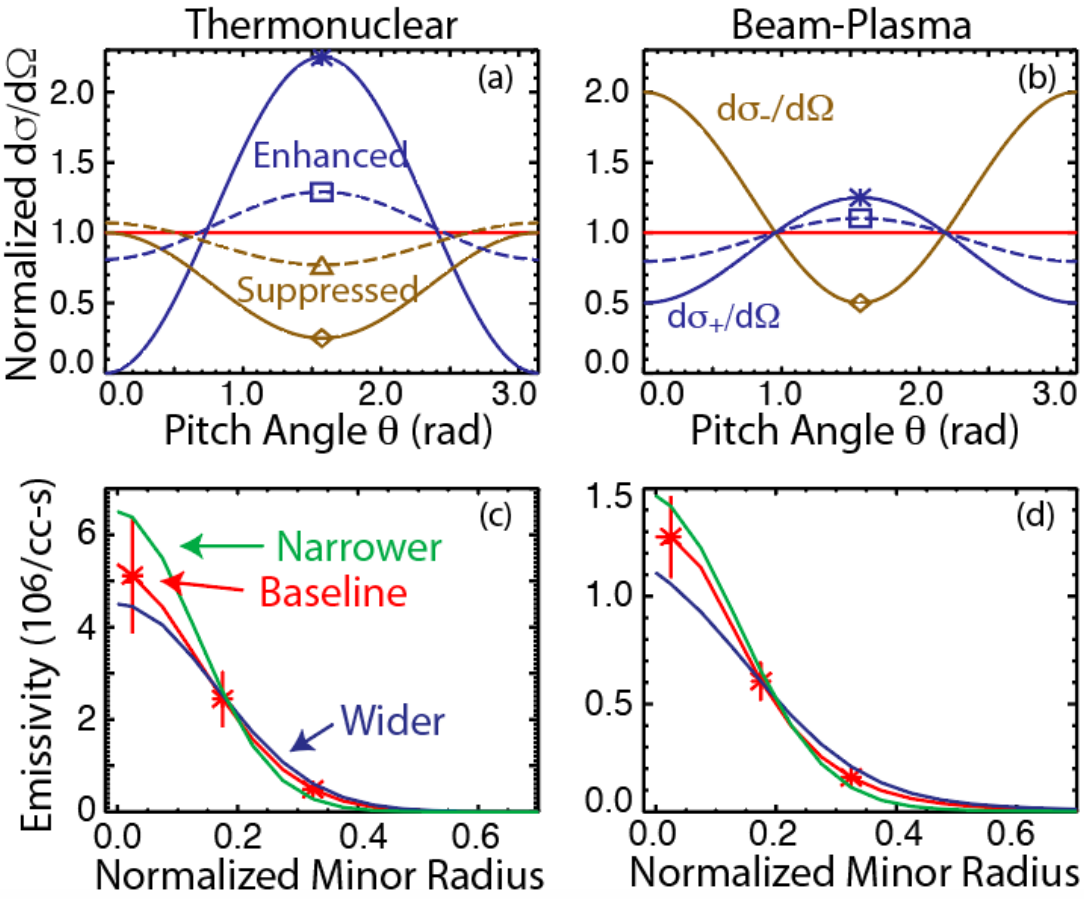

Figure 3.12: Comparison of the ideal differential cross sections (solid lines) used in section 3.3 with the realistic differential cross sections (dashed lines) employed in section 3.4 for the (a) thermonuclear and (b) beam-plasma cases. (c) Sensitivity of the thermonuclear D-^{3}He emissivity profile S to 5% uncertainty in T_i and 10% uncertainties in n_D and n_{3He}. The error bars show one-sigma uncertainties at selected locations. The solid curves show the baseline emissivity profile computed by TRANSP, together with wider and narrower profiles employed in Figure 3.13 and Figure 3.14 to test the sensitivity of the calculations to the emissivity profile. (d) Emissivity profiles employed in analysis of the realistic beam-plasma case.

provides $\sim 5^\circ$ resolution in pitch and $\sim 15^\circ$ resolution in gyroangle; for this geometry, the coefficient that multiples $\int S\,dl$ is approximately 3×10^{-5} cm^2. The number of counts also depends upon the desired temporal resolution, which depends upon the rate of decay of the polarization. Theoretically, the polarization state is expected to decay slowly [63], so we assume 50-ms time bins in our analysis.

A third practical complication is the sensitivity of predicted signals to the integrated emis-

sivity $\int S\,dl$. It was stressed in section 3.1 that relative measurements are less sensitive than absolute measurements to the large uncertainties in the overall reaction rate, but the same strong sensitivity also complicates interpretation of relative measurements. Figure 3.12(c) shows that reasonable estimates of the uncertainties in T_i, n_D, and n_{3He} substantially broaden or narrow the thermonuclear emissivity profile. Similarly, in the beam-plasma case, uncertainties in the fast-ion and deuterium density profiles can broaden or narrow the emissivity profile [Figure 3.12(d)]. In addition, the escaping orbits, which are the effective sightlines, depend upon the equilibrium reconstruction. To test the sensitivity to uncertainties in equilibrium reconstructions, an EFIT equilibrium [59] from a nearby time that differs from the baseline reconstruction by typical random error is selected, and the calculations of $\int S\,dl$ are repeated.

Figure 3.13 and Figure 3.14 show the results of calculations that employ these assumptions about pellet polarization, detection efficiency, and emissivity and equilibrium profiles for the thermonuclear scenario. The error bars shown on the figures are the one-sigma errors associated with counting statistics, the square root of the number of counts. One observation is that predicted signal levels are significant, in the range of 2×10^4 cps for pitch-resolved proton detection and 2×10^5 cps for alpha flux measurements. A second observation is that, as expected, the results are sensitive to the emissivity profile and equilibrium; however for a given assumed set of profiles, the difference between the curves for different polarization states is similar.

To assess quantitatively the accuracy of these candidate measurements, we consider the null hypothesis that the polarized data are consistent with unpolarized signals and compute the reduced chi-squared χ_r^2. If χ_r^2 is significantly greater than unity, the candidate measurement detects polarization with high confidence but, if $\chi_r^2 \lesssim 1$, the measurement is unable to reliably detect polarization. The procedure for calculating $\chi_r^2 \lesssim 1$ is well defined for random errors but proper assessment of systematic errors is more challenging. We have used two methods

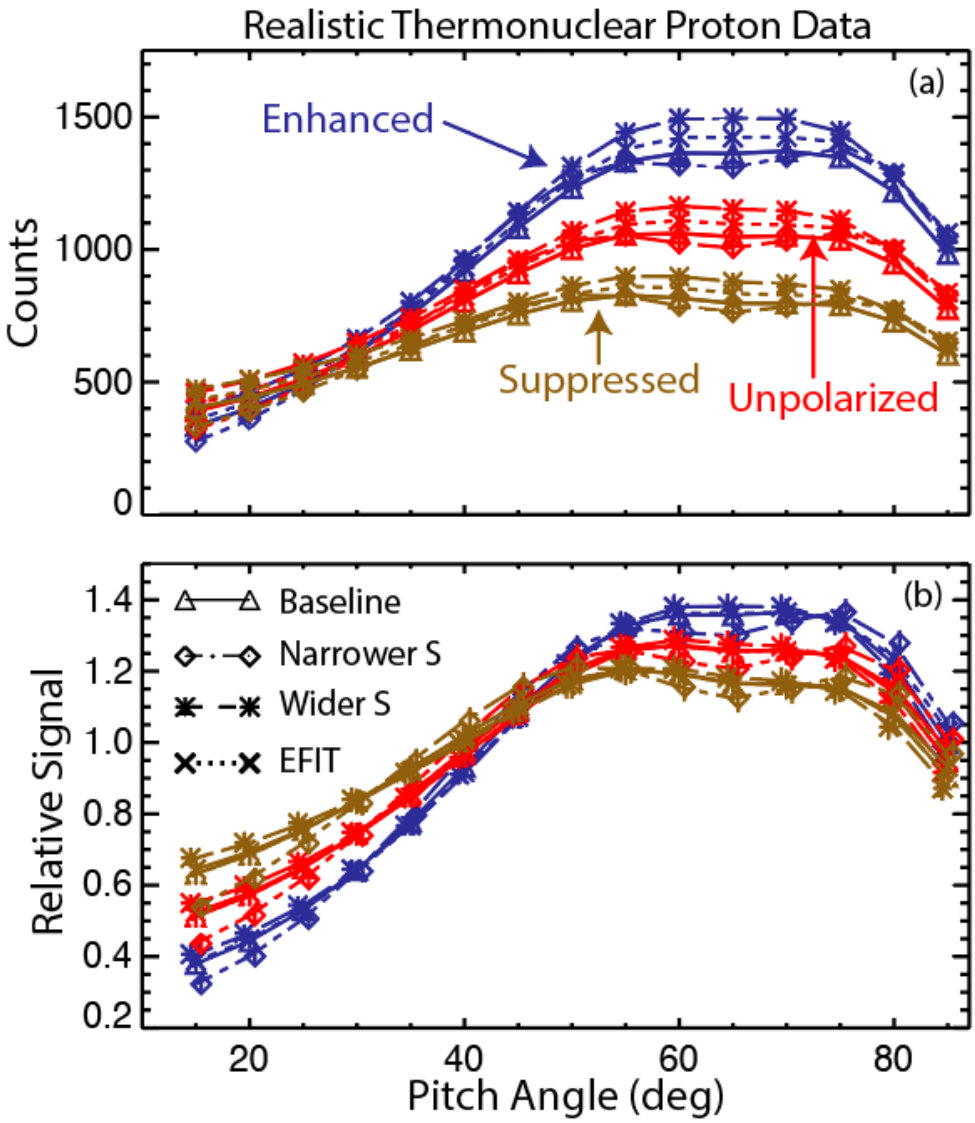

Figure 3.13: Realistic synthetic thermonuclear data for enhanced ($P_D^V P_{3He} = 0.26$, $P_D^T = 0.12$), unpolarized ($P_D^V P_{3He} = P_D^T = 0$), and suppressed ($P_D^V P_{3He} = -0.26$, $P_D^T = 0.12$) polarizations for a 14.7 MeV proton detector at the $-56°$ port. The calculations assume pitch angle resolution of 5°, gyroangle resolution of 15° and temporal resolution of 50 ms. Both (a) raw counts and (b) signals after normalization by the total detected flux (b) are shown. For each polarization case, the four curves represent calculations with the baseline emissivity profile and equilibrium (thick lines with triangles), the narrow emissivity profile of Figure 3.12(c) and baseline equilibrium (dash-dot lines with diamonds), the wide emissivity profile of Figure 3.12(c) and baseline equilibrium (dashed lines with *), and the baseline emissivity profile but different equilibrium reconstruction (dotted lines with X symbols). Note: Some error bars are smaller than the symbol size.

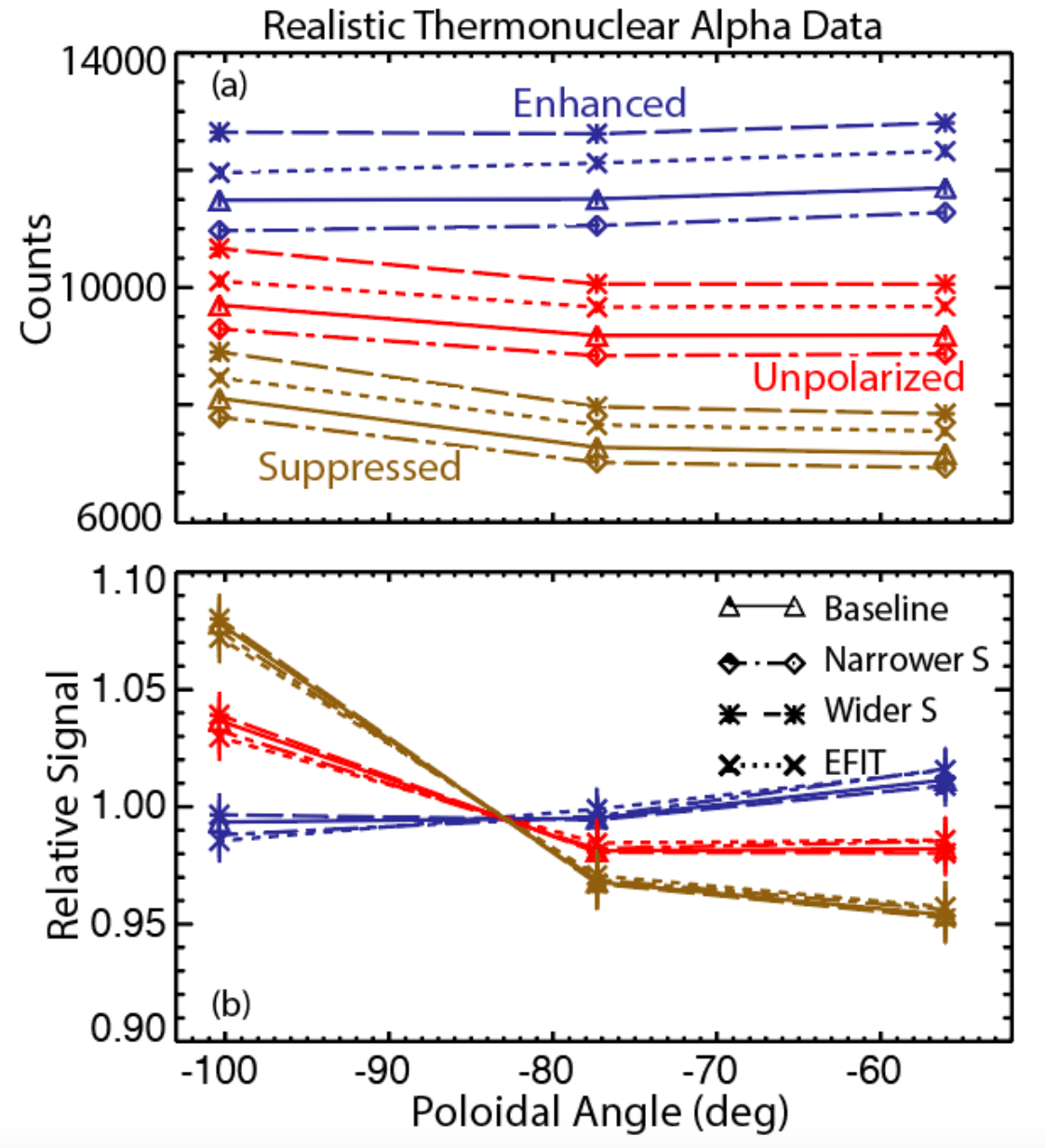

Figure 3.14: Realistic synthetic thermonuclear data for detection of the 3.6 MeV alpha flux with detectors at three different poloidal angles. The calculations assume 50-ms temporal resolution, 15° gyroangle resolution, and measurement of all significant escaping pitch angles. The figure format is the same as Figure 3.13.

that yield similar conclusions; the simpler but less rigorous treatment appears here, while a more rigorous and complicated method is documented in Appendix D. For application of the simpler method to the relative measurements in Figure 3.13b and Figure 3.14b, the

CFP	Polarization	χ_r^2 (H-D)	χ_r^2 (^{7}Li-D)
Proton	Enhanced thermonuclear	4.4	16.3
Proton	Suppressed thermonuclear	2.6	4.9
Alpha	Enhanced thermonuclear	5.8	19.4
Alpha	Suppressed thermonuclear	4.2	8.2
Proton	Tensor polarized beam-plasma	0.13	1.7
Alpha	Tensor polarized beam-plasma	0.08	0.9

Table 3.1: Estimates of χ_r^2 for synthetic data calculated using Equation 3.9. The third column assumes $P_D^V = 0.40$ and $P_D^T = 0.12$ and the fourth column assumes $P_D^V = 0.70$ and $P_D^T = 0.41$. Values much greater than unity indicate confident detection.

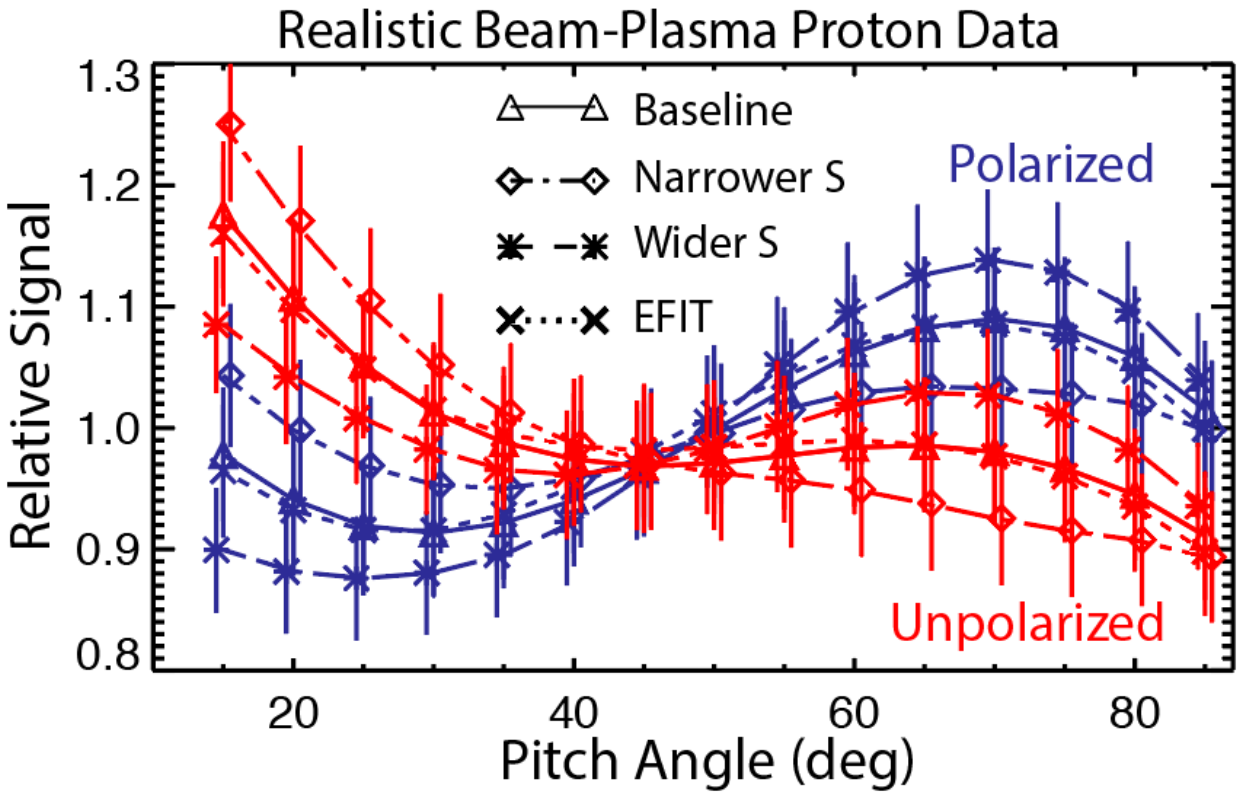

Figure 3.15: Realistic synthetic data for detection of 14.7 MeV protons at the $-56°$ port for unpolarized and tensor polarized deuterium pellets with $P_D^T = 0.41$. The calculations assume pitch angle resolution of 5°, 15° gyroangle resolution, and 50-ms temporal resolution. The figure format is the same as Figure 3.13(b).

reduced chi-squared is

$$\chi_r^2 = \frac{1}{N-1}\sum_{i=1}^{N}\frac{(\Delta s_i)^2}{\sigma_i^2}. \tag{3.9}$$

Here, N is the number of measurements (15 for protons and 3 for alphas), σ_i^2 is the random error associated with counting statistics for the polarized and unpolarized measurements and their normalizations (added in quadrature), and Δs_i is the difference between the polarized and unpolarized calculations for each measurement. To take account of the systematic errors associated with uncertainties in the emissivity profile and equilibrium reconstruction, the smallest value of $|\Delta s_i|$ of the four curves is utilized. The results of this calculation (Table 3.1) indicates that confident detection is feasible for the thermonuclear cases. Both the enhanced and the suppressed polarization states supply useful information. As shown in more detail in Appendix D, alpha detection is less sensitive to potential systematic errors and more accurate.

In the last column, Table 3.1 shows calculated values of χ_r^2 for the larger polarization values provided by ^{7}Li-D capsules. With this degree of polarization, extremely high confidence is obtained for both protons and alphas. However, there are caveats. First, this evaluation assumes the same deuterium density as for the H-D case but, owing to the higher Z of lithium compared to hydrogen, a smaller pellet is probably needed to keep the increase in electron density manageable. On the other hand, lithium injection is usually favorable for tokamak operation [76] so its presence may assist high T_i operation. Second, the ^{7}Li(p,α)α fusion reaction produces a background. At the 75 keV energy of hydrogen beam injection in DIII-D, the reaction cross section is $\sim 10^{-28}$ cm^2 [77], which implies a beam-plasma emissivity an order of magnitude smaller than the thermonuclear d-^{3}He emissivity. The reaction releases 17.3 MeV of energy, divided between the alphas. This implies that the proton and alpha diagnostics must include some energy and/or gyroradius discrimination to avoid this unwanted background.

In contrast to the thermonuclear case, uncertainties in the analyzed beam-plasma scenario compromise confident detection, even for the higher polarization values of ^{7}Li-D pellets (Table 3.1). Proton measurement of tensor-polarized ^{7}Li-D pellets is the most sensitive

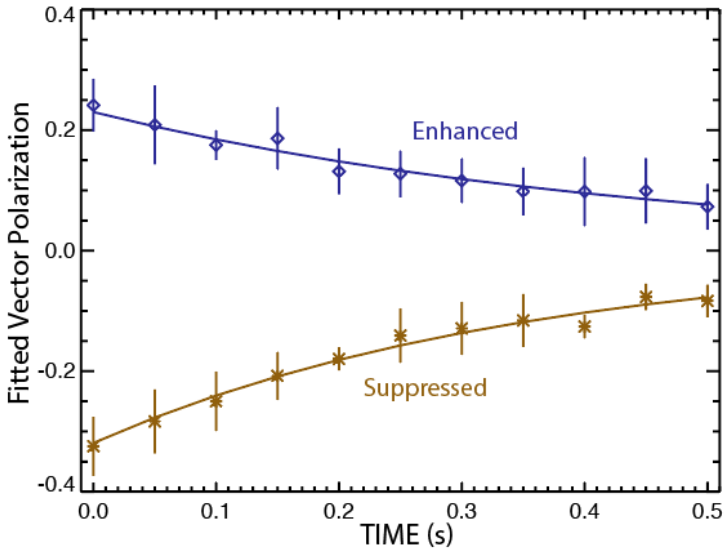

Figure 3.16: Time evolution of the fitted vector polarization $P_D^V P_{He}$ for hypothetical pitch-resolved 14.7 MeV proton data from the $-56°$ port. The $P_D^V P_{He}$ coefficient is inferred from data similar to Figure 3.13, assuming that P_D^T is given by Equation 3.10. Each symbol and error bar is from an ensemble of trials with randomly generated counting statistics. The lines are from subsequent exponential fits to the $P_D^V P_{He}$ coefficients. The hypothetical data assumed a $P_D^V P_{He}$ exponential decay time of 0.40 s; the exponential fits to the generated data are 0.45 ± 0.04 and 0.35 ± 0.04 s for the enhanced and suppressed cases, respectively.

but, as shown in Figure 3.15, the curves and error bars for the unpolarized and tensor-polarized cases partially overlap, a reflection of the smaller difference between the polarized and unpolarized cross sections [Figure 3.12(a,b)] and the lower reaction rate [Figure 3.12(c,d)] for the beam-plasma case compared to the thermonuclear case. Evidently, a ^{3}He beam that produces more reactions or summation over multiple shots or over larger time intervals is required for confident detection in this case. Alpha detection (not shown) is less sensitive than proton detection for this scenario.

In an actual experiment, one imagines making measurements like those shown in Figure 3.13 and Figure 3.14 in successive discharges with enhanced, suppressed, and unpolarized pellets. In each discharge, measurements are acquired for hundreds of milliseconds to track the decay of the polarization over time. Figure 3.16 shows hypothetical data from such an experiment for pitch-resolved 14.7 MeV proton emission from a thermonuclear plasma. The analysis for

that figure assumes that

$$P_D^T = 2 - \sqrt{4 - 3(P_D^V)^2}, \tag{3.10}$$

which is the initial tensor polarization associated with thermal equilibrium in a solid deuterium pellet. However, it should be noted that the different polarization terms P_D^T, P_D^V, and P_{He} may decay at different rates in an actual experiment. Nevertheless, the analysis shows that proton data suffice to measure the polarization lifetime with $\lesssim$15% accuracy.

Synthetic data like those analyzed to produce Figure 3.16 can be used to estimate the one-sigma uncertainty in the inferred polarization. For pitch-resolved 14.7 MeV proton data from the $-56°$ port in a thermonuclear experiment, the uncertainty in $P_D^V P_{He}$ is ~ 0.04. For 14.7 MeV proton data from the same port in a beam-plasma experiment, the uncertainty in P_D^T is ~ 0.10. For a poloidal array of three 3.6 MeV alpha detectors, the uncertainty associated with counting statistics in inferring either $P_D^V P_{He}$ in a thermonuclear experiment or P_D^T in a beam-plasma experiment is very small (< 0.01), implying that systematic errors will determine the ultimate resolution.

Although we emphasize individual relative measurements here, in an actual experiment, all available data would be utilized in a unified framework, including measurements of the total D-^{3}He rate, T_i and n_{He} profiles measured by charge exchange recombination (CER) spectroscopy [78], and the n_D profile measured by the main-ion CER diagnostic [79]. In that regard, inclusion in the diagnostic suite of a gamma-ray detector that measures the total D-^{3}He rate is particularly attractive.

In addition to the primary branch that produces the 14.7 MeV proton and 3.6 MeV alpha, the D-^{3}He reaction also produces a pair of gammas at 16.9 MeV and 15.4 MeV, with a branching ratio of approximately 4.5×10^{-5} at fusion relevant energies for the 16.9 MeV gamma [80]. The differential cross sections for these reactions are sensitive to the D and

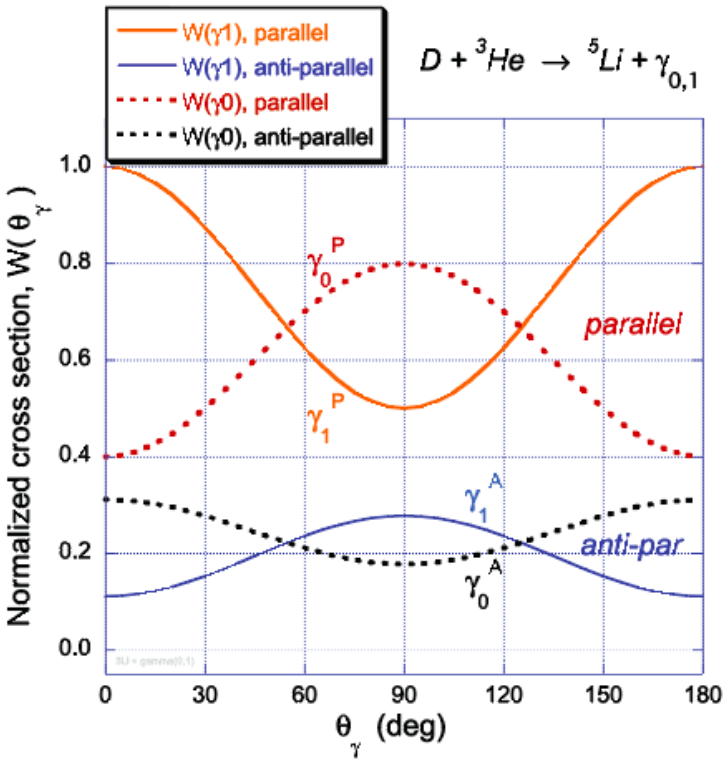

Figure 3.17: Angular dependence $W(\theta)$ of the differential cross section for gamma emission to the ground and first excited state for D and ^{3}He nuclei with parallel or anti-parallel spins. These distributions assume the ideal case of 100% polarization of the initial D and ^{3}He spins.

^{3}He spin states. The differential cross section is the product of three factors: the square of a reduced matrix element, the branching ratio for gamma decay of the ^{5}Li nucleus, and an angular weight $W(\theta)$, where θ is the angle of emission of the gamma relative to the local magnetic field. The evaluation of W for ^{5}Li gamma decay is analogous to the calculation outlined in Appendix A of [71] for the α + proton final state. As shown in Figure 3.17, the two gammas depend differently on the emission direction; both are sensitive to the alignment of the D and ^{3}He spins.

If gammas are detected "with equal efficiency" from all possible locations throughout the torus, and so from points with all possible field direction at the moment of fusion, then one effectively integrates over the plotted W distributions. While it may not seem obvious at first sight, the integrals of the $\gamma(0)$ and $\gamma(1)$ distributions are in fact identical; this is true for both

the case with parallel D and ^{3}He spins, as well as for the anti-parallel case. Furthermore, the integral of W with parallel initial spins is three times larger than the integral of W with anti-parallel spins, and that is true for both $\gamma(0)$ and $\gamma(1)$. This factor of three is the same polarization enhancement that occurs in the alpha + proton final state.

In principle, with a collimated gamma detector such as the vertically viewing instrument that measures emission at $\sim 90^\circ$ at JET [81], one could exploit the differing angular dependencies of the two gammas in Figure 3.17 to detect the polarization state of the nuclei. Because the natural line widths of the two gammas are quite large ($\Gamma_0 = 1.2$ MeV and $\Gamma_1 = 6.6$ MeV, respectively), the measured spectrum must be deconvolved to infer the relative contributions of each gamma but, with adequate energy resolution and counting statistics, that can be done accurately [82, 83].

Unfortunately, owing to the low branching ratio, the count rate is too low for collimated gamma measurements in DIII-D. To obtain adequate counting statistics, a detector should have large intrinsic efficiency, large area, and large solid angle. Estimates indicate that a $\sim 10^3$ cm^3 bismuth germanate (BGO) scintillator mounted just outside the vacuum vessel would measure $> 10^4$ cps in the thermonuclear shots. Because such a detector would detect gammas with many values of θ from a large spatial volume, the measurement is insensitive to uncertainties in emission profile and equilibrium reconstructions ($\int S\,dl$), thus providing a valuable complement to the primary CFP diagnostics. In discharges with large D-D neutron rates, the large (n,γ) background produced by 2.45 MeV neutrons can obscure the relatively weak D-^{3}He gamma peak but, in our thermonuclear scenario, the D-D rate is orders of magnitude smaller than in those discharges, so the (n,γ) background should be manageable. A review of gamma-ray diagnostics in tokamaks appears in [84] and an example of successful recent detection appears in [83].

3.5 Discussion

The previous section gave a realistic, quantitative assessment of experimental feasibility. In this section, additional complications and considerations are discussed, often qualitatively.

There are multiple issues associated with delivery of the pellet fuel. The actual preparation and delivery of spin-polarized pellets has many challenges that are discussed in detail elsewhere [67]. To summarize, we envision filling gas-discharge-polymer (GDP) shells like those used in inertial fusion research [85] with polarized fuel. For the ^{3}He, the nuclei are polarized prior to diffusing through the shell; for deuterium, the pellet contains both H and D so RF can be used to transfer H spin to D. Once prepared, the shell pellets are injected vertically into the tokamak from a 77 K cryogenically cooled gun for the ^{3}He pellets and a 2 K gun for the H-D pellets [71].

A measurement of the polarization upon entry into the tokamak is desirable since, due to inhomogeneity of the magnetic field, some nuclei may depolarize during pellet injection. For example, the loops of a superconducting quantum interference device (SQUID) located at the end of the flight tube could be used to measure fluctuations in the magnetic field produced from changes in the depolarization of the nuclei upon entry. If this depolarization mechanism is operative, it will occur too rapidly to be detected accurately by the CFP measurements. On the other hand, as long as the signal-to-noise ratio remains adequate, if the actual injected polarization differs somewhat from the expected (or measured) value, this does not preclude study of the other depolarization mechanisms (such as wave-induced depolarization), since one could still infer the lifetime of polarization from a time series of accurate CFP measurements.

Another issue related to pellet delivery is that, most likely, the fuel will be deposited away from the magnetic axis. Central deposition is achievable with large pellets but large increases in density are incompatible with the desired high T_i regime. The injected pellets resemble the

"shell pellets" employed in disruption mitigation experiments [86]. The required quantity of ^{3}He fuel is similar to the amount of argon delivered in the shell-pellet experiments. For example, in a disruption mitigation experiment, a 2-mm-diameter pellet with 10 atm argon fill delivered its payload near a normalized minor radius of $\rho \simeq 0.4$ [86]. Central deposition is enhanced by pellet injection from the high-field side [87] so, if this is compatible with preservation of the polarization during injection, high-field side (or vertical) injection is preferable to low-field side injection. The calculations presented above assume centrally peaked n_d and n_{3He} profiles (Figure 3.2b), so, almost certainly, some convective inward transport is required to bring the fuel into the high fusion emissivity region. Inward transport rates are scenario and species dependent and are not well established for the desired plasma conditions. A likely timescale is 50-100 ms. Empirically, low collisionality favors density peaking [88] and the desired regime has low collisionality. In TFTR experiments, ^{3}He puffed at the plasma edge reached the core with inward transport times of $\sim$ 100 ms [89]. Thus, we anticipate inward transport of the pellet payload to the high fusion emissivity region will occur on an acceptable timescale in an actual experiment, but this assumption requires further study and experiments.

Another issue that requires further research is the optimal size of the pellets. In the absence of large MHD or changes in confinement regime, the stored energy often remains roughly constant after pellet injection, so the fractional increase in density is approximately equal to the fractional reduction in temperature, $\Delta n/n \simeq -\Delta T/T$. The thermonuclear D-^{3}He reaction rate is proportional to $n_D n_{3He} \langle \sigma v \rangle$, with the reactivity being a strong function of T_i. Although smaller pellets have lower values of $n_D n_{3He}$, the reaction rate is not necessarily lower than assumed in our thermonuclear scenario, since $\langle \sigma v \rangle$ is larger for a smaller reduction in T_i.

A related issue is the timing of pellet injection. Ideally, to measure the polarization lifetime for as long as possible and to isolate different possible depolarization mechanisms, the fuel

would immediately be heated to high temperature. However, pellet injection into a high T_i regime with properties resembling the desired one often triggers disruptions or confinement-degrading neoclassical tearing modes [90]. It may be necessary to inject less fuel than assumed in section 3.2, so repeat discharges might be required to achieve suitable accuracy. Alternatively, injection prior to the high-power phase could prove more stable but this might prevent detection of relatively rapid depolarization mechanisms. Once again, additional experiments to establish the best scenario are desirable.

Backgrounds associated with D+D fusion reactions are manageable. There are two backgrounds to consider, one associated with the D+D $\rightarrow$ 2.4 MeV neutron + 0.8 MeV ^{3}He branch and another associated with the D+D $\rightarrow$ 3.0 MeV proton + 1.0 MeV triton branch. For equal deuterium and 3He concentrations at $T_i = 10$ keV, the emissivity of each of these D+D branches is 1.3 times larger than the D-^{3}He emissivity. The concern for the neutron-^{3}He branch is that 0.8 MeV ^{3}He ions produce secondary "burnup" D-^{3}He reactions as they slow down [91]. Most 0.8 MeV ^{3}He ions produced in D-D reactions are confined in a 1.1 MA plasma but, for an average electron temperature of $\langle T_e \rangle = 2.5$ keV, only 6×10^{-3} of the ^{3}He ions produce a secondary D-^{3}He reaction as they thermalize, so secondary reactions produce 14.7 MeV protons and 3.6 MeV alphas at $< 1\%$ of the thermonuclear D-^{3}He rate.

The proton-triton branch is of greater concern. The orbits of 3.0 MeV protons and 1.0 MeV tritons are very similar to 3.6 MeV alpha orbits. Moreover, as discussed below, the differential cross section for the D+D reaction has an unknown but likely significant dependence on spin polarization, so it is essential to distinguish the D+D fusion products from the D+^{3}He ones. A scintillator-based FILD detector is envisioned for the pitch-resolved 14.7 MeV measurement. Since the gyroradius of the 14.7 MeV proton is 2.2 times larger than the 3.0 MeV proton gyroradius, the two proton "spots" on the FILD scintillator plate are widely separated and easily distinguished. However, for the 3.6 MeV alpha flux measurement, the gyroradius is only 1.2 times larger, so a different discrimination method is required. Here,

one could exploit the difference in range between protons and alphas in a pulse-counting energy measurement. The range of a 3.0 MeV proton in silicon is 92 microns, while the range of a 3.6 MeV alpha is only 15 microns. If one uses a thin $\sim$ 15 micron silicon detector to measure the alphas, their $\sim$ 3 MeV peak can be readily distinguished from the lower-energy pulses deposited in the detector by the protons and tritons.

Since DIII-D normally operates in deuterium, it would be simpler operationally to study the polarization lifetime using D-D fusion reactions rather than D-^{3}He reactions. The complication with D-D reactions is that, although they are known to be anisotropic even with unpolarized fuel [56], the dependence of the differential cross section on spin polarization is controversial theoretically. Hence, although it is likely that there is *some* dependence, the magnitude of the expected effect is unknown. Nevertheless, one can imagine making measurements with polarized and unpolarized deuterium pellets in scenarios similar to the ones described here. For the thermonuclear case, only deuterium pellets would be injected; for the beam-plasma case, an unpolarized deuterium beam would replace the unpolarized ^{3}He beam. The confinement of the 3 MeV protons produced in D-D reactions is nearly identical to 3.6 MeV alpha confinement, so the alpha flux detectors (perhaps with thicker silicon diodes) could be used to measure the escaping 3 MeV protons. Since the D-D reaction rate is comparable to the D-^{3}He rate for those conditions, count rates remain adequate. If either scenario produces a measurable dependence on polarization, then the lifetime of the polarization could be inferred from the rate of decay of the effect, even without knowledge of the expected initial value.

Although DIII-D should provide reactor-relevant tests of depolarization by plasma waves and Coulomb collisions, DIII-D is not equipped to study depolarization at the walls under reactor-relevant conditions. DIII-D is a graphite-wall device and carbon is predicted to retain too much tritium for use in a reactor [92]. Depolarization at a metal wall is predicted to be more rapid than with a carbon wall [93]. Another likely difference is the importance

of recycling. In DIII-D, even during divertor operation, nuclei often return to the plasma after interacting with the wall. Depending on the ultimate design of the divertor, recycling is likely to be less important in a reactor. The majority of escaping fuel will be reprocessed. As an aside, although polarizing the fuel adds additional complexity and cost to a fusion power plant, in a D-T reactor, reprocessing of tritium is absolutely essential [94], so polarizing the fuel merely adds an additional step to the multi-step tritium recovery process.

An attractive alternative approach that is not currently possible on DIII-D is to use ion cyclotron resonance heating (ICRH) of a dilute ^{3}He population to produce a large beam-target D-^{3}He reaction rate. (DIII-D is not equipped with an ICRH capability but many other facilities are.) Minority heating of ^{3}He at its fundamental cyclotron frequency [95] has been employed in tokamaks for decades and is a very effective way to create a fast-ion population at energies that produce abundant D-^{3}He reactions [22]. For example, on the Princeton Large Torus (PLT), a population of ICRH-accelerated ^{3}He ions with energies in the 100-400 keV range produced large reaction rates [96] and energy-resolved 14.7 MeV proton measurements showed that the perpendicular energy of the reacting ^{3}He ions was much larger than the parallel energy [69]. A possible scenario is to accelerate a small ^{3}He population (concentration $\sim$ 5%) to $\sim$ 200 keV energies in a ^{4}He plasma, then inject a tensor-polarized deuterium pellet. In a device where 14.7 MeV protons escape with little change in pitch (as in PLT), the signals from collimated proton detectors at two different pitch angles (such as 40° and 90°) would be directly proportional to $d\sigma_+/d\Omega$ (Figure 3.12b); measurements of the energy spectra [69] would confirm the origin of the reactions. The ideal device for such an experiment has (i) magnetic fields that are large enough to confine $\sim$ 400 keV ^{3}He ions but low enough that 14.7 MeV protons readily escape and (ii) relatively small volume in order to minimize the amount of polarized fuel required for adequate signals.

3.6 Conclusion

Polarized fuels could significantly enhance the performance of a burning plasma, provided that the polarizations are retained for periods comparable to the burn-up time. This chapter focuses on detection of polarization-dependent changes in the differential cross section $d\sigma/d\Omega$ in order to measure the lifetime of spin-polarized fuel. A suitable facility needs unconfined fusion products to facilitate detection, either polarized beams or hot ($T_i \gtrsim 10$ keV) plasmas to produce adequate count rates, and reactor-relevant depolarization mechanisms. DIII-D provides all three. The most promising detection strategy is a poloidal array of 3.6 MeV alpha flux detectors. A pitch-resolving 14.7 MeV proton detector located at a poloidal angle of -56° is also sensitive. Both detection schemes are sensitive for a wide range of plasma currents. For either detection strategy, polarizations that either enhance or suppress the total cross section provide detectable signals. Quantitative assessment of uncertainties shows that these strategies can detect the presence of polarization with high confidence, even for the less than maximal values of polarization available with existing technology. Although substantial technical challenges must be overcome to successfully deliver the polarized fuel to the plasma core, this study shows that, if those obstacles are surmounted, accurate lifetime measurements of the polarization are feasible on DIII-D.

Chapter 4

Alfvén Eigenmode detection using Machine Learning on DIII-D

4.1 Introduction

The successful operation of planned nuclear fusion devices such as ITER depends on confined populations of super-thermal particles that heat fuel ions for a self-sustaining plasma burn [97]. If confined, alpha particles born from fusion reactions can provide the heating required to reach ignition. If these alphas become unconfined, they can carry away fusion power and damage the first walls [98, 99]. The heat loss can be replaced using auxiliary heating mechanisms such as neutral beam injection (NBI) or radio frequency (RF) waves and both of these methods can create populations of fast ions that are useful for momentum transfer and current drive [100]. Fast ions born from fusion reactions or external heating can resonate with special types of plasma waves called Alfvén eigenmodes (AEs) [23, 101, 102], transfer energy to the wave, drive the plasma unstable and degrade energy confinement [24, 25]. Also, particle redistribution can expel fast ions from the plasma [24–30] and damage

the inner walls of the vessel [31, 32]. Therefore, studying fast ions and controlling AEs is imperative for the realization of controlled nuclear fusion.

Real-time control of AEs in high performance burning plasmas without damage to the inner walls is a high priority objective for the Plasma Control System (PCS) at ITER [103, 104]. It is currently an important goal to determine the best set of external actuators in order to control AEs and alpha losses [17]. Suitable techniques include electron cyclotron resonance heating (ECRH) and current drive, and neutral beam injection. Since AEs can appear for short time scales on the order of milliseconds, simple feed-forward physics models are used to detect and control AEs. There is a need in the community for models with quick response times that could accurately detect the presence of AEs in real-time experiments.

Machine Learning (ML) applications in magnetic confinement fusion energy are growing and exciting opportunities exist in the fast-ion physics research field. Currently, the largest application of ML is in the area of disruption mitigation, where models are trained to prevent the rapid loss of thermal and magnetic energy during a quench of the plasma [105–112]. Surrogate model generation and experimental planning also benefit from data-driven methods [113]. On the other hand, ML in fast-ion research is a relatively new field. For example, Alfvénic and magnetohydrodynamic modes were detected using deep learning-based models, manually-labeled targets and magnetics on TJ-II [114] and COMPASS [115]. More examples used supervised learning to detect AEs [114–116], and data mining techniques combined with clustering for extraction of plasma fluctuations [117, 118].

In recent years, significant advancements have been made in detecting and controlling AEs using electron-cyclotron emission (ECE) data on DIII-D. Originally, in-shot variation of neutral beam energy showed promise for AE control [18], then the first active real-time control of AEs in a tokamak utilized modulated beams to tune the drive for AEs using feedback from high resolution ECE signals [31]. Shortly after, the Large 2009–2017 DIII-D AE Energetic Particle Database [119] was created to better understand low frequency

AEs and was later used for machine learning analysis in two papers [120, 121]. Deep Neural Networks were trained using ECE data in both studies. Reservoir Computing Networks (RCN) and Multi-layer Perceptron (MLP) Networks were trained in the former and latter study, respectively, and both achieved high performance. section 4.2 of this chapter discusses the Large AE-EP Database in more detail.

In this work, we focus on training Recurrent Neural Networks and labels created from the Large AE-EP Database, but use CO_2 interferometer data instead of ECE since there are several advantages: 1) calculating crosspower spectrograms between two chords is common in the fast-ion physics community since AE patterns can be highly visible in this representation of the data, 2) the 1D phase signals are routinely processed by the Plasma Control System for nearly every discharge and can be used for real-time control in future DIII-D experiments, and 3) although ECE measurements are high resolution and can measure AE fluctuations with good signal-to-noise, issues associated with resonances and cutoff frequencies pose challenges for AE detection. Using the CO_2 interferometer for AE identification is useful for reliably detecting AEs since it does not have limitations with cutoffs. For reasons 2 and 3, more shots are available in the Large AE-EP Database to train data-driven models. The baseline technique was initially trained to detect AEs using CO_2 Interferometer data in a conference paper [3], and we report significant advancements here.

Building from our prior work, the primary objective of this chapter is to study the performance by comparing the following: 1) different feature sets (simple magnitude and crosspower spectrograms), 2) recurrent neural networks (RCN vs LSTM), and 3) stacking outputs vs individual crosspower. The state-of-the-art (SOTA) technique in [120] used 40 stacked time-domain signals of ECE data and created labels from the Large AE-EP Database to train an RCN. We instead use spectrograms of CO_2 interferometer data, and individually forward pass each chord through both Neural Networks one-at-a-time and compare the results. The aim is to match our prior performance by training with CO_2 interferometer data

for the potential long-term goal of creating an ML detector that could be useful in real-time AE control.

This chapter is organized as follows: the CO_2 interferometer on DIII-D, labels from the Large AE-EP Database and important challenges are discussed in section 4.2. The results of model and feature comparison are shown in section 4.3. Correlation analysis between predictions and metadata (equilibrium, beam, etc.) are reported in section 4.4. Conclusions appear in section 4.5.

4.2 Experimental Data

DIII-D is a well diagnosed tokamak housing many diagnostic systems that measure the effects of AEs, with large amounts of available data from decades of experimental campaigns. Electron cyclotron emission [122], CO_2 interferometry [123], beam emission spectroscopy [124], and magnetic fluctuation diagnostic systems [125] can be used to study the effects of fast-ion driven instabilities. Diagnostic and plasma information can be relayed to actuators for real-time control of AEs in DIII-D experiments [17–20].

The two-color vibration compensated CO_2 interferometer is a real-time system routinely used for feedback control of the plasma state at DIII-D. Additionally, it can provide useful information about the internal mode structure of AEs since it observes the AE induced density perturbations with a resolution in the $\Delta(nL)/nL \sim 10^{-5}$ range at the frequencies of interest. A layout of the CO_2 interferometer for an example equilibrium is displayed in Figure 4.1. All four chords (3 vertical and 1 horizontal) are digitized for 9 seconds per shot at a rate of 1.67 MS/s, and the CO_2 phase data are studied in this work since AE frequencies are well above typical mechanical vibration frequencies. Also, the phase data are processed in real time by the Plasma Control System at DIII-D, making the AE detector in this work

applicable for actuator driven mitigation of AE impacts.

In the past, identfication of AEs was usually done in a post-shot framework using crosspower spectrograms of CO_2 interferometer data and other AE fluctuation diagnostics (or plasma parameters). Doing spectral analysis is useful since generating spectrograms can remove low frequency noise and machine vibrations seen in the 1D signals. Although this method worked, it can be time consuming and requires extensive domain knowledge. In this work, we automate the identification process by training RCNs and LSTMs using simple and crosspower spectrograms of CO_2 interferometer data.

The original curated Large AE-EP Database was created to investigate the dependence of AE stability on plasma parameters in over 1,139 shots [119]. It includes the occurrences of six plasma instabilities: ellipticity (EAE), toroidal (TAE), reversed-shear (RSAE), beta-induced (BAE), low-frequency mode (LFM), and energetic particle-induced geodesic acoustic mode (EGAM) [119]. Table I of [120] shows a description of these modes. Times were selected when the various AEs were stable, marginal, or unstable. The number of time stamps per discharge was chosen to sample changes in plasma parameters and mode activity in a representative fashion. Time stamps usually appear in the middle of a type of activity, and many occur during the first 1.9 s since some AEs depend on the q profile and q steadily evolves during that phase of the discharge.

There are several challenges using the Large AE-EP Database and they are addressed here. The time stamps need to first be made binary and we adopt the one-hot encoding method described in Table II of [120]. We consider AEs originally marked unstable as being *present* in the discharge and mark them as 1, otherwise flags are reassigned to 0. Figure 4.2 shows the *presence* of AEs over the selected 1069 shots studied in this chapter. Since predicting single time stamps is a challenge for ML-based methods, the re-assigned flag for all AEs are widened over ± 125 ms. This completes the creation of the labels used to train the RCN and LSTM in this work. The third challenge is shown in Figure 4.3, where the distribution of

labels is imbalanced and heavily skewed towards TAE and RSAE. This imbalance motivates using true positive rate (TPR) and false positive rate (FPR) as the metrics of success since the accuracy metric would be 94 % if a model always predicted 0. TPR and FPR are defined as follows:

$$\begin{aligned} \text{TPR} &= \frac{\text{TP}}{\text{TP} + \text{FN}} \\ \text{FPR} &= \frac{\text{FP}}{\text{FP} + \text{TN}} \end{aligned} \tag{4.1}$$

where TP = true positive, FN = false negative, FP = false positive, and TN = true negative. Although the ML classifiers train using information over the entire discharge and the original curated label is only available at discrete random times, TP and FP are modified such that a given prediction is reassigned only if an AE label is nearby within a window of ± 140 ms. Lastly, CO_2 interferometer, ECE and magnetics were all used to originally classify AEs in the Large AE-EP Database, which creates a classification challenge since a certain mode might show up more clearly in a different diagnostic than the CO_2 interferometer.

Given these challenges, our prior work using ECE data accomplished true positive rate = 91 % and false positive rate = 7 %, (Table III of [120]). Our aim here is to match or improve these results using different feature sets of a new diagnostic system (CO_2 interferometer) and recurrent neural networks (RCN vs. LSTM).

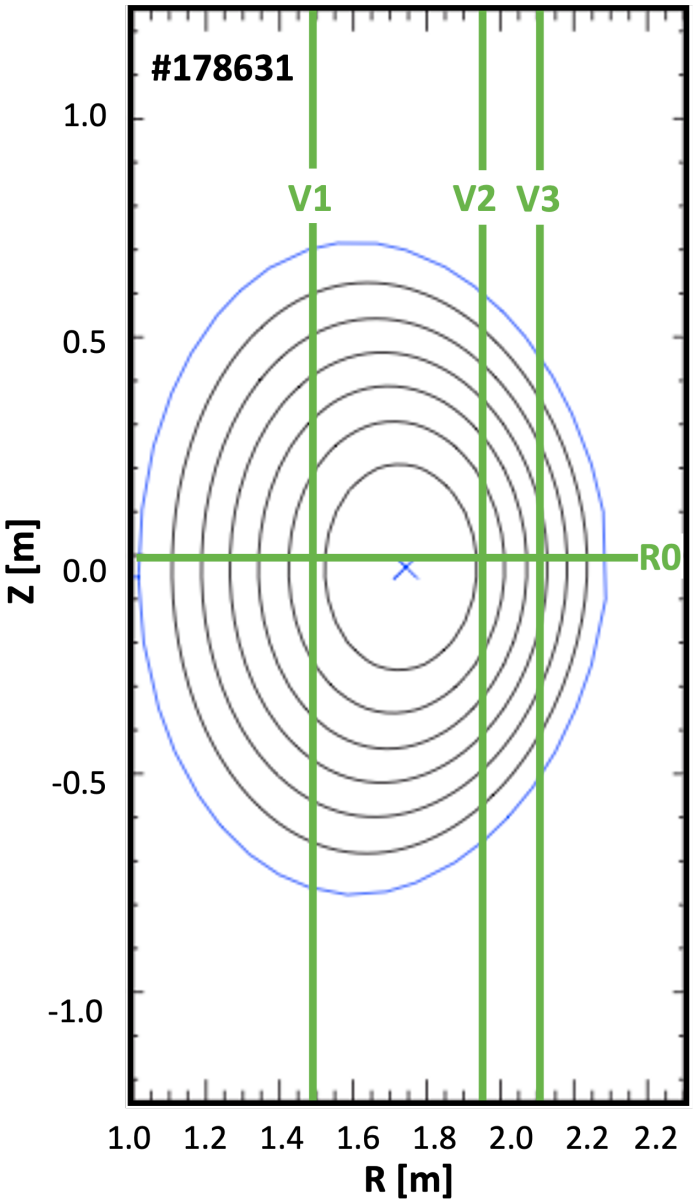

Figure 4.1: The elevation view of the CO_2 interferometer installed on DIII-D for shot #178631. Three vertical chords are located at R_m of 1.48 m, 1.94 m and 2.10 m, and the radial chord is horizontal on the midplane. The black curves are the magnetic flux surfaces (the last closed flux surface is in blue). The magnetic axis is denoted by the blue $\times$ symbol.

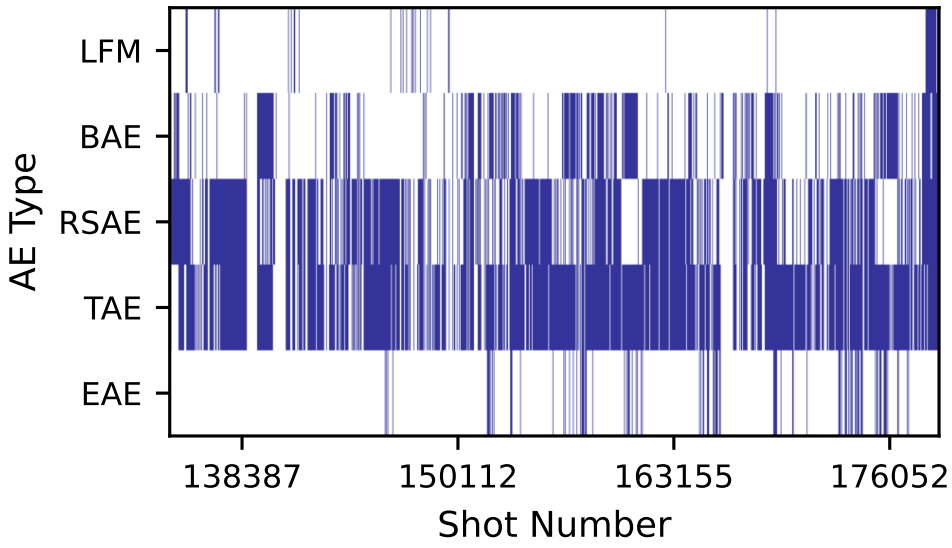

Figure 4.2: The *presence* of AE label vs. shot number shows TAE and RSAE are labelled frequently across many experimental campaigns. LFM, BAE and EAE have relatively sparse representation in the database.

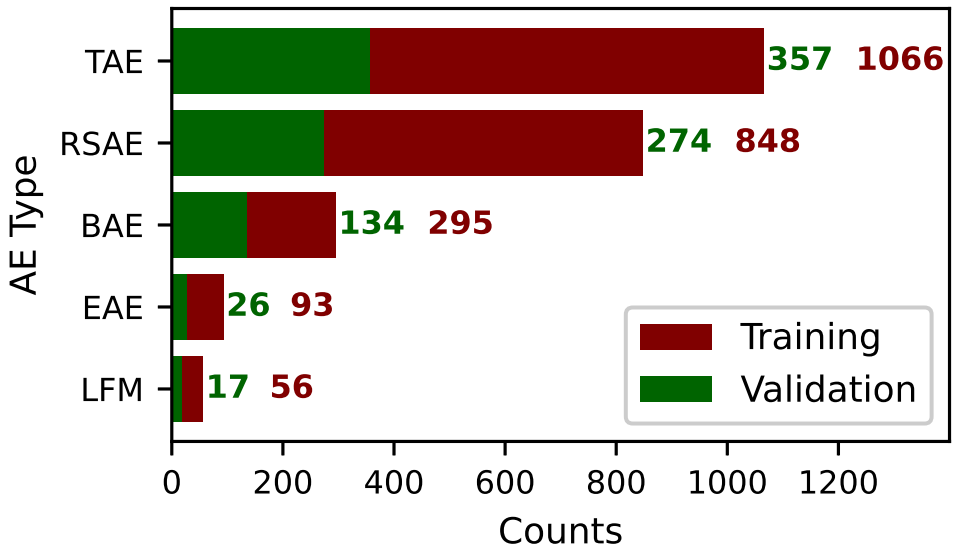

Figure 4.3: The occurrence of labels for the training set (801 shots) and validation set (268 shots) are skewed towards TAE and RSAE. The sets are randomly shuffled to preserve distribution shape. In comparision, there are barely any LFM or EAE instances throughout the database.

4.3 Comparisons and results

In an effort to discover the best performing Machine learning-based model for this new CO_2 interferometer project, several methods are explored in the following order: 1) Linear Regression, 2) Multi-Layer Perceptrons, 3) Convolutional Neural Networks (convnet), and 4) Recurrent Neural Networks. A brief, qualitative summary for the regression, MLP and convnet classification appear in Appendix D. Details about the linear baseline classification for single chord analysis using CO_2 interferometer data are shown in [3], and significant advancements are made in this work. Here, three major goals are addressed:

1. Compare the features of different inputs, i.e., simple magnitude and advanced crosspower spectrograms. The extraction of these different feature sets is discussed in subsection 4.3.1

2. Determine the best performing recurrent neural network (RCN or LSTM) for this study. The different models are introduced in subsection 4.3.2.

3. Compare the performance of stacking outputs vs. crosspower combinations (2 simple spectrogram chords and 1 crosspower calculation). Results are shown in subsection 4.3.3.

4.3.1 Inputs

The inputs for both recurrent neural networks are simple magnitude and advanced crosspower spectrograms. These are windowed Fourier transform calulations using a window length of 4.9 ms and overlap of 80 %. The spectrograms are downsampled using a maxpool function and the final input shapes are (time, frequency) = (140, 508). Maxpooling is commonly used in computer vision tasks and produced good results in this work. For the LSTM model,

spectrograms are "cut" into 280 ms windows, concatenated and fed into the model. For the RCN case, windowing is not implemented and the model processes 1D vectors of frequencies per training step. More details about the input preparation for the LSTM model can be viewed in Section III of [3].

4.3.2 Architectures

The Python toolbox PyRCN (Python Reservoir Computing Networks) [126] is used for optimizing and training the RCN in this classification project. We utilize the more common RCN architecture, Echo State Networks (ESNs) [127], to perform the classification of AEs. Also, the hyper-parameter optimization routine is handled within the PyRCN framework and is based on the search strategy introduced in [128].

A 2-layer RCN is developed by sequentially stacking two RCNs [129] on top of each other. It has been shown in [128–130] that stacking RCNs increases the temporal model capacity and reduces errors learned in early layers by rectifying their outputs in the subsequent layers. Larger capacity (more temporal information) can improve the RCN's performance in detecting specific AEs such as LFM. Figure 4.4 shows a diagram of this architecture. The RCN processes a timestamp vector of frequency values ($N_{freq} \times 1$) and uses the provided labels ($N_{modes} \times 1$) to train the readout layer. The output of the first RCN are scores for each of the five AEs. This output vector is then fed into the second RCN as input and the second readout layer is trained using the same labels. The final outputs are rectified scores for each AE.

The hyperparameter optimization strategy closely follows the method described in Section 3c of [128]. Table 4.1 shows the results from the hyperparameter optimization routine for both layers. The process uses a 3-step sequence of searches for the hyperparameters input scaling, spectral radius, bias scaling and leakage. The steps of the method are as follows:

1. Perform a random search for the input scaling and spectral radius while the bias scaling and leakage terms are held constant.

2. Fix the leakage to 1 and search for the bias scaling.

3. Search for the leakage term.

Step 1 determines the balance between forward and recurrent connections, Step 2 can introduce more non-linearity into the system, and Step 3 determines the attention the network gives to temporal information in the inputs. The hyperparameters at each step are selected based on the minimization of the mean squared error (MSE) curve.

The LSTM model consists of three layers using Long-Short Term Memory cells, one dropout layer and four layers using Multi-layer Perceptrons. This type of architecture will consider memory in the inputs and generate AE scores. Refer to [3] for more information about this model. The hyperparameters shown in Table 4.2 are optimized by sequentially scanning values and analyzing predictions over three selected discharges.

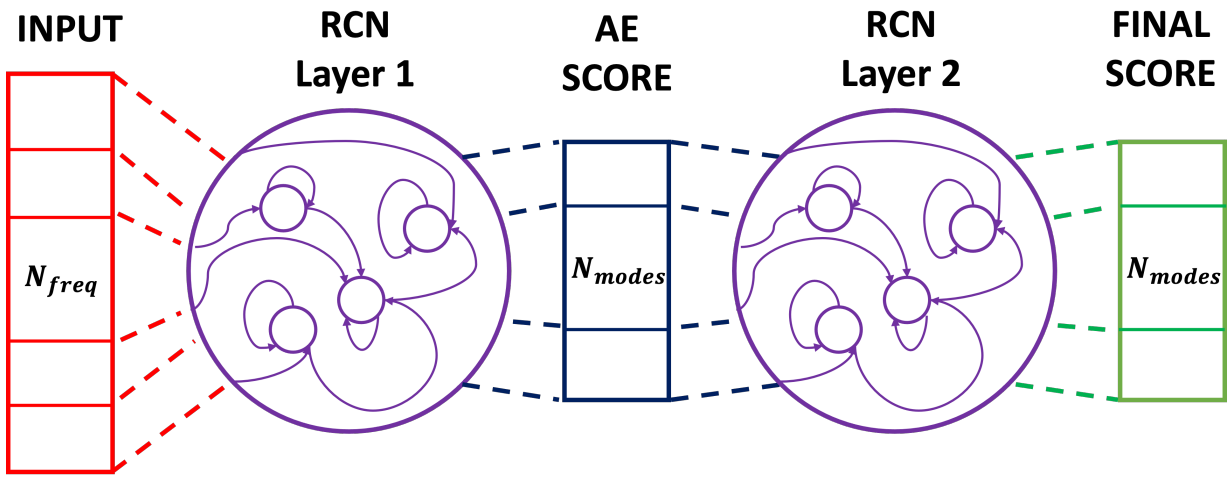

Figure 4.4: Schematic of the stacked 2-layer RCN used to classify AEs trained with simple and crosspower spectrograms. The input layer of the first RCN is connected to a reservoir of nonlinear neurons and gets mapped to a higher dimensional space, where the data are more separable. The readout layer of the first RCN is trained using linear regression and processed as inputs for the second RCN. The second reservoir consists of less neurons since less model capacity is needed to rectify the mistakes of the first layer. The final outputs are AE scores.

Table 4.1: The results from the hyperparameter optimization routines used to train the RCN network. A sequential search hyperparameter optimization strategy is used to train the readout layers of the stacked 2-layer RCN. Final values for each hyperparameter and each layer are reported in the final two columns.

Hyper-parameter	**Range**	**Distribution**	**Layer 1**	**Layer 2**
Input scaling	1×10^{-5} to 1	uniform	0.03	0.09
Spectral radius	0 to 2	uniform	1.27	0.39
Leakage	1×10^{-5} to 1	log uniform	0.71	0.71
Bias scaling	1×10^{-2} to 1	uniform	0.27	0.13
Alpha	1×10^{-5} to 10	loguniform	6.60	0.00

Table 4.2: Similar to Table 4.1, only for the LSTM network. A simple sequential scan is implemented here. Final values are listed in the last column.

Hyperparameter	**Range**	**Step size**	**Final**
Optimizer	Adam, Adamax, RMSprop	N/A	Adam
Learning rate	$10^{-2} - 10^{-6}$	$\times 10^{-1}$	10^{-4}
Layers (LSTM)	$2 - 9$	$+1$	3
Nodes (LSTM)	$32 - 256$	$\times 2$	64
Layers (MLP)	$1 - 3$	$+1$	3
Nodes (MLP)	$64 - 512$	$\times 2$	128
Dropout layers	$1 - 3$	$+1$	1
Dropout threshold	$0.25 - 0.75$	$+0.25$	0.5

4.3.3 Results

A data-driven convention is initially implemented to evaluate the performance of the model, and detailed analysis of the predicted errors follow. Thus, the TP and FP metrics are modified such that the time slice of each prediction is reassigned if any AE label information is available within a window of ± 140 ms of the predicted timeslice. Two examples at the end of this section show a few observed errors. Also, comparisons here evaluate performance over all four CO_2 interferometer chords.

The classification results that compare the RCN and LSTM model for simple and crosspower spectrograms are summarized by Table 4.3. The results for the simple spectrograms are nearly equal or better than crosspower spectrograms for the RCN and LSTM model. Also, the RCN performs slightly better than the LSTM model when using simple spectrograms. The LSTM can trigger slightly stronger predictions than the RCN. This is visible in the slightly higher TPR for EAE and FPR for TAE and RSAE. Figure 4.5 is a specific example with a lot of AE activity that demonstrates the feature set comparison using the RCN and LSTM models.

Both models might be slightly overestimating detection of TAE and RSAE since the FPR is relatively higher for these AEs. Since AE scores of the RCN are slightly lower, the overestimation effect is smaller. In regions where the AI failed, this is likely due to several reasons: 1) models are overfitting to training data, 2) noise in the CO_2 interferometer spectrograms, 3) latency associated with sparse time stamp, 4) general AI error. However, there are cases where the AI is working well, but an error is assigned. Possible reasons for this are the following: Incorrect value assigned to curated database through A) Δt label extension and B) calling no label stable, and C) some cases can be ambiguous. Figure 4.6 illustrates some of these points. Despite these issues, both models are capable of learning the patterns associated with AEs in this database and achieve high performance.

The RCN model demonstrates better results, and additional advantages include finer resolved predictions and the training speed for an RCN can be faster than for an LSTM. The RCN improved the linear baseline technique in [3] substantially since the memory of the model is higher with the addition of reservoirs containing random recurrent connections. Figure 4.7 shows the effect of adding a second layer to the RCN model. This effect is similarly observed when adding a third layer and increasing the number of nodes to 64 for the LSTM model.

In an effort to determine the set of chords with the highest AE detection, we check the performance for one chord, two-stacked chords or one crosspower combination using the F_2 score. This metric is a harmonic mean of the recall (TPR) and precision $\left(\frac{TP}{TP+FP}\right)$ metrics, where $\beta = 2$ in the following equation:

$$F_\beta = \frac{1+\beta^2}{\frac{\beta^2}{Recall} + \frac{1}{Precision}}. \tag{4.2}$$

The metrics TP and FP are further modified here by an additional $\Delta t = \pm 71\,\text{ms}$ in the calculation of the F_2 score to capture more information per chord from the discharges. These values are collected into a confusion matrix shown in Figure 4.8. For the upper diagonal (crosspower), the best performing combinations are V2R0, V3R0 and V2V2. The anecdotal favorite combination in the control room during experiments at DIII-D is V2R0 and the RCN model scores highest for this combination. For the lower diagonal (stacking outputs), adding predictions from V2 to V1 and any chord to R0 slightly improves the performance of V1 and R0, respectively. Although these differences are small, additional AE information from different chords might be needed when predicting using chords V1 or R0. Lastly, the darkest shaded region indicates that predictions for chord V2 achieve the best performance.

Table 4.3: Comparison of results using simple and crosspower spectrograms for the RCN and LSTM models. RCN predictions are made binary (0 and 1) using AE scores = 0.05, 0.15, 0.11, 0.07 and 0.08 for the five AEs listed in the left column. Similarly, the LSTM threshold values are 0.06, 0.13, 0.13, 0.10 and 0.07. The RCN trained using simple spectrograms is the top performer.

	SIMPLE				**CROSSPOWER**			
	RCN		**LSTM**		**RCN**		**LSTM**	
AE	**TPR**	**FPR**	**TPR**	**FPR**	**TPR**	**FPR**	**TPR**	**FPR**
EAE	0.60	0.07	0.77	0.07	0.72	0.07	0.70	0.06
TAE	0.93	0.18	0.94	0.26	0.89	0.14	0.94	0.28
RSAE	0.94	0.19	0.91	0.29	0.89	0.15	0.92	0.28
BAE	0.80	0.23	0.79	0.23	0.69	0.13	0.79	0.27
LFM	0.81	0.05	0.80	0.10	0.64	0.02	0.78	0.07
TOTAL	0.90	0.14	0.90	0.18	0.85	0.10	0.90	0.18

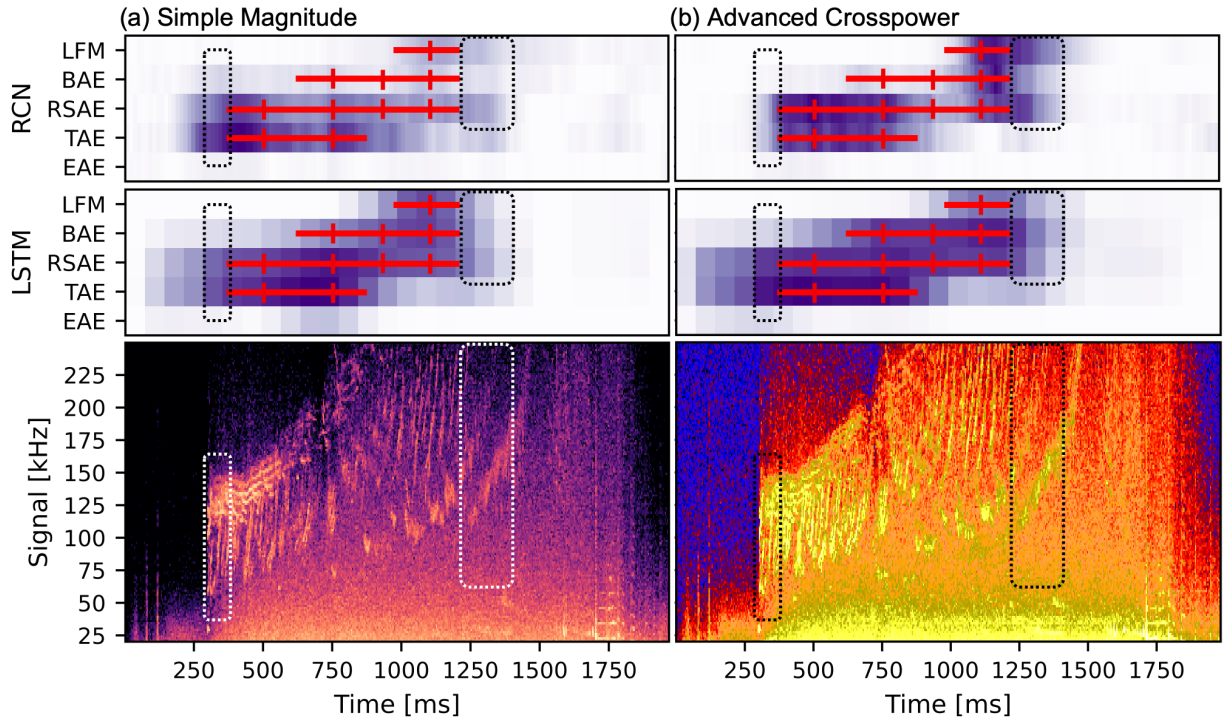

Figure 4.5: A comparison of the raw RCN and LSTM predictions using simple magnitude (panel a) and advanced crosspower (panel b) spectrograms for shot #178631. The simple spectrogram is calculated for chord V2 and the crosspower is between chords V2 and R0. The red vertical ticks and horizontal strikethroughs indicate the curated time stamp and label, respectively. The purple pixels are raw predictions for the RCN and LSTM models. Regions where the purple pixels overlap the red strikethroughs are considered good agreement. The dotted regions are times where the curated database doesn't indicate anything, yet the model is robust enough to capture the AE activity observed in the spectrograms.

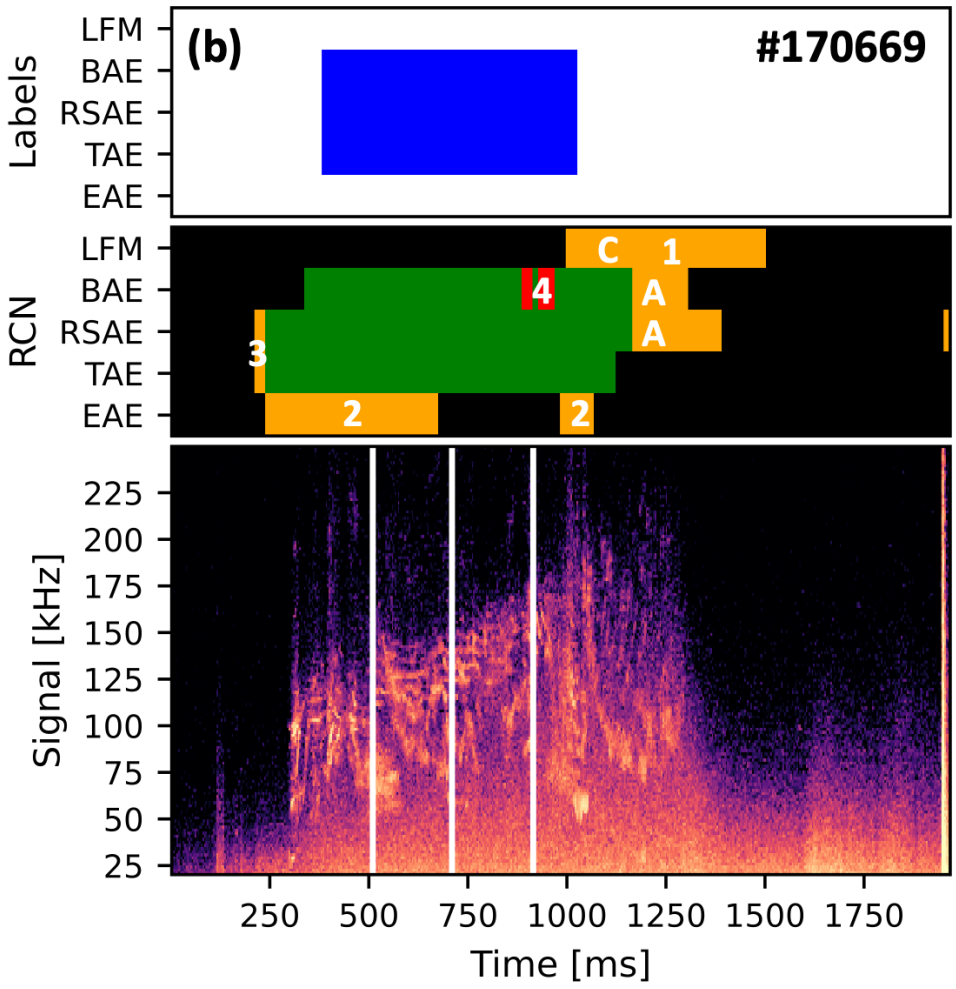

Figure 4.6: AE labels, thresholded predictions and simple magnitude spectrograms for shot #170669. The colored predictions are denoted as follows: TP = green, FP = orange, FN = red, and TP = black. White vertical lines in the spectrograms indicate the original timestamp. Error type 1 is due to effects from overfitting, since the model could be triggering scores for LFM due to the overall pattern of the discharge. Error type 2 occurs due to noise in the spectrograms. Error type 3 is attributed to time delays for predictions. Error type 4 is categorized as a general AI error, where the model failed to predict correctly. Letter A indicates an incorrectly assigned error since there is still activity but the Δt extension of the label is too short. Letter C also indicates an incorrectly assigned error due to ambiguity in the discharge.

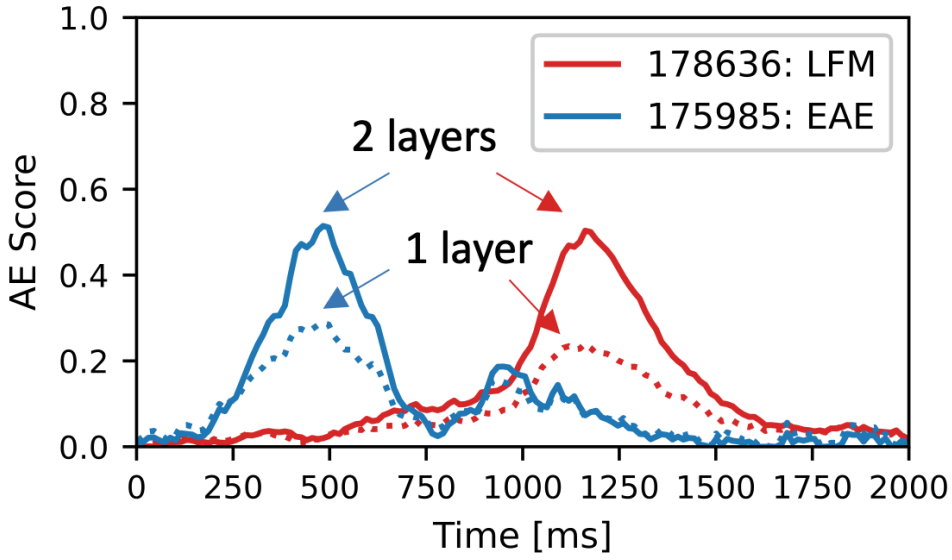

Figure 4.7: LFM and EAE predictions using the RCN model for shots 178636 and 175985 for CO_2 chord V2. A second reservoir recitifies the mistakes made by the first layer and produces better predictions for the least common modes in the database.

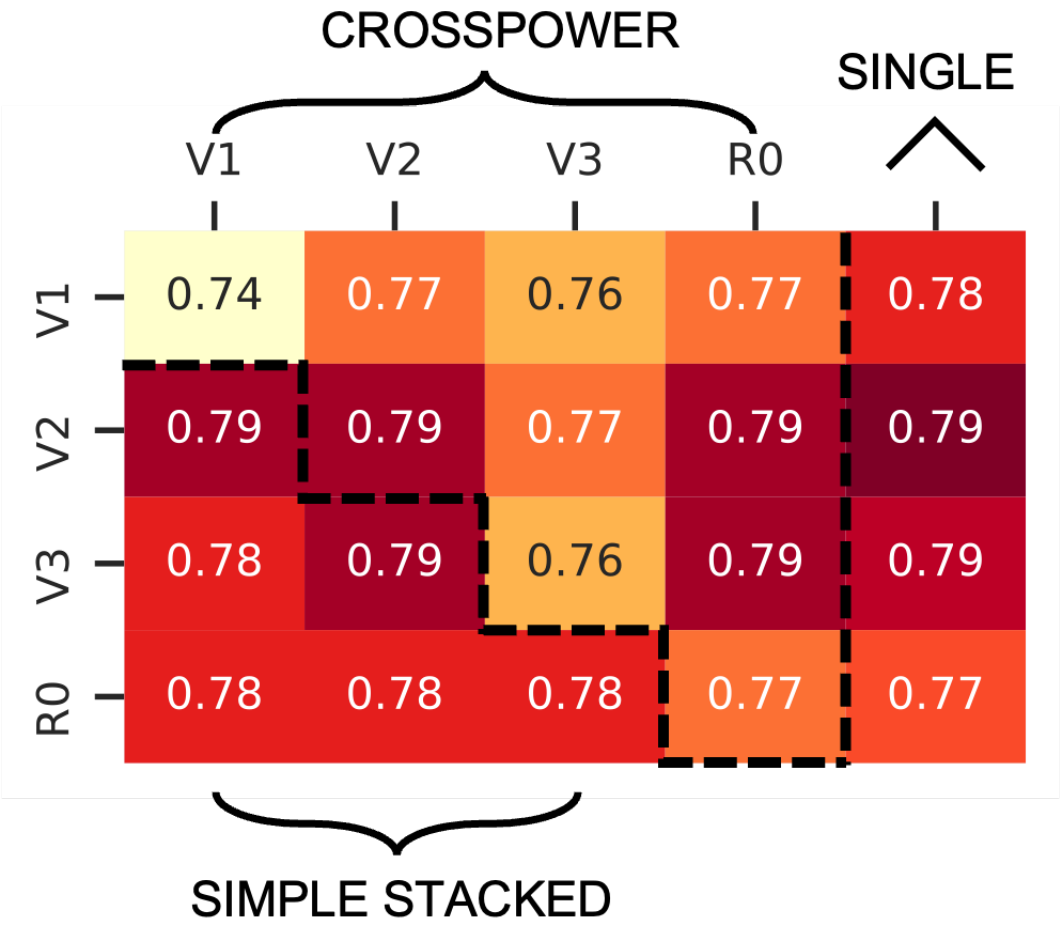

Figure 4.8: F2 scores for the crosspower (upper diagonal), stacked chords (lower diagonal) and single chord (right vertical bar) comparison using the RCN model. Stacking chords can perform better than crosspower, and chord V2 performs slightly better than the other three chords.

4.4 Analysis of metadata

Additional information in the Large AE-EP Database can be used to study model interpretability, and correlations between misclassification and operating regime parameters. The following inferred and experimental data data are available [119]: 1) EFIT equilibrium reconstructions [59] provide plasma shape, magnetic field, and beta information, 2) kinetic temperature, plasma rotation, and electron and impurity densities from between-shot profile fitting algorithms, and 3) information about neutral beams such as injected power, energy, voltage and orientation. The goal is to determine if there are any tendencies with misclassification by calculating Pearson correlation coefficients, r, between TPR and FPR with all 68 parameters in the database for the validation set.

Although many parameters have coefficient values near zero for both TPR and FPR, we report parameters with the highest values here. For the AE labels, BAE has the strongest Pearson correlation coefficient with values of -0.22 and -0.21 for TPR and FPR, respectively. For the plasma parameters, the strongest correlation for TPR is with pitch-angle-scattering (PAS) time on axis, and for FPR is with an analytical calculation of the BAE frequency; see Figure 4.9. The r for PAS with TPR and BAE frequency with FPR are 0.20 and -0.17, respectively. In both cases, there are about 500 points used in the comparison, and an $|r| \simeq 0.20$ indicates that the dependence is either non-existent or very weak. Thus, there is no evidence of any dependence on the operating regime—suggesting that we could safely use the identifier throughout this parameter range and likely somewhat beyond.

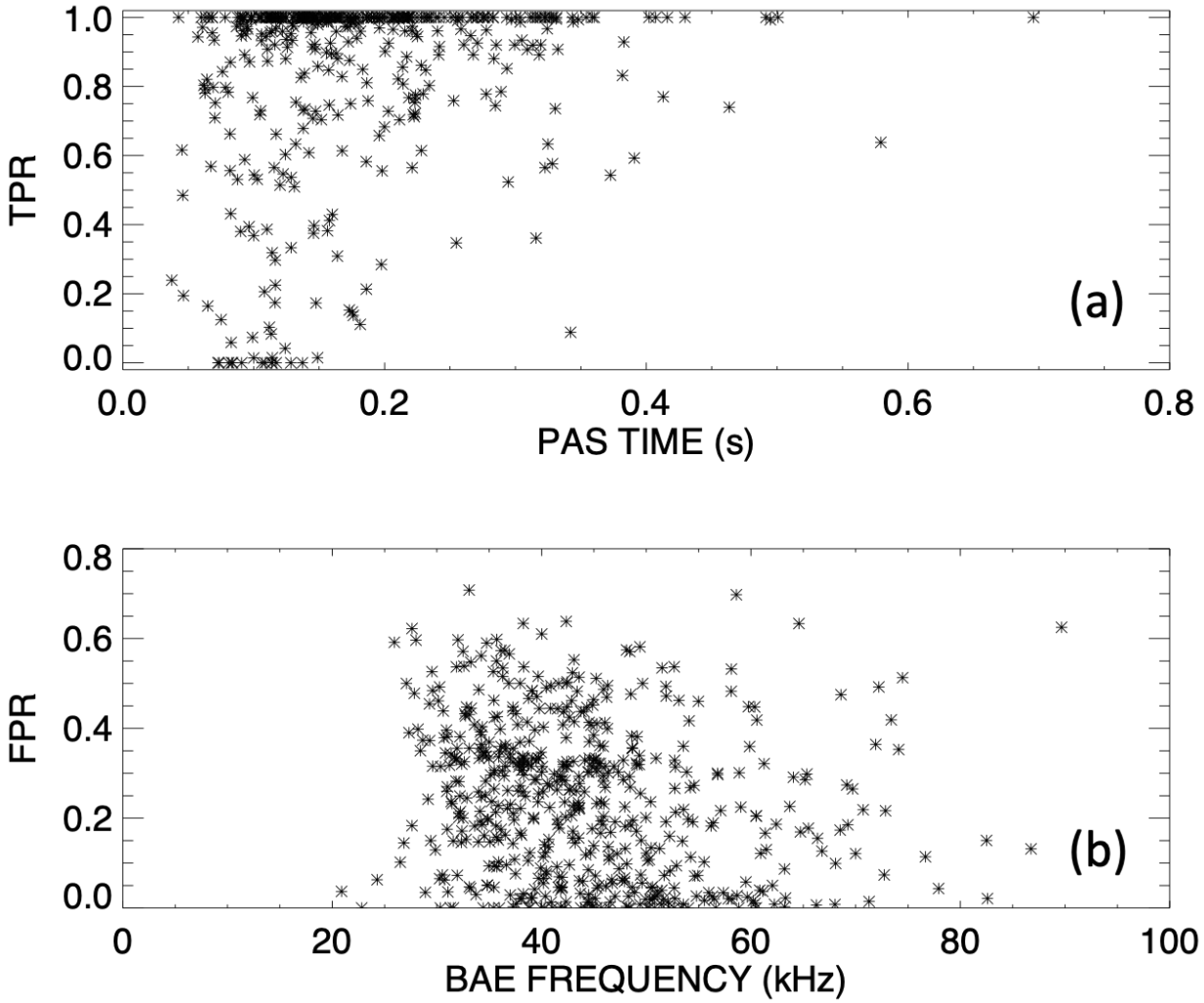

Figure 4.9: Points for the strongest Pearson correlation coefficient, r, in the comparison between AE metrics (TPR & FPR) and metadata are shown here. In panel a, the pitch-angle scattering (PAS) time is the 90-degree scattering time in the NRL Formulary [131]. The r between PAS and TPR is 0.20. In panel b, the BAE frequency is from Eq. (1) of [132], and the r with FPR is -0.17. Since most of the analysis shows low correlation values, concerns regarding the RCN model failing to predict AEs at the limits of the parameter range are alleviated.

4.5 Conclusion

Recurrent neural networks are trained using CO_2 interferometer data and labels from the Large AE-EP Database on the DIII-D tokamak. Two models (RCN and LSTM) are trained separately using simple and crosspower spectrograms. The additional steps required to calculate crosspower are unnecessary since the predictions are similar for both types of inputs. Both models are trained using one CO_2 chord per training step and achieve high results. The RCN performance is slightly higher with True Positive Rate = 90 % and False Positive Rate = 14 %. Detection using any single chord is feasible (V2 is slightly better than the other three). Since the model is primarily trained using labels marked during the current ramp phase, more cases labelling the steady-state portion of the discharge would improve generalizability. Lastly, analysis of the metadata demonstrates that the RCN model still works at the limits of the experimental parameter ranges.

The CO_2 Interferometer is commonly used in fluctuation analysis, acquires data for nearly every DIII-D experiment, is available in the Plasma Control System in real-time, and doesn't have issues with cutoff frequencies. Given these results and advantages, it is strongly recommended to detect AEs using RCNs trained with simple magnitude spectrograms calculated using the vertical chord passing near center ($R_m = 1.94\,\mathrm{m}$ at DIII-D).

Future work would consist of implementing the RCN reported in this chapter into real-time control algorithms to detect AEs at DIII-D. The state-of-the-art detector currently installed on the Plasma Control System is an RCN that trained using ECE data with 8000 and 500 nodes for Layer 1 and Layer 2, respectively. It processes time domain signals and makes predictions in approximately 400 microseconds for each time step. The RCN developed in this work is smaller for both layers (4000 and 50 nodes). Although there is an additional step of calculating spectrograms, the RCN trained using CO_2 Interferometer data could have a similar or faster response time during real-time experiments. Implementation of Fast Fourier

Transforms into the PCS is currently under consideration and we plan to test it in the near future.

Chapter 5

Conclusions and Outlook

This work produced novel computational methods to study topics in fast-ion physics. The first part developed 3 MeV proton weight functions verified using MAST-U data. The second part showed that accurate lifetime measurements of spin polarized fuel are feasible on DIII-D. The third part trained machine learning-based classifiers to identify Alfvén eigenmodes using CO_2 interferometer data and an expert labelled database on DIII-D. The following sections suggest possibilities for future work in these three areas.

5.1 Velocity-space tomography

Understanding fast ions born from fusion reactions is a goal for the worldwide energetic particle community since they can damage the first walls if unconfined and can provide the heating needed for an ignited burn via alpha self-heating [133]. Fast-ion diagnostics play an important role in this endeavor since they provide information about the plasma and facilitate better understanding of the fast-ion distribution function. Diagnostic velocity-space weight functions can be used to infer the fast-ion distribution function from experimental

measurements. Equation 2.1 can be discretized into matrix form as follows:

$$\mathbf{C} = \mathbf{W} \cdot \mathbf{F}, \tag{5.1}$$

where the rows of $\mathbf{W}$ consist of weight functions for each individual measurement and the elements of $\mathbf{F}$ are local "pixels" of the distribution function. Inverting this equation for $\mathbf{F}$ is a challenge since this is an over-determined system of equations with usually noisy diagnostic data. Several reconstruction methods exist in fusion energy research [134–141] and it would be interesting to apply a similar method implementing the 3 MeV proton weight functions developed in this work in combination with FIDA, neutron collimator, and NPA data.

5.2 Measure the lifetime of spin polarization

Spin polarized D-T fuel can increase the number of fusion reactions by 50% if the nuclear spins remain polarized in the same direction as the magnetic field. Measuring the lifetime of spin polarization is important for a successful spin polarization fusion program. Using the conclusions from this work, installation of charged fusion product detectors at DIII-D would be an exciting step forward towards this goal. Orbits detected at the wall can provide information about the emitted charged fusion product pitch angle near the core, where most of the fusion reactions take place. In this thesis, pitch-resolved measurements of 14.7 MeV protons at the -56° port, and an array of alpha flux detectors showed the strongest sensitivity to different polarization modes. A preliminary next step for SPF lifetime measurements would be to install 3-MeV proton detectors born from D-D reactions since detected orbits are similar to 3.6 MeV alphas. Since the 3-MeV proton diagnostic can easily be repurposed, successful D-D experiments can pave the way forward for CFP detection during SPF experiments at DIII-D. Additionally, the following challenges need to be addressed in the near future: 1) produce a high T_i scenario, 2) deposit pellets into the core, 3) define size of pellets,

and 4) determine timing of pellet injection.

5.3 Alfvén eigenmode prediction and control

Improving scientific understanding of the plasma state and steering it away from dangerous instabilities is an important goal for commercially viable fusion reactors. Data-driven models can provide real-time monitoring of the plasma in reactor relevant scenarios since they can be trained quickly, require a minimal set of physics information as input and can make predictions faster than the time scales of instabilities. The recurrent neural networks developed in this thesis are suitable options for these needs and they directly contribute to Priority Research Opportunity 4 in the Report on the Advancing Fusion with Machine Learning Research Needs Workshop [113].

Implementation of this CO_2 interferometer detector into the Plasma Control System in upcoming experiments at DIII-D would be the logical next step. Since global normalization of the CO_2 interferometer signals is a challenge using simple techniques, using 1D Convolutional Neural Networks (convnet) is a suitable candidate to eliminate the FFT preprocessing step. The filters of the convnets are theoretically capable of learning the frequency information directly from the signals with sufficient model capacity (deep layers and many nodes). Alternatively, implementing real-time Fourier transformation capabilities on several GPUs or FPGAs might be an easier option since this doesn't require additional neural network training. ECE signal streams can be integrated and parallelized with CO_2 interferometer data for multimodal machine learning. A feedback controller can use the outputs of this model for AE prediction and control in a reinforcement learning framework.

Bibliography

[1] W. W. Heidbrink et al., "Phase-space sensitivity (weight functions) of 3 MeV proton diagnostics", Plasma Physics and Controlled Fusion **63**, 055008 (2021).

[2] A. Garcia, W. Heidbrink, and A. M. Sandorfi, "Conceptual design of DIII-D experiments to diagnose the lifetime of spin polarized fuel", Nuclear Fusion **63**, 026030 (2023).

[3] A. V. Garcia et al., "Alfvén eigenmode detection using Long-Short Term Memory Networks and CO_2 Interferometer data on the DIII-D National Fusion Facility", in 2023 International Joint Conference on Neural Networks (IJCNN) (IEEE, 2023), pp. 1–8.

[4] A. Garcia et al., "Comparison of machine learning systems trained to detect Alfvén eigenmodes using the CO_2 interferometer on DIII-D", Nuclear Fusion (submitted 2023).

[5] S. Anand and A. Sen, "Human Development Index: Methodology and Measurement.", (1994).

[6] O. Rosling, A. R. Rönnlund, and H. Rosling, *Gapminder Tools*, `https://www.gapminder.org/tools/`, 2023.

[7] Wikipedia, *Nuclear binding energy — Wikipedia, The Free Encyclopedia*, `https://en.wikipedia.org/wiki/Nuclear_binding_energy`, 2023.

[8] J. Wesson and D. J. Campbell, *Tokamaks*, Vol. 149 (Oxford university press, 2011).

[9] *Achieving fusion ignition*, https://lasers.llnl.gov/science/pursuit-of-ignition, 2023.

[10] A. Horvath and E. Rachlew, "Nuclear power in the 21st century: Challenges and possibilities", Ambio **45**, 38–49 (2016).

[11] H. Bosch and G. Hale, "Improved formulas for fusion cross-sections and thermal reactivities", Nuclear Fusion **32**, 611 (1992).

[12] V. Smirnov, "Tokamak foundation in USSR/Russia 1950–1990", Nuclear fusion **50**, 014003 (2009).

[13] J. Menard et al., "Fusion nuclear science facilities and pilot plants based on the spherical tokamak", Nuclear Fusion **56**, 106023 (2016).

[14] B. van Milligen, *Toroidal coordinates*, http://fusionwiki.ciemat.es/wiki/File:Toroidal_coordinates.png, 2009.

[15] Y. Li, "Thermo-mechanical behavior of tungsten under fusion-relevant hydrogen plasma loads", (2021).

[16] E. ITER et al., "Physics of energetic ions", Nuclear Fusion **39**, 2471–2494 (1999).

[17] M. Garcia-Munoz et al., "Active control of Alfvén eigenmodes in magnetically confined toroidal plasmas", Plasma Physics and Controlled Fusion **61**, 054007 (2019).

[18] D. C. Pace et al., "Control of power, torque, and instability drive using in-shot variable neutral beam energy in tokamaks", en, Nuclear Fusion **57**, 014001 (2016).

[19] P. Li et al., "Dynamics between toroidal Alfvén eigenmode evolution and turbulence suppression under RMP on EAST", Nuclear Fusion (2021).

[20] S. Tang et al., "Stabilization of Alfvén Eigenmodes in DIII-D via Controlled Energetic Ion Density Ramp and Validation of Theory and Simulations", Physical Review Letters **126**, 155001 (2021).

[21] T. Evans, "Implications of topological complexity and Hamiltonian chaos in the edge magnetic field of toroidal fusion plasmas", in *Chaos, Complexity and Transport: Theory and Applications* (World Scientific, 2008), pp. 147–176.

[22] W. Heidbrink and G. Sadler, "The behaviour of fast ions in tokamak experiments", Nuclear Fusion **34**, 535 (1994).

[23] W. W. Heidbrink, "Basic physics of Alfvén instabilities driven by energetic particles in toroidally confined plasmas", Physics of Plasmas **15**, 055501 (2008).

[24] W. W. Heidbrink et al., "Confinement degradation by Alfvén-eigenmode induced fast-ion transport in steady-state scenario discharges", Plasma Physics and Controlled Fusion **56**, 095030 (2014).

[25] C. T. Holcomb et al., "Fast-ion transport in $q_{min} > 2$, high-β steady-state scenarios on DIII-D", Physics of Plasmas **22**, 055904 (2015).

[26] H. Berk, B. Breizman, and H. Ye, "Scenarios for the nonlinear evolution of alpha-particle-induced Alfvén wave instability", Physical review letters **68**, 3563 (1992).

[27] R. White et al., "Particle distribution modification by low amplitude modes", Plasma Physics and Controlled Fusion **52**, 045012 (2010).

[28] A. U. Team et al., "Convective and diffusive energetic particle losses induced by Shear Alfvén waves in the ASDEX Upgrade tokamak", Physical Review Letters **104**, 185002 (2010).

[29] D. Sigmar et al., "Alpha-particle losses from toroidicity-induced Alfvén eigenmodes. Part II: Monte Carlo simulations and anomalous alpha-loss processes", Physics of Fluids B: Plasma Physics **4**, 1506–1516 (1992).

[30] L. Appel et al., "Alfvén eigenmode induced energetic particle transport in JET", Nuclear fusion **35**, 1697 (1995).

[31] W. Hu et al., "Active real-time control of Alfvén eigenmodes by neutral beam and electron cyclotron heating in the DIII-D tokamak", Nuclear Fusion **58**, 124001 (2018).

[32] T. Kurki-Suonio et al., "ASCOT simulations of fast ion power loads to the plasma-facing components in ITER", Nuclear Fusion **49**, 095001 (2009).

[33] B. Geiger et al., "Progress in modelling fast-ion D-alpha spectra and neutral particle analyzer fluxes using FIDASIM", Plasma Physics and Controlled Fusion **62**, 105008 (2020).

[34] L. Stagner, B. Geiger, and W. Heidbrink, *FIDASIM: A Neutral Beam and Fast-ion Diagnostic Modeling Suite*, `https://doi.org/10.5281/zenodo.1341369`, 2023.

[35] L. Stagner, B. Geiger, and W. Heidbrink, *FIDASIM*, `http://d3denergetic.github.io/FIDASIM/master/page/index.html`, 2023.

[36] M. Salewski et al., "Bayesian integrated data analysis of fast-ion measurements by velocity-space tomography", Fusion science and technology **74**, 23–36 (2018).

[37] W. W. Heidbrink et al., "Measurements of fast-ion acceleration at cyclotron harmonics using Balmer-alpha spectroscopy", Plasma Physics and Controlled Fusion **49**, 1457–1475 (2007).

[38] M. Salewski et al., "On velocity-space sensitivity of fast-ion D-alpha spectroscopy", Plasma Physics and Controlled Fusion **56**, 105005 (2014).

[39] L. Stagner and W. W. Heidbrink, "Action-angle formulation of generalized, orbit-based, fast-ion diagnostic weight functions", Physics of Plasmas **24**, 092505 (2017).

[40] M. Salewski et al., "On velocity space interrogation regions of fast-ion collective Thomson scattering at ITER", Nuclear Fusion **51**, 083014 (2011).

[41] X. Du et al., "Resolving the fast ion distribution from imaging neutral particle analyzer measurements", Nuclear Fusion **60**, 112001 (2020).

[42] A. Jacobsen et al., "Velocity-space sensitivity of neutron spectrometry measurements", Nuclear Fusion **55**, 053013 (2015).

[43] A. Jacobsen et al., "Velocity-space sensitivities of neutron emission spectrometers at the tokamaks JET and ASDEX Upgrade in deuterium plasmas", Review of Scientific Instruments **88**, 073506 (2017).

[44] A. Sperduti et al., "Velocity-space sensitivity of the neutron camera on MAST", Journal of Instrumentation **14**, C09005–C09005 (2019).

[45] M. Salewski et al., "Velocity-space observation regions of high-resolution two-step reaction gamma-ray spectroscopy", Nuclear Fusion **55**, 093029 (2015).

[46] M. Salewski et al., "Fast-ion energy resolution by one-step reaction gamma-ray spectrometry", Nuclear Fusion **56**, 046009 (2016).

[47] J. Galdon-Quiroga et al., "Velocity-space sensitivity and tomography of scintillator-based fast-ion loss detectors", Plasma Physics and Controlled Fusion **60**, 105005 (2018).

[48] R. Perez et al., "Investigating fusion plasma instabilities in the Mega Amp Spherical Tokamak using mega electron volt proton emissions", Review of Scientific Instruments **85**, 11D701 (2014).

[49] W. Heidbrink et al., "Fast ion profiles during neutral beam and lower hybrid heating", Plasma physics and controlled fusion **28**, 871 (1986).

[50] A. Netepenko et al., "Plasma diagnostics in spherical tokamaks with silicon charged-particle detectors", Review of Scientific Instruments **87**, 11D805 (2016).

[51] D. Liu et al., "Effect of sawtooth crashes on fast ion distribution in NSTX-U", Nuclear Fusion **58**, 082028 (2018).

[52] M. Cecconello et al., "Energetic ion behaviour in MAST", Plasma Physics and Controlled Fusion **57**, 014006 (2015).

[53] W. Heidbrink and J. Strachan, "Tokamak ion temperature and poloidal field diagnostics using 3-MeV protons", Review of scientific instruments **56**, 501–518 (1985).

[54] H. Vogel, "A better way to construct the sunflower head", Mathematical biosciences **44**, 179–189 (1979).

[55] H. Brysk, "Fusion neutron energies and spectra", Plasma Physics **15**, 611–617 (1973).

[56] R. E. Brown and N. Jarmie, "Differential cross sections at low energies for $^2\mathrm{H}(d,p)^{\mathrm{H}}$ and $^2\mathrm{H}(d,n)^3\mathrm{He}$", Physical Review C **41**, 1391–1400 (1990).

[57] L. Stagner, B. Geiger, and W. Heidbrink, *D3DEnergetic/FIDASIM: A Neutral Beam and Fast-ion Diagnostic Modeling Suite*, `https://github.com/D3DEnergetic/FIDASIM`, 2023.

[58] E. V. Belova, N. N. Gorelenkov, and C. Z. Cheng, "Self-consistent equilibrium model of low aspect-ratio toroidal plasma with energetic beam ions", Physics of Plasmas **10**, 3240–3251 (2003).

[59] L. Lao et al., "Reconstruction of current profile parameters and plasma shapes in tokamaks", Nuclear Fusion **25**, 1611 (1985).

[60] J. Breslau et al., *TRANSP*, `https://doi.org/10.11578/dc.20180627.4`, 2018.

[61] W. Heidbrink, "Energy spectra from "beam-target" nuclear reactions in magnetic fusion devices", Nuclear Instruments and Methods in Physics Research Section A: Accelerators, Spectrometers, Detectors and Associated Equipment **236**, 380–384 (1985).

[62] R. Chrien, R. Kaita, and J. Strachan, "Observation of $d(d,p)T$ reactions in the Princeton Large Torus", Nuclear fusion **23**, 1399 (1983).

[63] R. Kulsrud, E. Valeo, and S. Cowley, "Physics of spin-polarized plasmas", Nuclear Fusion **26**, 1443–1462 (1986).

[64] R. M. Kulsrud et al., "Fusion Reactor Plasmas with Polarized Nuclei", Physical Review Letters **49**, 1248–1251 (1982).

[65] S. P. Smith, "The Potential For Retention of Spin Polarization To Raise Fusion Reactivity", 27th IAEA Fusion Energy Conference, 7 (2018).

[66] G. Ciullo et al., eds., *Nuclear Fusion with Polarized Fuel*, Vol. 187, Springer Proceedings in Physics (Springer International Publishing, Cham, 2016).

[67] A. M. Sandorfi et al., "Polarized fusion, its Implications and plans for Direct Measurements in a Tokamak", arXiv:1703.06165 [physics] (2017).

[68] S. J. Zweben, "Pitch angle resolved measurements of escaping charged fusion products in TFTR", Nuclear Fusion **29**, 825–833 (1989).

[69] W. W. Heidbrink, "Fusion reaction spectra produced by anisotropic$\less$sup$\greater$3$\less$/sup ions during ICRF", Nuclear Fusion **24**, 636–639 (1984).

[70] S. J. Zweben et al., "Loss of alpha-like MeV fusion products from TFTR", Nuclear Fusion **30**, 1551–1574 (1990).

[71] A. Sandorfi et al., "Polarized Fusion and Potential in situ Tests of Fuel Polarization Survival in a Tokamak Plasma", Nuclear Fusion **62**, Submitted (2022).

[72] K. H. Burrell et al., "Effects of velocity shear and magnetic shear in the formation of core transport barriers in the DIII-D tokamak", Plasma Physics and Controlled Fusion **40**, 1585–1596 (1998).

[73] D. Schissel et al., "Energy confinement properties of H-mode discharges in the DIII-D tokamak", Nuclear Fusion **29**, 185 (1989).

[74] W. W. Heidbrink and J. D. Strachan, "Tokamak ion temperature and poloidal field diagnostics using 3-MeV protons", Review of Scientific Instruments, 19 (1985).

[75] R. K. Fisher et al., "Scintillator-based diagnostic for fast ion loss measurements on DIII-D", Review of Scientific Instruments **81**, 10D307 (2010).

[76] A. Bortolon et al., "High frequency pacing of edge localized modes by injection of lithium granules in DIII-D H-mode discharges", Nuclear Fusion **56**, 056008 (2016).

[77] C. Spitaleri et al., "Indirect ^{7}Li$(p,\alpha)^{4}$He reaction at astrophysical energies", Physical Review C **60**, 055802 (1999).

[78] P. Gohil et al., "high spatial and temporal resolution visible spectroscopy of the plasma edge in DIII-D", **61**, 2949 (1990).

[79] S. Haskey et al., "Radially resolved active charge exchange measurements of the hydrogenic isotope fraction on DIII-D", Review of Scientific Instruments **92**, 043535 (2021).

[80] F. Cecil et al., "Reaction ^{2}H$(^{3}$He$,\gamma)^{5}$Li at center-of-mass energies between 25 and 60 keV", Physical Review C **32**, 690 (1985).

[81] V. Kiptily et al., "γ-ray diagnostics of energetic ions in JET", Nuclear Fusion **42**, 999 (2002).

[82] W. Buss et al., "Deuteron capture in ^{3}He", Nuclear Physics A **112**, 47–64 (1968).

[83] M. Iliasova et al., "Gamma-ray measurements in D3He fusion plasma experiments on JET", Nuclear Instruments and Methods in Physics Research Section A: Accelerators, Spectrometers, Detectors and Associated Equipment **1031**, 166586 (2022).

[84] V. Kiptily, F. Cecil, and S. Medley, "Gamma ray diagnostics of high temperature magnetically confined fusion plasmas", Plasma physics and controlled fusion **48**, R59 (2006).

[85] A. Nikroo et al., "Recent Progress in Fabrication of High-Strength Glow Discharge Polymer Shells by Optimization of Coating Parameters", Fusion Science and Technology **41**, 214–219 (2002).

[86] E. M. Hollmann et al., "Low-Z Shell Pellet Experiments on DIII-D", AIP Conference Proceedings **1161**, 65–74 (2009).

[87] L. R. Baylor et al., "Improved core fueling with high field side pellet injection in the DIII-D tokamak", Physics of Plasmas **7**, 1878–1885 (2000).

[88] C. Angioni et al., "Particle transport in tokamak plasmas, theory and experiment", Plasma Physics and Controlled Fusion **51**, 124017 (2009).

[89] J. D. Strachan and A. Chan, "Helium transport in TFTR", Nuclear Fusion **27**, 1025–1029 (1987).

[90] X. D. Du et al., "Multiscale Chirping Modes Driven by Thermal Ions in a Plasma with Reactor-Relevant Ion Temperature", Physical Review Letters **127**, 025001 (2021).

[91] W. W. Heidbrink, R. E. Chrien, and J. D. Strachan, "Burn-up of fusion-produced tritons {$ˆ3\mbox{He}$} ions in PLT and PDX", Nuclear Fusion **23**, 917–931 (1983).

[92] R. A. Causey, "Hydrogen isotope retention and recycling in fusion reactor plasma-facing components", Journal of Nuclear Materials **300**, 91–117 (2002).

[93] H. S. Greenside, R. V. Budny, and D. E. Post, "Depolarization of D–T plasmas by recycling in material walls", Journal of Vacuum Science & Technology A **2**, 619–629 (1984).

[94] M. A. Abdou et al., "Deuterium-Tritium Fuel Self-Sufficiency in Fusion Reactors", Fusion Technology **9**, 250–285 (1986).

[95] T. H. Stix, "Fast-wave heating of a two-component plasma", Nuclear Fusion **15**, 737 (1975).

[96] R. Chrien and J. Strachan, "d-^{3}He reaction measurements during fast wave minority heating in the PLT tokamak experiment", The Physics of fluids **26**, 1953–1964 (1983).

[97] S. D. Pinches et al., "The role of energetic particles in fusion plasmas", Plasma Physics and Controlled Fusion **46**, B187–B200 (2004).

[98] H. Duong et al., "Loss of energetic beam ions during TAE instabilities", Nuclear Fusion **33**, 749 (1993).

[99] R. White et al., "Toroidal Alfvén eigenmode-induced ripple trapping", Physics of Plasmas **2**, 2871–2873 (1995).

[100] N. N. Gorelenkov, S. Pinches, and K. Toi, "Energetic particle physics in fusion research in preparation for burning plasma experiments", Nuclear Fusion **54**, 125001 (2014).

[101] L. Chen and F. Zonca, "Physics of Alfvén waves and energetic particles in burning plasmas", Reviews of Modern Physics **88**, 015008 (2016).

[102] Y. Todo, "Introduction to the interaction between energetic particles and Alfvén eigenmodes in toroidal plasmas", Reviews of Modern Plasma Physics **3**, 1–33 (2019).

[103] J. Snipes et al., "MHD and Plasma Control in ITER", Fusion Science and Technology **59**, 427–439 (2011).

[104] J. Snipes et al., "Physics of the conceptual design of the ITER plasma control system", Fusion Engineering and Design **89**, 507–511 (2014).

[105] C. Rea and R. S. Granetz, "Exploratory Machine Learning Studies for Disruption Prediction Using Large Databases on DIII-D", Fusion Science and Technology **74**, 89–100 (2018).

[106] Y. Fu et al., "Machine learning control for disruption and tearing mode avoidance", Physics of Plasmas **27**, 022501 (2020).

[107] B. Cannas et al., "Automatic disruption classification in JET with the ITER-like wall", Plasma Physics and Controlled Fusion **57**, 125003 (2015).

[108] C. Rea et al., "Disruption prediction investigations using Machine Learning tools on DIII-D and Alcator C-Mod", Plasma Physics and Controlled Fusion **60**, 084004 (2018).

[109] A. Murari et al., "Adaptive predictors based on probabilistic SVM for real time disruption mitigation on JET", Nuclear Fusion **58**, 056002 (2018).

[110] J. Kates-Harbeck, A. Svyatkovskiy, and W. Tang, "Predicting disruptive instabilities in controlled fusion plasmas through deep learning", Nature **568**, 526–531 (2019).

[111] E. Aymerich et al., "Disruption prediction at JET through deep convolutional neural networks using spatiotemporal information from plasma profiles", Nuclear Fusion **62**, 066005 (2022).

[112] K. J. Montes et al., "Machine learning for disruption warnings on Alcator C-Mod, DIII-D, and EAST", Nuclear Fusion **59**, 096015 (2019).

[113] D. Humphreys et al., "Advancing Fusion with Machine Learning Research Needs Workshop Report", Journal of Fusion Energy **39**, 123–155 (2020).

[114] A. Bustos et al., "Automatic identification of MHD modes in magnetic fluctuation spectrograms using deep learning techniques", Plasma Physics and Controlled Fusion **63**, 095001 (2021).

[115] V. Škvára et al., "Detection of Alfvén Eigenmodes on COMPASS with Generative Neural Networks", Fusion Science and Technology **76**, 962–971 (2020).

[116] B. J. Q. Woods et al., "Machine Learning Characterization of Alfvénic and Sub-Alfvénic Chirping and Correlation With Fast-Ion Loss at NSTX", IEEE Transactions on Plasma Science **48**, 71–81 (2020).

[117] S. Haskey, B. Blackwell, and D. Pretty, "Clustering of periodic multichannel timeseries data with application to plasma fluctuations", Computer Physics Communications **185**, 1669–1680 (2014).

[118] S. Haskey et al., "Experiment-theory comparison for low frequency BAE modes in the strongly shaped H-1NF stellarator", Plasma Physics and Controlled Fusion **57**, 095011 (2015).

[119] W. W. Heidbrink et al., "'BAAE'instabilities observed without fast ion drive", Nuclear Fusion **61**, 016029 (2020).

[120] A. Jalalvand et al., "Alfvén eigenmode classification based on ECE diagnostics at DIII-D using deep recurrent neural networks", Nuclear Fusion **62**, 026007 (2022).

[121] A. A. Kaptanoglu et al., "Exploring data-driven models for spatiotemporally local classification of Alfvén eigenmodes", Nuclear Fusion (2022).

[122] M. Austin and J. Lohr, "Electron cyclotron emission radiometer upgrade on the DIII-D tokamak", Review of scientific instruments **74**, 1457–1459 (2003).

[123] M. Van Zeeland et al., "Alfvén eigenmode observations on DIII-D via two-colour CO2 interferometry", Plasma Physics and Controlled Fusion **47**, L31 (2005).

[124] G. McKee et al., "The beam emission spectroscopy diagnostic on the DIII-D tokamak", Review of scientific instruments **70**, 913–916 (1999).

[125] J. D. King et al., "An upgrade of the magnetic diagnostic system of the DIII-D tokamak for non-axisymmetric measurements", Review of Scientific Instruments **85**, 083503 (2014).

[126] P. Steiner et al., "PyRCN: A toolbox for exploration and application of Reservoir Computing Networks", Engineering Applications of Artificial Intelligence **113**, 104964 (2022).

[127] H. Jaeger, *The "echo state" approach to analysing and training recurrent neural networks*, tech. rep. GMD Report 148 (German National Research Center for Information Technology, 2001).

[128] P. Steiner et al., "Multipitch tracking in music signals using echo state networks", in 2020 28th European Signal Processing Conference (EUSIPCO) (IEEE, 2021), pp. 126–130.

[129] F. Triefenbach et al., "Phoneme recognition with large hierarchical reservoirs", Advances in neural information processing systems **23** (2010).

[130] A. Jalalvand et al., "Radar Signal Processing for Human Identification by Means of Reservoir Computing Networks", in IEEE Radar Conference (RadarConf) (2019), pp. 1–6.

[131] A. S. Richardson, *2019 NRL plasma formulary*, tech. rep. (US Naval Research Laboratory, 2019).

[132] W. Heidbrink et al., "Isotope dependence of beta-induced Alfvén eigenmode (BAE) and low frequency mode (LFM) stability in DIII-D", Nuclear Fusion **61**, 106021 (2021).

[133] J. Ongena et al., "Magnetic-confinement fusion", Nature Physics **12**, 398–410 (2016).

[134] Y. Nagayama et al., "Soft x-ray tomography of the m= 2 magnetic island structure in the JIPP T-II Tokamak", Japanese Journal of Applied Physics **20**, L779 (1981).

[135] R. Koslover and R. McWilliams, "Measurement of multidimensional ion velocity distributions by optical tomography", Review of scientific instruments **57**, 2441–2448 (1986).

[136] R. McWilliams and R. Koslover, "Laboratory observation of ion conics by velocity-space tomography of a plasma", Physical review letters **58**, 37 (1987).

[137] C. Reinhold, R. Olson, and W. Fritsch, "Excitation of atomic hydrogen by fully stripped ions", Physical Review A **41**, 4837 (1990).

[138] M. Anton et al., "X-ray tomography on the TCV tokamak", Plasma physics and controlled fusion **38**, 1849 (1996).

[139] D. C. Zimmerman, R. McWilliams, and D. A. Edrich, "Two-dimensional ion velocity distribution functions in inductively coupled argon plasma", Plasma Sources Science and Technology **14**, 581 (2005).

[140] J. Svensson, A. Werner, J.-E. Contributors, et al., "Current tomography for axisymmetric plasmas", Plasma Physics and Controlled Fusion **50**, 085002 (2008).

[141] M. Odstrcil et al., "Modern numerical methods for plasma tomography optimisation", Nuclear Instruments and Methods in Physics Research Section A: Accelerators, Spectrometers, Detectors and Associated Equipment **686**, 156–161 (2012).

[142] M. Van Zeeland et al., "Measurements and modeling of Alfvén eigenmode induced fast ion transport and loss in DIII-D and ASDEX Upgrade", Physics of Plasmas **18**, 056114 (2011).

Appendix A

Numerical methods to calculate thermonuclear signals

Equation 3.5 states that the CFP countrate C is $C(E_3) = \iiint dl\, dA\, d\Omega\, S(\mathbf{r}, \mathbf{v}_3)$, where dl is over the sightline trajectory, dA is over the detector area, dΩ is over the solid angle accepted by the detector collimating structure, and $S(\mathbf{r}, \mathbf{v}_3)$ represents the D-^{3}He emissivity (in reactions/volume-time) of CFPs that are emitted at position $\mathbf{r}$ along the sightline with the correct values of detected energy E_3 and solid angle Ω. This appendix sketches the methods used in the calculations of subsection 3.2.1 and section 3.4.

EFIT [59] is used to reconstruct the equilibrium, so the axisymmetric magnetic field $\mathbf{B}$ is known on a cylindrical (R, z) grid. CFP orbits are computed by integrating the Lorentz force law $d\mathbf{v}/dt = q\mathbf{v} \times \mathbf{B}$ using the Adams-Bashford-Moulton method. Since the orbit is followed in reverse, the "initial" conditions for the calculation is actually the position and velocity of the CFP at the detector $(\mathbf{r}, \mathbf{v})$. The $(\mathbf{r}, \mathbf{v})$ coordinates of the orbit is stored in 1 cm steps. The guiding center orbit calculated using the code described in the Appendix of [142] is used to ensure that orbits correctly terminate when they reapproach the wall.

The emissivity profile S is a function of the flux coordinate ρ, the square root of the normalized toroidal flux. To compute $\int S\,dl$, the equilibrium reconstruction is used to map orbital spatial positions into ρ, then S is inferred through interpolation. The local pitch $\cos\theta$ needed for evaluation of the differential cross section in Equation 3.1 is computed at each step from $\mathbf{v}\cdot\mathbf{B}/vB$. The values of $\int S\,dl$ plotted in subsection 3.2.1 are actually $\sum S(\mathbf{r})\,d\sigma/d\Omega(\mathbf{v})\,\Delta l$ summed over the orbit.

In the evaluations of actual signal levels in section 3.4, greater care of the $\iint dA\,d\Omega$ term is required, since a realistic detector samples a range of orbits. Since the detector area is small compared to the orbit size, the approximation [74]

$$\int\int dA\,d\Omega \simeq A\int T(\Omega)\,d\Omega \tag{A.1}$$

is used, where $T(\Omega)$ is a transmission factor that depends upon the angle of the orbit at the aperture. Here, we assume rectangular apertures oriented to select gyroradius and pitch. Since the 14.7 MeV proton trajectory is sensitive to initial gyroangle, a 5×5 gyroangle-pitch grid is used in Figure 3.13. For alpha flux, the orbits are insensitive to initial gyroangle but very sensitive to initial pitch, so a large number of initial pitch values (e.g., 81) are used for the calculations shown in Figure 3.14.

Appendix B

Generalization of p_{gyro}

The goal is to generalize the factor that considers the number of fast ions in velocity space that can produce a reaction with the specified value of v_3 for any general CFP. Generalization of p_{gyro} follows Section 4.2 of [1] and important parts of the derivation are described here. Masses, m_i, in the equations of energy and momentum conservation in the lab frame are left general. Using the coordinate system described in the paper, v_1, v_2 and v_3 are inserted into the conservation equations and yields the following

$$\begin{aligned} v_\perp \left(2\mu_1 \sin\phi - \frac{\mu_1\mu_2}{\mu_3}\frac{2v_a}{v_3}\right)\cos\gamma = (1+\mu_3)v_3 - \frac{q}{\mu_3 v_3} - (2\mu_1 v_\parallel + 2\mu_2 v_b)\cos\phi \\ - 2\mu_2 v_a \sin\phi + \frac{(\mu_1^2-\mu_1)v_1^2}{\mu_3 v_3} + \frac{(\mu_2^2-\mu_2)v_2^2}{\mu_3 v_3} \\ + \frac{2\mu_1\mu_2}{\mu_3 v_3}(v_b v_\parallel + v_c v_\perp \sin\gamma) \end{aligned} \tag{B.1}$$

where $\mu_i = m_i/m_4$ and $q = 2Q/m_4$.

To get a general p_{gyro} factor, we want to calculate a pair of gyroangles γ for two energies $E_{3,high}$ and $E_{3,low}$; we are interested in the velocity-space spread of fast-ion gyroangles that produce protons in a specified energy bin ΔE_{bin}. Equation B.1 is used to determine γ_{high}

for $E_{3,high} = E_3 + \Delta E_{bin}/2$ and γ_{low} for $E_{3,low} = E_3 - \Delta E_{bin}/2$. The gyroradius probability factor is $p_{gyro} \simeq |\gamma_{high} - \gamma_{low}|/\pi$.

An issue in calculating Equation B.1 occurs when an energy bin extends beyond the permissible values of E_3 that are compatible with the other selected parameters. To find the permissible regime, the maximum and minimum values of E_3 are found from Equation B.1 when $\cos\gamma \simeq \pm 1$. Using the quadratic formula to find the extreme values of v_3 yields

$$v_3 = \frac{-B + \sqrt{B^2 - 4AC}}{2A} \tag{B.2}$$

where A, B and C are defined as

$$A = 1 + \mu_3$$

$$B = 2\mu_1(\mp v_\perp \sin\phi - v_\parallel \cos\phi) - 2\mu_2(v_b \cos\phi + v_a \sin\phi)$$

$$C = -\frac{1}{\mu_3}\left[q - (\mu_1^2 - \mu_1)v_1^2 - (\mu_2^2 - \mu_2)v_2^2 - 2\mu_1\mu_2(v_b v_\parallel \mp v_\perp v_a)\right]$$

Appendix C

Calculate CFP signals in FIDASIM

The preprocessing and main algorithm for the charged fusion product diagnostic calculations within the FIDASIM framework are outlined here. The CFPD table is prepared in the pre-fida step and merged with the usual FIDASIM inputs. This part of the algorithm is written in IDL and an example for α detection at pitch = 0.6 is shown below.

```
;Inputs
result_dir = '/home/results/'
inputs_dir = '/home/inputs/'
tables_dir = '/home/tables/'
transp_file = inputs_dir+'132224H02.CDF'

current_fractions = double([0.52811315, 0.26870434, 0.20318251])
basic_inputs = {device:"DIII-D",$
                einj:72.5,pinj:1.7,current_fractions:current_fractions,$
                lambdamin:647.0d0,lambdamax:667.0d0,nlambda:2000,$
                n_fida:5000000L,n_npa:5000000L,n_nbi:50000L, $
                n_pfida:50000000L,n_pnpa:50000000L,lambdamax_wght:667.d0,$
                n_halo:500000L,n_dcx:500000L,n_birth:10000L,$
```

```
                ne_wght:50,np_wght:50,nphi_wght:100,emax_wght:100.0d0,$
                nlambda_wght:1000,lambdamin_wght:647.d0,$
                calc_npa:0,calc_brems:0,calc_fida:0,calc_neutron:0,$
                calc_bes:0,calc_dcx:0,calc_halo:0,calc_cold:0,$
                calc_fida_wght:0,calc_npa_wght:0,calc_pfida:0,$
                adaptive:0,split_tol:0.d0,max_cell_splits:1,$
                calc_cfpd:3,calc_birth:0,calc_pnpa:0,$
                result_dir:result_dir,$
                tables_file:tables_dir+'atomic_tables.h5'}

;Beam grid
basic_bgrid = {nx:70,ny:50,nz:100,$
               xmin:100.d0,xmax:240.d0,$
               ymin:-50.d0,ymax:50.d0,$
               zmin:-100.d0,zmax:100.d0,$
               alpha:0.d0,beta:0.d0,gamma:0.d0,$
               origin:[0.d0,0.d0,0.d0]}

;Beam (needed to get prefida to run, but not used in cfpd algo)
nbi = test_beam(0.d0)

;Grid
g = readg(inputs_dir+'g132224.02005')
rmin = min(g.r)*0.95d0*100.d0
zmin = min(g.z)*1.05d0*100.d0
rmax = max(g.r)*1.05d0*100.d0
zmax = max(g.z)*1.05d0*100.d0
nr = fix(abs(rmax-rmin)/2 + 1)
nz = fix(abs(zmax-zmin)/2 + 1)
grid = rz_grid(rmin,rmax,nr,zmin,zmax,nz)

;Equilibrium
fields = read_geqdsk(inputs_dir+'g132224.02005', grid, rho=rho, g=g)
```

```
fields = create_struct(fields,"geqdsk",g)
fields.time *= 1.d-3 ;[s]

;Distribution function
fbm = read_nubeam(inputs_dir+'132224H02_fi_1.cdf',grid, btipsign=btipsign)

;Plasma
plasma = extract_transp_plasma(transp_file, fields.time, grid, rho)

;Inputs
inputs = create_struct("comment",'Pitch analysis for He3(d,p)He4',$
         "time",fields.time,$
         "shot",g.shot,$
         "ab",3.01602931914d0,$
         basic_inputs, basic_bgrid)
inputs = create_struct("runid","none", inputs)

;CFPD
nrays = 1
nchan = 4
nsteps = 1375
earray = 2850 + 75.*findgen(24) ;3.6 MeV alphas
pitch = 0.600
pitch_id = '600'

;Detector orientation
orientations = fltarr(3, nchan) ; [vr, vphi, vz]
orientations[*,0] = -[-2, pitch*sqrt(((-2)^2+(-1)^2)/(1-pitch^2)), -1];V1
orientations[*,1] = -[-1, pitch*sqrt(((-1)^2+(-1)^2)/(1-pitch^2)), -1];V2
orientations[*,2] = -[+0, pitch*sqrt(((+0)^2+(-1)^2)/(1-pitch^2)), -1];R1
orientations[*,3] = -[+1, pitch*sqrt(((+1)^2+(-2)^2)/(1-pitch^2)), -2];R0

inputs.runid = 'He3_NBI_a_'+pitch_id
```

```
;Creates the sightline array and defines the CFPD table
cfpd = spf_cfpd(result_dir+'/'+inputs.runid+'.idl', inputs_dir+'g132224
    ↪ .02005', earray, v=orientations, amu=4, z=2, nsteps=nsteps, nrays=
    ↪ nrays, step=.08)

;Write
prefida, inputs, grid, nbi, plasma, fields, fbm, cfpd=cfpd

end
```

Using the prefida inputs, the CFP signals in FIDASIM are calculated with the following FORTRAN code. For conciseness, structure names `cfpd%` and `inputs%` are removed in the snippet below. Refer to our GitHub [57] page for the full details of the code.

```
subroutine cfpd_f
    !+ Calculate charged fusion product count rate and weight function using a
    ↪  fast-ion distribution function F(E,p,r,z)
    real(Float64), dimension(3) :: vi, vi_norm, v3_xyz, xyz, r_gyro
    real(Float64), dimension(4) :: mamu
    real(Float64), dimension(21) :: ptcharr
    integer :: i
    type(LocalProfiles) :: plasma
    type(LocalEMFields) :: fields
    real(Float64) :: pgyro, vnet_square, factor, vabs
    real(Float64) :: eb, pitch, erel, rate, kappa, gyro, fbm_denf, tol
    integer :: ie, ip, ich, ie3, iray, ist

    !! define pitch - array
    do i=1, 21
        ptcharr(i)=real(i-0.5)*2./20.5 - 1.
    enddo
```

```
allocate(flux(nenergy, nchan))
allocate(weight(nenergy, nchan, fbm%nenergy, fbm%npitch))
flux = 0.d0
weight = 0.d0

!Masses are in [kg]
mamu(1) = beam_mass
mamu(2) = H2_amu
if (calc_cfpd.le.2) mamu(3) = H1_amu
if (calc_cfpd.eq.3) mamu(3) = He4_amu
if (calc_cfpd.eq.1) mamu(4) = H3_amu
if (calc_cfpd.eq.2) mamu(4) = He4_amu
if (calc_cfpd.eq.3) mamu(4) = H1_amu

rate = 0.d0
factor = 0.5d0*fbm%dE*fbm%dp*dl !0.5 for TRANSP-pitch (E,p) space factor
channel_loop: do ich=1, nchan
    E3_loop: do ie3=1, nenergy
        ray_loop: do iray=1, nrays
            step_loop: do ist=1, nsteps
                if (ist.gt.nactual(ie3,iray,ich)) cycle ray_loop

                !! Calculate position and velocity in beam coordinates
                call convert_sightline_to_xyz(ie3,ist,iray,ich,xyz,v3_xyz)

                !! Get fields at sightline position
                call get_fields(fields, pos=xyz)
                if(.not.fields%in_plasma) cycle step_loop

                !! Get plasma parameters at sightline position
                call get_plasma(plasma, pos=xyz)
                if(.not.plasma%in_plasma) cycle step_loop
```

```
                !! Loop over energy/pitch/gamma
                pitch_loop: do ip = 1, fbm%npitch
                    pitch = fbm%pitch(ip)
                    energy_loop: do ie =1, fbm%nenergy
                        eb = fbm%energy(ie)

                        !! Get the probability factor
                        call get_pgyro(fields,earray(ie3),eb,pitch,plasma,
↪ v3_xyz,pgyro,gyro,mass_amu=mamu)
                        if (pgyro.le.0.d0) cycle energy_loop

                        !! Calculate fast-ion velocity
                        call pitch_to_vec(pitch, gyro, fields, vi_norm)
                        vabs = sqrt(eb/(v2_to_E_per_amu*fbm%A))
                        vi = vi_norm*vabs
                        !!Correct for gyro orbit
                        call gyro_step(vi,fields,fbm%A,r_gyro)

                        fbm_denf=0
                        if (dist_type.eq.1) then
                            !get F at guiding center position
                            call get_ep_denf(eb,pitch,fbm_denf,pos=(xyz+
↪ r_gyro))
                        endif
                        if (fbm_denf.ne.fbm_denf) cycle energy_loop

                        !! Calculate effective beam energy
                        vnet_square=dot_product(vi-plasma%vrot,vi-plasma%
↪ vrot)  ![cm/s]
                        erel = v2_to_E_per_amu*fbm%A*vnet_square ![kev]

                        !! CFPD production rate and anisotropy term
```

```
                        call get_bt_rate(plasma, erel, rate, branch=1)
                        if (calc_cfpd.eq.1) call get_ddpt_anisotropy(
    ↪ plasma, vi, v3_xyz, kappa)
                        if (calc_cfpd.ge.2) call get_dhe3_anisotropy(
    ↪ plasma, vi, v3_xyz, fields, kappa)

                        weight(ie3,ich,ie,ip) = weight(ie3,ich,ie,ip) &
                                              + rate * kappa * pgyro &
                                              * daomega(ie3,iray,ich) &
                                              * factor / (fbm%dE*fbm%dp)
                        flux(ie3,ich) = flux(ie3,ich) + rate * kappa &
                                      * pgyro * daomega(ie3,iray,ich) &
                                      * fbm_denf * factor

                    enddo energy_loop
                enddo pitch_loop
            enddo step_loop
        enddo ray_loop
    enddo E3_loop
enddo channel_loop

end subroutine cfpd_f
```

Appendix D

Estimate of χ_r^2 including systematic uncertainties

To obtain a more accurate assessment of the experimental accuracy that includes the random errors associated with counting statistics and the systematic errors associated with uncertainties in the emission profile and CFP orbits, the following procedure is adopted.

1. Select one of the thermonuclear cases (enhanced or suppressed polarization; proton or alpha detection) as calculated by the baseline prediction (Figure 3.13 or Figure 3.14.) The data points for the original prediction are $\{C_i\}$.

2. Use a Gaussian random number generator with $\sqrt{C_i}$ as the one-sigma error to generate a set of synthetic data $\{D_i\}$.

3. Normalize the synthetic data, $\bar{D} = \sum_i D_i/N$, where N is the number of synthetic data points.

4. These normalized synthetic data are compared with a different set of predicted data $\{P_i\}$ that use a different emissivity profile or a different assumption about the spin

CFP	D_i	P_i:	**Baseline**	**Wide**	**Narrow**	**EFIT**
Proton	Enhanced	Enhanced	1.0	8	3	3
Proton	Enhanced	Unpolarized	13	17	9	14
Proton	Suppressed	Suppressed	1.0	1.2	3.3	1.1
Proton	Suppressed	Unpolarized	7	6	12	7
Alpha	Enhanced	Enhanced	1.0	1.0	1.3	1.7
Alpha	Enhanced	Unpolarized	11	12	8	7
Alpha	Suppressed	Suppressed	1.0	1.0	1.0	1.1
Alpha	Suppressed	Unpolarized	7	6	9	10

Table D.1: Typical values of χ_r^2 for proton detection using 15 pitch measurements or alpha detection using 3 flux measurements (first column) for synthetic data with the polarization listed in the second column. The expected values P_i are for the polarization state in the third column for the $\int S\,dl$ case listed in the fourth through seventh columns.

polarization.

5. Calculate the reduced chi-squared,

$$\chi_r^2 = \frac{1}{N-1}\sum_i (P_i/\bar{P} - D_i/\bar{D})^2/\sigma_i^2, \tag{D.1}$$

where σ_i is the random error in $D_i/\bar{D}$ associated with counting statistics.

6. Calculate χ_r^2 for multiple trials for the different $\int S\,dl$ models and assumptions about polarization. Tabulate the results.

The results of this procedure appear in Table D.1. To interpret this table, consider first the rows where the polarization of the synthetic data *is the same* as the assumed polarization of the prediction. Ideally, if the prediction was insensitive to the assumed emission profile, $\chi_r^2 \simeq 1$ for this case. However, the first row of the table shows that $\chi_r^2 \simeq 8$ if the baseline emissivity profile is replaced by the wide profile; this indicates strong sensitivity to experimental uncertainties in S. The second row shows the same synthetic data compared with the unpolarized predictions. Ideally, this would give a value of predicted χ_r^2 much larger than any of the values in the first row. However, in this case, the smallest value in the second row is only slightly larger than the largest value in the first row; this indicates that uncertainties

in S may prevent confident determination of the polarization state. Now examine the last two rows in the table. For alpha detection of suppressed polarization, the flux is insensitive to the assumed emissivity profile, so $\chi_r^2 \simeq 1$ when the suppressed case is compared with any suppressed prediction. On the other hand, when the suppressed case is compared with the unpolarized predictions, $\chi_r^2 \gtrsim 6$ for all of them. Polarization can be detected with high confidence for this case. Similarly, the middle rows of the table show that proton detection of suppressed polarization is detectable, as is alpha detection of enhanced polarization.

Appendix E

Additional AI trained to detect Alfvén eigenmodes

The crosspower spectrograms were initially used to train Linear Regression, Multi-layer Perceptron (MLP) and Convolutional Neural Networks. For regression, Tikhonov regularization is used as follows:

$$\mathbf{W}_{\text{out}} = \left(\mathbf{R}^T\mathbf{R} + \alpha\mathbf{I}\right)^{-1}\mathbf{R}^T\mathbf{D}, \tag{E.1}$$

where $\mathbf{R}$ is the data, $\mathbf{D}$ are the labels and α is the regularization parameter. For the MLP network, the models are nearly the same as the LSTM model described in subsection 4.3.2, only without the LSTM block. Lastly, the convnet contained a sequence of 5 convolutional and max pooling layers followed by a small MLP block for the final classification.

All models were capable of detecting the most common modes (TAE and RSAE) and struggled to detect the other three modes (BAE, EAE and LFM). This is likely due to the lack of memory in the models. However, the convnet was capable of performing slightly better when trained over the entire discharge (similar to the popular cat-dog classification problem)

instead of the windowing technique described in subsection 4.3.2. Although temporal information is lost when training over the entire discharge, the convnet is capable of predicting the *presence* of these modes within approximately 10% of the results reported in this paper for the recurrent neural networks.